Plasma diagnostics of discharge channels for neutralized ion-beam transport

Vom Fachbereich Physik der
Technischen Universität Darmstadt

zur Erlangung des Grades
eines Doktors der Naturwissenschaften
(Dr.rer.nat.)

genehmigte Dissertation von
Dipl.-Phys. Christoph Niemann
aus Düsseldorf

Darmstadt 2002
D17

Referent:	Professor Dr. Dr. h.c./RUS D.H.H. Hoffmann
Korreferent:	Professor Dr. W. Seelig

Tag der Einreichung:	7.2.2002
Tag der Prüfung:	6.5.2002

Zusammenfassung

In der Entwicklung zukünftiger Teilchenbeschleuniger werden extrem hohe Strahlströme für Anwendungen wie die Erzeugung von Spallationsneutronen, intensiven Neutrino - oder Kaonstrahlen, die Aufbereitung von radioaktivem Abfall oder die schwerionengetriebene Inertialfusion (IFE) eine Schlüsselrolle spielen. Die Strahlparameter sind besonders in der Trägheitsfusion sehr anspruchsvoll, wo Ionenstrahlen mit einigen zehn kA Strahlstrom und Spitzenleistungen von bis zu 10^{14} W über mehrere Meter durch eine Reaktorkammer auf ein Fusionstarget von der Größe nur weniger mm fokussiert werden müssen. Hochstrom-Plasmakanäle bieten attraktive Eigenschaften für den Transport intensiver, raumladungsdominierter Ionenstrahlen. Ein genügend dichtes Plasma kann sowohl den Strahlstrom, als auch die Raumladung des Strahls neutralisieren.

Diese Arbeit beschreibt Experimente an Entladungskanälen, die auf den Transport von intensiven Ionenstrahlen zugeschnitten sind und an der Gesellschaft für Schwerionenforschung mbH (GSI) in Darmstadt und dem Lawrence Berkeley National Laboratory (LBNL) in Berkeley durchgeführt wurden. In beiden Experimenten werden stabile Entladungskanäle durch einen Laserstrahl eingeleitet, der kurz vor der Entladung in die Kammer eingestrahlt wird. Während in Berkeley ein UV-Laser eine Spur von Elektronen hinterlässt, die durch resonante Zweiphoton-Absorption erzeugt werden, wird an der GSI ein Infrarotlaser benutzt um Ammoniak-Gas resonant aufzuheizen. Das erhitzte Gas expandiert und hinterlässt einen Kanal mit geringerer Gasdichte und somit bevorzugten Bedingungen für einen Entladungsdurchbruch. In Experimenten am UNILAC Linearbeschleuniger der GSI wurden Entladungskanäle zum ersten Mal auch durch den Ionenstrahl selbst initiiert, der das Gas in der Kammer entlang der späteren Entladungsachse ionisiert. Die Kanäle, die auf diese verschiedenen Weisen erzeugt wurden, zeigen in einem breiten Parameterbereich sehr hohe hydrodynamische Stabilität.

Um das Plasma genauer zu charakterisieren wurden verschiedene Diagnoseverfahren entwickelt und eingesetzt. Mit einem Zweifarbeninterferometer wurde die Elektrondichte im Plasma ortsaufgelöst bestimmt. Dabei ergaben sich Werte um die 10^{17} bis 10^{18} cm^{-3}. Daneben wurden mit dem selben Interferometer auch der lasererzeugte Kanal mit reduzierter Dichte sowie eine radial expandierende Druckwelle beobachtet die wahrscheinlich zur Stabilität der Entladung beiträgt. Die Druckwelle wurde detailiert mit einer Schlierendiagnostik vermessen. Das Plasmaeigenleuchten wurde im sichtbaren Wellenlängenbereich spektral aufgelöst untersucht. Es wurde ein Ratenmodell für ein Stickstoffplasma entwickelt und aus Vergleichen der experimentellen mit berechneten Spektren eine Elektronentemperatur von maximal 7 eV abgeschätzt. In Berkeley wurde im Rahmen dieser Arbeit ein Faraday-Polarimeter aufgebaut mit dem das Magnetfeld im Plasma aus der Rotation der Polarisationsrichtung eines CO_2-Lasers bestimmt wird. Erste Ergebnisse zeigen, daß der Stromfluß auf einen engen Kanal von circa 1 cm Durchmesser beschränkt ist.

Desweiteren wurden Experimente mit gekreuzten Kanälen erfolgreich durchgeführt. Dies ist für die Anwendung in einem zukünftigen Fusionsreaktor von Bedeutung, da zwei identische Ionenstrahlen von entgegengesetzter Richtung nur in einem solchen Plasmasystem auf das Target transportiert werden können. Es wurden stabile L, T und X-förmige Entladungskanäle erzeugt. Um die Tauglichkeit dieser Kanäle für den Ionenstrahltransport zu demonstrieren, wurde ein 660 MeV Ni^{+12} Strahl vom UNILAC Beschleuniger durch einen T-Kanal tranportiert und die ionenoptischen Eigenschaften untersucht.

Abstract

Most of the future accelerators will be high intensity machines delivering mega-watt beams for applications such as spallation neutron production, muon colliders, neutrino factories, nuclear-waste transmutation or inertial confinement fusion energy (IFE). Especially in the field of heavy ion driven inertial confinement fusion, where space charge dominated multi kilo-ampere beams have to be transported over several meters through a reactor chamber to a mm-size target, some kind of beam neutralization is required. Among the possible solutions is the plasma-channel based final transport. High-current discharge channels offer unique properties for ion-beam transport. They can neutralize both current and space charge of very intense ion beams and provide a strong azimuthal magnetic field all the way along the channel.

This work describes experiments performed at the Gesellschaft für Schwerionenforschung (GSI) in Darmstadt and the Lawrence Berkeley National Laboratory (LBNL) to create and diagnose high current discharge channels designed for the transport of intense ion beams. In both experiments, stable channels are created by a laser pulse which is fired into the chamber along the desired path of breakdown before the discharge is triggered. While in Berkeley a UV-laser creates an initial seed of electrons by two-photon ionization of a small admixture of Benzene molecules to the background gas, at GSI an IR-laser is used to heat ammonia gas by resonant absorption and to produce a gas-rarefaction channel with preferred conditions for a breakdown. An alternate technique, using an ion beam to initiate stable, free-standing channels has been tested successfully for the first time at the UNILAC- linear accelerator at GSI. All channels, created by either of these three methods show no signs of hydrodynamic instabilities in a wide parameter range.

Several plasma diagnostics were developed and used to gain a deeper understanding of the dynamics and stability of the discharges. In order to measure the electron density with spatial resolution a two-color imaging interferometer was developed. Peak densities around 10^{17} to 10^{18} cm^{-3} were inferred, depending on the discharge conditions. The interferometer also showed the existence of a rarefaction channel and a radially expanding gas wall which is believed to enhance the stability of the discharge. This pressure wave was studied in detail by means of schlieren diagnostics. In Berkeley a Faraday polarimeter was developed to determine the current density distribution and thus the magnetic field inside the plasma, from the rotation of the plane of polarization of a CO_2 laser beam passing through the plasma. The plasma-self emission was investigated by spectroscopy in the visible wavelength range. Measurements of the Stark broadening of hydrogen Balmer lines were used for an alternate electron-density measurement. To fit theoretical spectra to the measurements, a rate model for a nitrogen plasma was developed and a maximum electron temperature of 7 eV was derived.

For an application of plasma channels to the final focus and transport inside an inertial-confinement fusion reactor with two-sided target illumination it is required to produce intersecting discharges to provide a focusing magnetic field for two ion beams propagating from opposite sides towards the target. Experiments at GSI demonstrated that X-shaped, T-shaped and L-shaped discharges can be produced by CO_2 laser initiation. The ion optical properties of such T-discharges were investigated with a 660 MeV Ni^{+12} heavy-ion beam from the UNILAC-linear accelerator at GSI.

Contents

Chapter 1

Introduction

Recently a trend of particle-accelerator development points towards high-current machines, delivering multi-megawatt beams for applications that require high beam intensities, such as neutron-spallation sources [Gar95, Wei00], radioactive-waste transmutation [Tuy93], energy amplifiers [Car93], neutrino or kaon factories [Gee98], muon-colliders [Ank99] or drivers for heavy-ion inertial fusion energy [Ban99]. While accelerators which are being built today, like the spallation neutron source in the USA [Wei00] are already expected to reach average beam powers in the megawatt range, the most demanding requirements have to be met in heavy-ion beam driven inertial fusion energy (IFE).

Thermonuclear fusion is potentially a clean, safe energy source with an unlimited fuel supply. In the 'inertial confinement' approach to obtain controlled thermonuclear fusion in the laboratory, a small target of frozen deuterium and tritium is illuminated by intense ion beams from several sides. Due to the large beam energy deposition, the target is heated and the ablating material compresses the fuel to 1000-times the solid state density. When the fusion capsule reaches temperatures around 10 keV the hydrogen isotopes fuse to helium and release a large amount of energy, which can then be converted into electric power. During the entire burn process, which requires only a few picoseconds, the fuel is confined only by the inertia of the mass. To reach the conditions for thermonuclear burn a beam energy of some MJ must be delivered to the fusion target within roughly 10 ns. This corresponds to a peak-beam power of the order of 100 TW and electric ion-beam currents around 20 kA [Hog92].

The final beam - focus and transport over several meters inside the chamber of an inertial-confinement fusion reactor has been identified as one of the most critical design issues, since the extremely intense and space-charge dominated beams tend to diverge and 'blow up' rapidly and the beam spot requirements on the target are hard to meet. As a consequence the total beam current must then be distributed over as many as hundred separated beams in the reactor chamber, in order to reduce the individual current in each beam.

High-current discharge channels provide attractive properties to focus and transport intense ion beams over distances of several meters. Due to the high conductivity a typical discharge plasma can neutralize both beam current and space charge of fusion relevant ion beams. Once the beam is captured at the channel entry the transport to the fusion target is relatively insensitive to details of beam current, pulse shape, emittance or chromaticity. The discharge current also provides a strong focusing magnetic field all the way to the target. In a plasma channel based fusion reactor, the total required beam current can be transported to the target in only two beams from opposite sides, compared to tens of beams in a reactor with conventional ballistic transport. Consequently a transport channel relaxes the requirements for the accelerator and reactor system considerably [Yu98, Tau96, Tau98].

Discharge channels can also be an interesting alternative for beam transport in other applications, where intense or poor quality particle beams have to be transported over long distances. One possible future application may be the collection and transport of intense ion beams, which

have recently been created with powerful short pulse lasers [Sna00]. Those beams of high intensity and extremely small emittance open up a whole new field of applications but cannot be transported with conventional magnets due to their large momentum spread. Neutralizing discharge channels with their large acceptance and achromaticity may also be used in the future to collect, focus and transport intense ion beams for the production of secondary particles, such as spallation neutrons, muons or neutrinos.

This work describes experiments on discharge plasmas, designed for the transport of intense ion beams, which were carried out at the Gesellschaft für Schwerionenforschung (GSI) in Darmstadt and the Lawrence Berkeley National Laboratory (LBNL) in Berkeley. Discharges, suited for ion-beam transport have to be stable up to and during the passage of the ion beam. Breakdown must take place exactly along the beam axis rather than towards the metallic wall of a reactor chamber. Guiding structures like insulator tubes or metallic wires cannot be used, since they are destroyed as the fusion target ignites. During the beam transport the discharge must have a certain current and diameter to provide the required magnetic field, and therefore the current rise time has to be matched to the channel dynamics.

Different techniques for the initiation of stable, self-standing discharge channels, which fulfill those conditions were tested in the framework of this thesis. The discharges are initiated and guided by a laser pulse, fired into the gas along the preferred path of breakdown before the discharge is triggered. At GSI a CO_2-laser is used to resonantly heat low pressure ammonia gas to temperatures up to 1000 K. When the heated gas expands, a rarefaction channel is formed along the laser path, which favors conditions for a breakdown and also stabilizes the discharge. In the Berkeley experiment, a UV-laser creates a trace of seed electrons by resonant two-photon absorption in a low pressure nitrogen-benzene gas mixture. The preferred technique to produce stable channels with this method is a sequence of four distinct steps, including the formation of a gas-rarefaction channel by Joule heating and an electric low energy prepulse discharge before the actual high current discharge. A novel approach to initiate free-standing discharges has been tested for the first time at GSI, using the ion beam from the UNILAC linear accelerator itself to create an initial seed of electrons as the beam ionizes the background gas. This technique has the advantage, that the channels can be produced in any gas, in particular heavy rare gases like xenon, which due to its high mass is presently considered to be the most suited candidate for a fusion reactor.

The main part of this thesis describes different diagnostic techniques, which were developed and used to measure important plasma parameters, both in Berkeley and at GSI. These measurements are of foremost importance for a thorough understanding of the discharge dynamics and stability. Of particular interest are the electron density, the temperature and the current density distribution or the magnetic field, which determines the ion optical properties of discharge channels. Detailed experimental measurements at different discharge parameters are crucial to benchmark simulation codes, which can then be used to predict the performance of other channels not presently accessible by experiments and to design the most suited discharge for a certain application. First comparisons with a one-dimensional fluid code were done in the framework of this thesis for some of the measurements.

Chapter 2 summarizes the physics of gas discharges, relevant for this work. The ion-optical properties of such plasma channels for single-particle transport and the neutralized transport of space charge dominated beams are discussed. A one-dimensional Lagrangian fluid code (CYCLOPS) which was developed in Berkeley, to model several aspects of the pinch experiments, is briefly introduced.

The different channel initiation mechanisms including laser-gas heating, UV-laser induced ionization and beam initiation is presented in chapter 3. Channel stability and evolution as measured by simple diagnostics such as fast shutter and streak imaging are discussed.

An overview of the different diagnostic techniques, which were developed and used at GSI and Berkeley to provide a better understanding of the processes and parameters of the plasmas

is given in chapter 4. Electron densities were measured with spatial resolution by a two-color imaging interferometer. The same method also showed the formation of a neutral-gas density depression after the laser-gas heating and a radially expanding pressure wave. Detailed measurements of this expanding gas wall, which contributes to the stability of the discharge, were performed both with a schlieren and a shadowgraphy technique. The plasma-self emission in the visible range was investigated by means of time resolved spectroscopy. Line integrated electron densities were derived from the Stark-broadening of hydrogen Balmer lines and compared to results from the interferometry. A rate model for a nitrogen plasma, including electron-impact ionization, three-body-, radiative- and dielectronic recombination, collisional excitation and spontaneous emission was developed to calculate the population densities of the relevant energy levels and to reproduce the measured spectra. In this way the electron temperature can be derived from a measurement of relative intensities of nitrogen lines. In Berkeley a Faraday polarimeter was developed to measure the current distribution inside the plasma. The magnetic field is reconstructed from the rotation of the plane of polarization of a CO_2 laser at 10.6 μm, measured by a scheme of different polarizers and fast infrared detectors (HgCdTe), working in the half-shadow principle. Performance tests of the system and preliminary measurements are presented.

An application of the plasma channel concept inside the chamber of an inertial confinement fusion reactor with a two-sided target requires the formation of intersecting channels [Yu98, Tau96] (see chapter 2.6). Experiments at GSI demonstrated that it is feasible to bend discharges by a laser beam around a 90 degree corner and to produce intersecting channels suited for ion beam transport (chapter 5). Different discharges with the shape of an L, T or X were created. In experiments a Ni^{+12} beam with an energy of 660 MeV was transported through a 30 cm long T-shaped discharge channel over a quarter of a betatron oscillation and the ion-optical properties were investigated.

Chapter 2

Fundamentals of discharge channels for ion beam transport

2.1 Basic gas-discharge physics

2.1.1 Gas breakdown

A gas breakdown occurs, when a discharge between two electrodes starts to produce enough charge carriers by ionization to maintain itself. In steady state, the discharge has to create as many electrons from the cathode as are lost at the anode, to maintain the current flow. In the *Townsend-theory* the gas breakdown is explained by the interplay of two processes: the impact ionization of atoms by electrons as they propagate towards the anode and the release of new electrons from the cathode. The number of electrons created in the gas per length and electron is described by the first Townsend coefficient α. The third Townsend-coefficient γ denotes the number of electrons released from the cathode per electron created in the gas by ionization. The most important processes which are responsible for the release of electrons from the cathode are emission by ion-collisions and photo emission. In a self-maintained discharge an electron on its way to the anode has to create at least one new electron through collisions of created ions at the cathode. Therefore following condition has to be fulfilled:

$$\gamma e^{\alpha d} \geq 1 \ , \tag{2.1}$$

where d is the length of the discharge tube. The *Paschen-law* which describes the relation between breakdown voltage V_{br} and the product of pressure p and distance between the electrodes d, can be derived analytically from the Townsend-theory. With the Ansatz $\alpha = c_1 \cdot p \cdot exp(-c_2 \cdot p/E)$ for the first Townsend-coefficient and $V_{br} = E/d$, relation 2.1 leads to

$$V_{br} = \frac{c_2 \cdot \ p \cdot d}{ln(c_1 \cdot p \cdot d) - ln[ln(\gamma)]} \ . \tag{2.2}$$

The Paschen curve for ammonia gas [Rad68] which is used for most of the experiments in this work is shown in figure 2.1. The minimum breakdown voltage occurs at a pd product of around 0.6 $torr \cdot cm$. At higher pressures the breakdown voltage increases nearly linearly with the gas pressure. This behaviour is due to the E/p-dependence of α. At higher pressures, the smaller mean free-path length of the electrons must be compensated by a higher electric field. For a small pd - product, where the mean free-path length is large compared to the length of the discharge tube, almost no ionizing collisions take place. At the minimum of the Paschen-curve the mean free-path length is comparable to d. The vertical lines in figure 2.1 mark the pd - product for the GSI-transport channel experiment (chapter 3.1) at pressures of 5 and 20 mbar, corresponding to breakdown voltages of 8 kV and 30 kV respectively. The Townsend-theory is only valid for discharges, where space-charge effects can be neglected and in the approximation of infinite large, plane electrodes.

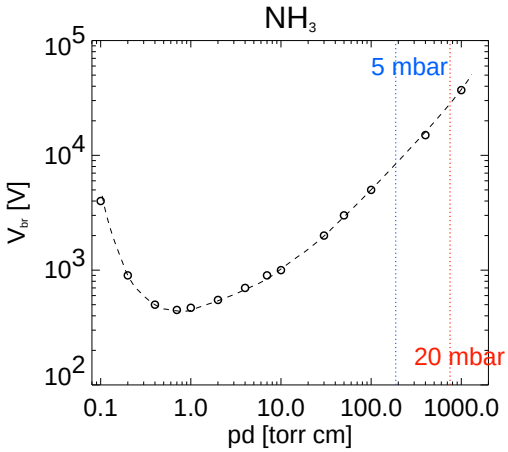

Figure 2.1: Paschen curve of ammonia [Rad68]. The vertical lines indicate the *pd* product for 5 and 20 mbar.

2.1.2 Pulsed discharges

The Paschen-law describes the breakdown behaviour in discharges with a constant electric field between the electrodes. The plasma channels investigated in this work are formed in pulsed discharges. An energy of more than one kilojoule is stored in a capacitor bank of several μF, charged up to 30 kV. The discharge is triggered by a fast high-voltage spark gap switch. Current and voltage oscillate sinusoidally as the energy shifts from the capacitors into magnetic energy and back. The electric circuit can be approximated by the external bank capacity C_{ext}, the inductance of the cables L_{ext} as well as the inductance and resistance of the plasma L_{pl} and R_{pl}. The discharge voltage U_C and current I are related by

$$\dot{I} = \frac{U_C - I(R_{pl} + \dot{L}_{pl})}{L_{ext} + L_{pl}} , \qquad \dot{U}_C = -\frac{I}{C_{ext}}. \tag{2.3}$$

Such an LC-circuit can be described by $I(t) = \hat{I}_0 e^{-\delta t} sin(\omega t)$ where $\delta = R/2L$ is a damping factor, $\omega = (1/LC)^{1/2}$ the *Thomson-frequency* and L the total circuit inductance. The discharges investigated in this work have current rise times of a few μs and a resistance of around 100 Ω, causing only a weak damping.

Compared to static discharges, pulsed discharges show a complex channel dynamics. At early times the gas kinetic pressure can be too small, to balance the magnetic pressure caused by the azimuthal magnetic field. As a consequence, the discharge "pinches"by its own magnetic field to a minimum diameter until the increasing kinetic pressure stops the contraction and finally leads to an expansion of the discharge. The investigation of the dynamics of discharges suited for the transport of ion beams is one objective of this work. The time-interval until the current maximum is of foremost interest, because the high magnetic field provides the best conditions for ion beam transport. After the pinch time high-current discharges usually become unstable. In addition to experiments, numerical simulations of the pinch dynamics are crucial. Several models were developed to simulate z-pinch plasmas [Ros54, Pot78, Miy84]. A one-dimensional hydrodynamic code which was designed for the transport-channel experiment at Berkeley will be introduced briefly in chapter 2.5.

2.1.3 Skin effect

In AC-discharges with an alternating current, inductive effects can lead to an increased current flow at the surface of the plasma. This behaviour is called the *skin effect*. In the case of

a sinusoidal current evolution and a cylindrical plasma with constant conductivity, the current density distribution can be calculated analytically from Maxwell's equations and Ohm's law. The equations can be solved by a Bessel function of 0^{th} order [Lan74]. For very small frequencies the current density distribution j becomes homogeneous. For higher frequencies, where the current-carrying region is small compared to the plasma diameter, the current density drops exponentially from the edge towards the center. The skin depth $d = (2/\omega\mu\sigma)^{1/2}$ expresses the distance from the surface where j has dropped by 1/e. Here ω is the current frequency, μ the magnetic permeability and σ the conductivity of the plasma. For the case of discharges with a constant diameter and conductivity it was shown [Hai59], that as a transient phenomenon current-density distributions with a positive current flow on the discharge axis and a reversed current at the edge can exist in pulsed discharges. This behaviour is called the *inverse skin effect* [Bog91]. The discharges described here have a skin depth comparable to the channel diameter so that an almost homogeneous current-density distribution is expected at most times.

2.2 Laser initiation of plasma channels

High-current discharges for beam focusing are usually initiated in insulating discharge tubes which guide and stabilize the discharge [Ste96]. If guiding structures like insulator tubes or metal wires can not be used as in the case of an inertial confinement fusion reactor (see chapter 2.6), the discharge can be initiated by a laser beam. Several methods using different laser-gas combinations have been tested. Preionization of organic molecules by ultraviolet lasers using a resonant two-photon absorption process provides an effective way to guide a discharge [Lee82, Tay80]. Absorption of a KrF laser (248 nm) or frequency quadrupled Nd:YAG laser beam (266 nm) for example in gases such as Tripropylamine (TPA) or Benzene (C_6H_6) is a suitable technique for generating large, well-defined ionized volumes [Woo85, Mar85]. Electron densities above $10^{12} cm^{-3}$ are easily obtained with a few mJ of laser energy [Fro82]. The Berkeley-channel experiment which is described in chapter 3.2 is also initiated in this way. Another effective method of coupling laser energy into a gas is 'laser ionization based on resonance saturation' (LIBORS) [Mea79]. A dye laser tuned to the resonance line of an alkali vapor (e.g. 670.8 nm for Lithium) creates a dense population of atoms in the excited resonance state, which provides translation energy to produce free electrons by collisions and a large number of atoms with an ionization energy reduced by the laser photon energy. In experiments [Mci77] a dye laser pulse of 1 MW with a duration of 800 ns produced a 15 cm channel with an electron density higher than $10^{15} cm^{-3}$ in a vapor pressure of 0.1 torr. These techniques, which form and control a plasma channel almost entirely by ionization, are in contrast to the technique used for the GSI-channel (chapter 3.1). Here a CO_2 laser is resonantly absorbed in low pressure ammonia (NH_3), causing gas heating which produces a rarefaction zone with only a slight amount of ionization. Experiments with this initiation mechanism were first investigated for light-ion beam transport experiments [Ols81a, Ols81b, Ols82].

2.3 Ion-optical properties of discharge channels

Cylinder-symmetric discharge channels are an ideal focusing device for charged particle beams, since the azimuthal magnetic field causes at each point a force on the moving particle, which is directed towards the symmetry-axis of the discharge. Therefore z-discharges are superior to conventional quadrupole magnets, which provide only a focusing field in one plane and a defocusing field in the perpendicular plane [Bog92]. The ion-optical properties of a z-discharge are determined by the radial dependence of the azimuthal magnetic field $\vec{B}(\vec{r})$, which is related

to the current density distribution j by Biot Savart's law [Jac83]

$$\vec{B}(\vec{r}) = \frac{\mu_0}{4\pi} \int \frac{\vec{j}(\vec{r'}) \times (\vec{r} - \vec{r'})}{|\vec{r} - \vec{r'}|^3} dV \ , \tag{2.4}$$

where $\mu_0 = 4\pi \cdot 10^{-7} Vs/Am$ is the magnetic permeability. In an axial-symmetric discharge like a z-pinch it follows easily from Ampere's law

$$\oint_C \vec{B} d\vec{s} = \mu_o \cdot I \tag{2.5}$$

that

$$B(r) = \frac{\mu_0 \cdot I(r)}{2\pi r} \tag{2.6}$$

where $I(r)$ is the total current flowing through the area enclosed by the circle of radius r

$$I(r) = \int j(\vec{r'}) d\vec{A} = 2\pi \int_0^r j(r') r' dr'. \tag{2.7}$$

For the special case of a homogeneous current-density distribution an analytic expression can be derived for the magnetic field inside the plasma

$$B(r) = \frac{\mu_0 I}{2\pi R^2} \cdot r \qquad (\text{if } r \leq R) \ , \tag{2.8}$$

where R is the discharge radius and I the total discharge current. Here the azimuthal magnetic field increases linearly with the radius. Outside of the current-carrying area the field shows the typical 1/r fall-off:

$$B(r) = \frac{\mu_0 I}{2\pi r} \qquad (\text{if } r > R). \tag{2.9}$$

The propagation of an ion beam in a z-discharge channel is illustrated in figure 2.2. The Lorentz force acts always perpendicular on the direction of propagation. The field strength decreases towards the discharge axis. In a cartesian coordinate system with the ion beam propagating in the z-direction the components of the magnetic field become

$$B_x = -\frac{y}{r} B(r) \qquad B_y = \frac{x}{r} B(r) \qquad B_z = 0 \ , \tag{2.10}$$

where $r = \sqrt{x^2 + y^2}$. For low beam currents as available at GSI or for neutralized beam transport (chapter 2.4), a single particle motion for each ion under the influence of the Lorentz force can be assumed. For ions of mass A and charge state C the differential equation to be solved is

$$\ddot{\vec{x}} = \frac{e \cdot C}{m} \vec{v} \times \vec{B} = \frac{e \cdot C}{m_p \cdot Z + m_n \cdot (A - Z)} \begin{pmatrix} -v_z B_y \\ v_z B_x \\ v_x B_y - v_y B_x \end{pmatrix}, \tag{2.11}$$

where Z gives the number of protons in the ion. The charge state C of the ions is determined by stripping in the gas of the differential pumping system before entering the discharge channel. The equilibrium charge state in gas can be calculated by the empirical Betz-formula [Bet83]

$$C = Z_{ion} \left[1 - exp \left[-0.555 \cdot \left(\frac{\beta \cdot 137}{Z_{ion}^{0.517}} \right)^{1.175} \right] \right] \ , \tag{2.12}$$

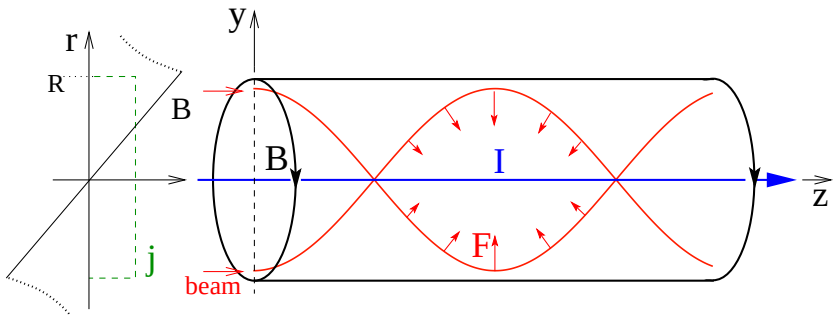

Figure 2.2: Propagation of an ion beam in a z-discharge plasma in the case of a homogeneous current density distribution.

where Z_{ion} is the atomic number and $\beta = v/c$ the velocity of the projectile. The Lorentz factor γ and the velocity factor β are connected to the beam energy per nucleon E_{kin}

$$\gamma = \frac{E_{kin} + m_n c^2}{m_n c^2} \ , \qquad \beta = \sqrt{1 - \frac{1}{\gamma^2}} \ , \tag{2.13}$$

where $m_n \approx 938\ MeV/c^2$ is the average mass of a nucleon in the projectile.

The ion-optical properties of discharge channels at GSI were calculated by numerically solving equation 2.11 for a number of randomly distributed ions representing an ion-bunch from the UNILAC-linear accelerator, including beam emittance, energy spread and a Gaussian beam profile. The results are compared with ion beam transport measurements in chapter 5.

2.4 Transport of space-charge dominated ion beams

In very intense ion beams, self forces between individual particles become important. The moving space charge of the ion beam causes electric and magnetic self-fields which exert forces on an ion moving with the beam. A beam with the typical parameters for a heavy-ion fusion reactor (chapter 2.6) would cause a radial electric field in the order of $10^7\ V/m$ without space-charge neutralization [Tau01b]. A fundamental limit of the beam current is reached at the so-called *Alfvén current* I_A

$$I_A = \frac{4\pi\epsilon_0 m_p c^3}{e} \frac{\beta\gamma A}{q} \ , \tag{2.14}$$

when the azimuthal magnetic field becomes so strong, that the cyclotron radius is equal to half of the beam radius. The ions would then be overfocused and lost. Here A is the mass number and q the charge state of the ions. Also the space-charge potential limits the maximum beam current, when it becomes comparable to the kinetic energy of the ions. The ions are stopped when all their kinetic energy is converted into potential energy. The current limit due to the space-charge potential is for beams relevant for a heavy-ion fusion reactor smaller than the Alfvén-current limit. For a Bi^{1+} beam of 10 GeV for example the Alfvén-current limit is around 2 GA, while the space charge limit for 1 cm beam radius and 10 cm beam-pipe radius is only 7 MA [Tau01b].

The typical timescale for beam current neutralization can be derived from Maxwell's equation and Ohm's law, neglecting the displacement current [Jac83]. An initial configuration of magnetic field will decay away in a diffusion time

$$\tau_m = \mu_0 R^2 \sigma \ , \tag{2.15}$$

where R is a length characteristic of the spatial variation of $\vec{B}$ and σ the conductivity. In a discharge plasma with a typical conductivity around $10^5\ Sm^{-1}$, τ_m is much larger than the

beam-pulse duration τ, while the charge-neutralization time

$$\tau_c = \frac{\epsilon_0}{\sigma} \tag{2.16}$$

is much shorter than τ. In typical discharge plasmas, ion beams are completely space charge and current neutralized after a very short time (picoseconds) and for a duration of several hundreds of nanoseconds. When an ion beam with a current of several hundreds of kA enters a discharge plasma with currents in the order of 50 kA, the space charge will be neutralized within a very short time. Although the beam current is much higher than the discharge current, the magnetic field of the discharge remains "frozen" for a time in the order of τ_m, which is long enough for the passage of the beam bunch. This property makes discharge plasmas ideally suited for the final beam transport through the reactor chamber in inertial fusion energy (chapter 2.6). The physics of space-charge dominated ion beams is described in detail in [Tau01b].

2.5 The one-dimensional fluid-code CYCLOPS

CYCLOPS is a one-dimensional Lagrangian fluid-code designed at Berkeley to model several aspects of the pinch-dynamics for the transport-channel experiment [Hen98, Van00, Pon01, Pon02]. It is based on the force equation

$$\rho(r,t)\frac{dv_r(r,t)}{dt} = j(r,t)B(r,t) - \frac{\partial p(r,t)}{\partial r} \tag{2.17}$$

for the cylinder symmetric plasma. The electron density is calculated from the continuity equation including electron impact ionization and recombination, which are estimated from empirical formulas. The magnetic field and thus the current density are calculated from a magnetic diffusion equation

$$\frac{dB}{dt} = \frac{1}{\mu}\frac{\partial}{\partial r}\frac{1}{r\sigma}\frac{\partial(rB)}{\partial r} - B\frac{\partial v_r}{\partial r} \ , \tag{2.18}$$

which follows from Maxwell's equations and Ohm's law, ignoring the displacement current. A gas energy balance equation includes Joule heating, convection, creation of electrons through avalanching, heat radiation and thermal conduction. The boundary conditions couple the external circuit equations (compare equation 2.3) to the channel dynamics. Several assumptions are made to simplify the model [Hen98]. The gas is assumed to be sufficiently dense to justify a single-fluid model and to obey the ideal-gas equation of state. First results and comparisons with measurements are reported in [Pon01]. For the GSI-channel experiment, which works with ammonia gas, CYCLOPS was so far only used to simulate the gas dynamics after the laser-gas heating (chapter 3.1). The code will be described in more detail in [Nef02].

2.6 Plasma-channel based final focus and chamber transport for heavy-ion inertial confinement fusion

2.6.1 Heavy-ion inertial confinement fusion

Fusion is potentially a safe, clean energy source with an unlimited fuel supply. In the inertial-fusion energy (IFE) approach, energy will be produced by thermonuclear fusion of hydrogen isotopes in a small fusion target which is compressed and heated by intense laser or particle beams. If the mm-size target is illuminated symmetrically with a power around 10^{14} W, the ablating matter compresses the target to a density of 1000 times the solid-state density and strongly heats the fuel. At temperatures around 10 keV in the target center, the conditions for fusion are met. The α-particles created in the fusion reactions, heat the remaining matter until the entire target is burned. During the burn process, which takes only a few ps, the fuel is

confined only by the inertia of the mass [Hog92]. To keep the micro explosions at a controllable size, but to deliver the typical power-plant net power around 1 GW, milligram-targets will have to be ignited with a repetition rate of several Hz. Ion accelerators are in many ways, ideally suited to the requirements of fusion power production [Ban99]. They can be durable, reliable, efficient, and can easily achieve the required pulse repetition rates. However, to deliver the required power, beam energies of several megajoule are needed, corresponding to peak beam currents of several tens of kA.

2.6.2 Final focus and transport inside the reactor chamber

The beam with an energy of some megajoule has to be delivered onto a fusion target of only a few mm size. The reactor chamber will have a diameter of several meters to protect the wall from target debris and to reduce the neutron impact per area. The extremely intense ion beams must therefore be transported over a distance of several meters without any guiding structures inside the chamber, which would be destroyed during every micro explosion. Different transport modes are extensively studied. Ballistic transport, based on conventional quadrupole magnets outside of the chamber and no additional focusing forces inside, is a convenient approach. However, when stripping effects in the rest gas of the chamber increase the beam current to the mega-ampere level, the space charge can easily lead to an uncontrolled blow-up of the beam and the required focal spot size can not be met. Several neutralization modes were proposed to compensate the space-charge effects, including the transport through a cloud of electrons, which has to be made available to the beam. The electrons can also be provided by a plasma or a background gas which is ionized by the ion beam itself. In the case of incomplete current neutralization, the beam pinches under the influence of its magnetic self-field. This *self-pinched* propagation of an intense proton beam, which was recently reported for the first time [Ott00], is one of the most promising candidates for an application in a reactor.

An alternate approach to the chamber transport in a heavy ion beam fusion reactor is the plasma-channel based transport. This scenario was considered before for light ion fusion [Fre82]. The channel transport relaxes the requirements on the accelerator system considerably. A first point design of a final transport /reactor system has been constructed [Yu98] considering a modified HYLIFE II reactor [Moi92] filled with a background gas of a few mbar and a two-sided target illumination. Ignition is for example predicted for a 6.5 MJ drive with 4 GeV Pb ions delivered in 8 ns onto the target with 5 mm radius spots [Tab98]. The scheme is shown in figure 2.3. On either side of the reactor, the beams from several accelerators are focused by final conventional quadrupole magnets and then combined in an adiabatic plasma lens [Tau96]. This lens is a current-carrying discharge with a tapered discharge tube, which reduces the beam diameter from initially around 1 cm to a size commensurate with target requirements. The focused but strongly divergent beam is then transported in a laser initiated 50 kA discharge channel from the chamber wall to the target. Once the beam is captured at channel entry, transport to the target is very insensitive to beam parameters and the beam diameter at the target will be the same as at the channel entrance. Adiabatic lens and transport channel can be driven by the same pulse generator. To transport two beams from opposite sides, the current is returned by two additional plasma channels which are initiated by another laser beam perpendicular to the ion beam direction. The targets are injected into the chamber with a velocity that is small compared to the discharge time scales. At the time of channel initiation the target will therefore be already in position. Experiments on intersecting discharge channels and channel-target interaction have been performed at GSI and will be presented in chapter 5. The ions entering the gas-filled chamber become highly stripped. Although the tens of kA of particle current correspond to multimega-amperes of electrical current, the highly conductive plasma provides total neutralization of the beam-space charge and current (chapter 2.4). Channel-based final transport offers the additional advantage of small beam entrance ports

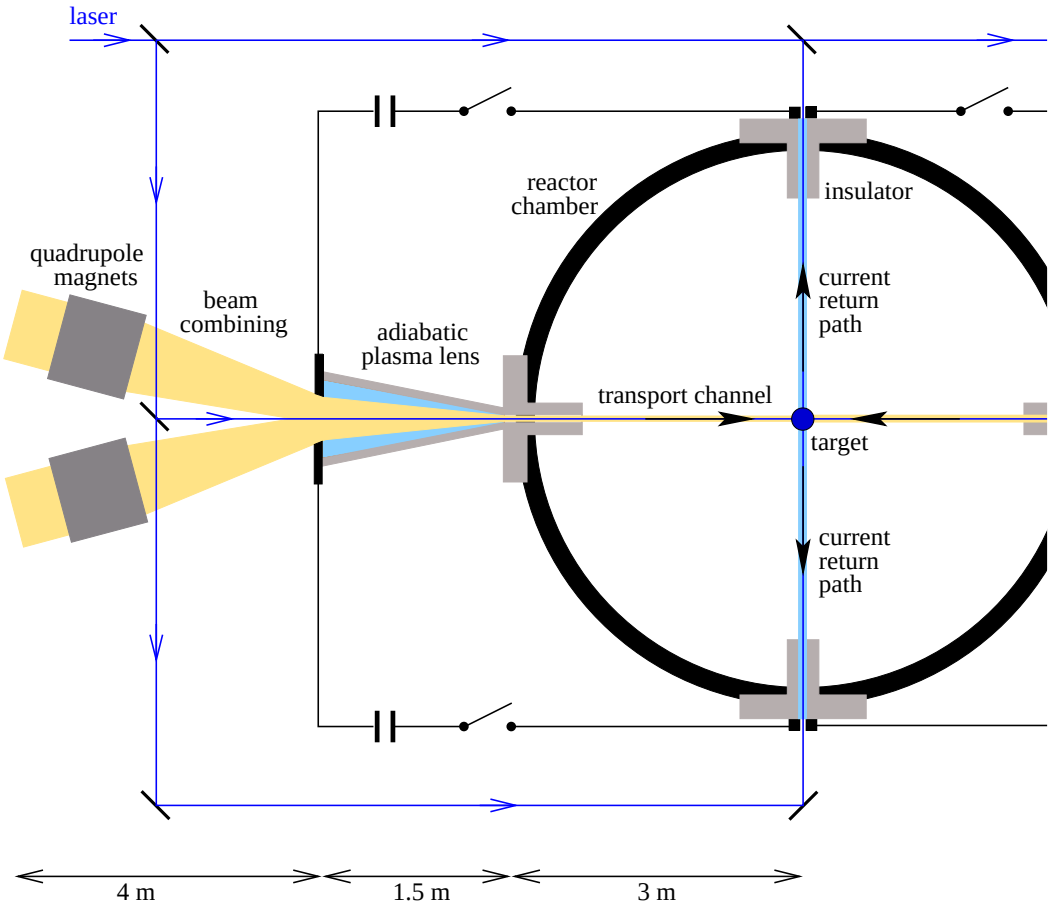

Figure 2.3: Schematic of a plasma-channel based fusion reactor.

which reduce the neutron bombardment of devices outside the reactor chamber like quadrupole magnets. The channel-transport scenario is compatible to fusion chambers with a neutronically thick liquid layer [Moi92]. The fluid layers are envisioned to consist of molten salts or metals such as lithium and serve as a protection of the first structural wall from neutrons, photons, charged particles and target debris [Ban99]. They would also be used to breed the tritium required for the operation of the power plant. Motivated by the advantages of the plasma-channel transport, discharge channels designed for this purpose are under investigation both at Berkeley and at GSI for a couple of years. Apart from low energy proton beams from pulsed-power diodes [Ner93, Blu92], no intense ion beams are currently available to study the neutralized beam transport in plasma channels. However, the discharge channels for chamber-transport can be investigated without the beam and the transport capability can be verified once the appropriate beams become available. This is an advantage compared to other focusing concepts like the self-pinched transport, which requires intense ion beams already for the experiments. For the transport-channel concept, the effect of the strong gas heating as the stripped beam deposits its energy along its path has to be studied in more detail. Until the relevant beams will be available, such studies have to be performed by simulation codes.

Chapter 3

Discharge-channel initiation mechanisms

3.1 Initiation of plasma channels by laser-gas heating

At GSI stable, free-standing high-current plasma channels are initiated by a CO_2 laser, which heats ammonia gas by resonant absorption before the discharge is triggered. The heated gas expands and leaves a gas-density depression behind, which represents a preferred path of breakdown for the discharge. This method was first used successfully in Sandia [Ols80, Ols81a, Ols81b] to create free-standing discharge channels for light-ion beam transport. This chapter describes the GSI channel experiment. The channel stability and evolution, measured by simple diagnostics, such as fast shutter or streak imaging, is discussed. More advanced measurements will be presented in chapter 4.

3.1.1 The GSI-transport channel experiment

The GSI laser-channel experiment consists of a cylindrical, stainless-steel discharge chamber of 50 cm length and 60 cm diameter with two high-voltage electrodes on opposite sides, insulated from the chamber by plexiglass flanges (figure 3.1). The chamber is filled with ammonia (NH_3) at pressures between 2 and 25 mbar in a steady gas flow. Before the discharge is triggered, a CO_2 laser pulse is fired into the chamber through a ZnSe entrance window and a 15 mm diameter bore hole in the anode. The laser beam leaves the chamber through a second ZnSe window in the cathode, where the energy is measured by a pyroelectric detector. With the laser wavelength tuned to a molecular vibration frequency of the NH_3 molecule, laser energy is efficiently coupled into the gas. This heating causes an expansion of the gas, creating a rarefaction channel along the desired path of breakdown on the chamber axis. Some microseconds after the laser pulse, a capacitor bank of 2.6 to 7.8 μF charged to 20 kV is connected to the electrodes by a spark gap switch and a discharge channel is formed along the laser path. To prevent breakdown from the electrodes directly to the wall a plexiglass tube extends 10 cm into the chamber from each side. An electric low-energy prepulse discharge can be applied from a separate pulse generator with a 200 nF capacitor in between the laser pulse and the main discharge, to stabilize or shape the channel. While the prepulse is optional, the laser pulse is crucial for a successful channel creation. Without the laser pulse the discharge will always break down to the wall. The discharge chamber was integrated into the Z4 beamline of the UNILAC linear accelerator, with the beam axis aligned to the chamber symmetry axis for the beam-transport experiments described in chapter 5. A differential pumping system, consisting of several roots and turbo pumps was used to reduce the pressure from the mbar range inside the chamber to the 10^{-6} $mbar$ range in the accelerator beamline. Both pulse generators as well as the discharge chamber are enclosed in Faraday cages with only small entrance ports for the laser and diagnostics. The chamber is

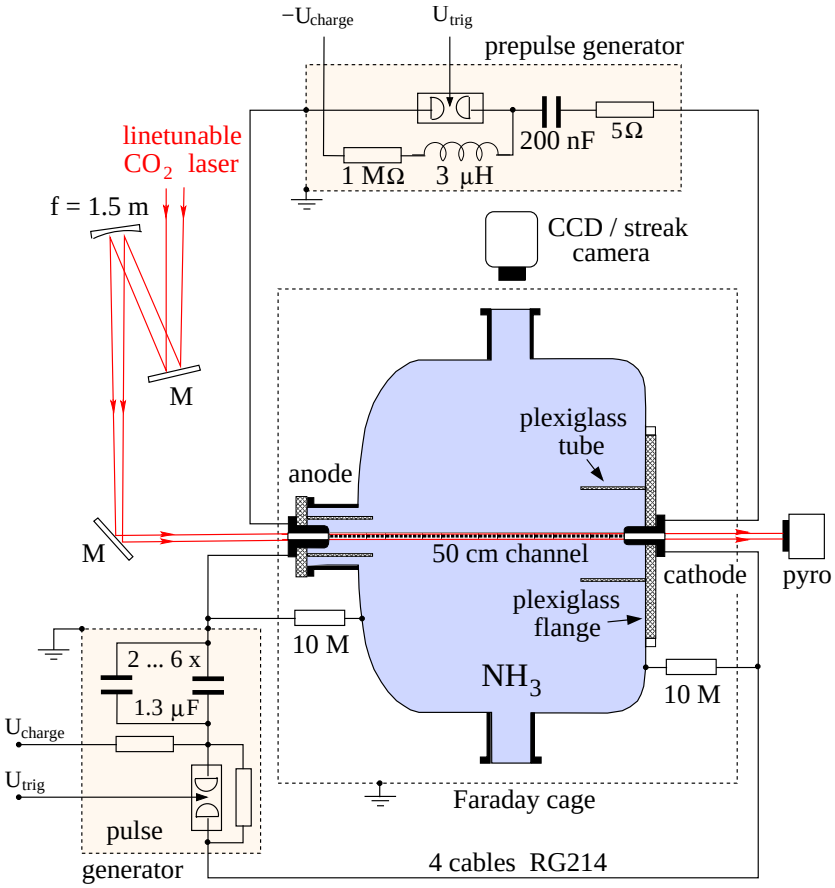

Figure 3.1: Setup of the GSI laser-channel experiment.

kept on mid-potential between the electrodes by two 10 $M\Omega$ resistors. Both anode and cathode are stainless steel cylinders with diameters of 5 cm and 3 cm respectively. Four cables (RG 214) connect the main capacitor bank to the electrodes to keep the inductance low. The total circuit inductance and the resistance for a 2.6 μF capacitor, measured with a 60 cm long 1 cm diameter brass rod replacing the plasma channel are 815 ± 1 nH and 54 ± 2 $m\Omega$ respectively. The current rise time for a discharge with a capacitor of 7.8 μF charged to 20 kV is around 4 μs depending on the gas pressure. A calibrated shunt measuring the total current driven by the pulse generator is used to determine the discharge current.

3.1.2 Laser-gas interaction

The TEA CO_2 laser (SLCR, manufacturer Model ML204) is line-tuneable by a diffraction grating and delivers microsecond pulses with an energy around 5 J. A f = 1.5 m concave mirror focuses the laser in the middle of the discharge chamber. The footprint of the rectangular beam profile varies only slightly from 0.9 cm^2 in the focus to 1.1 cm^2 near the electrodes. The maximum energy density in the chamber is around 2 J/cm^2. The 1.5 m focal length is a compromise between uniformity along the channel and energy density. The wavelength is adjusted to the P(32) transition for peak absorption, matching the $\nu_2 = 950$ cm^{-1} vibrational mode in NH_3 [Ols81a]. In this way a large fraction of the laser energy is absorbed as the beam passes through the 50 cm long gas filled chamber, down to pressures of a few mbar (figure 3.2 a). Compared to an untuned CO_2 laser oscillating at 10.6 μm the line tuning improves the absorption by more than one order of magnitude. The absorption A was measured with a pyroelectric detector behind the chamber. Since only one detector was available, several shots were averaged to compensate laser energy fluctuations, and compared with the energy measured behind the evacuated

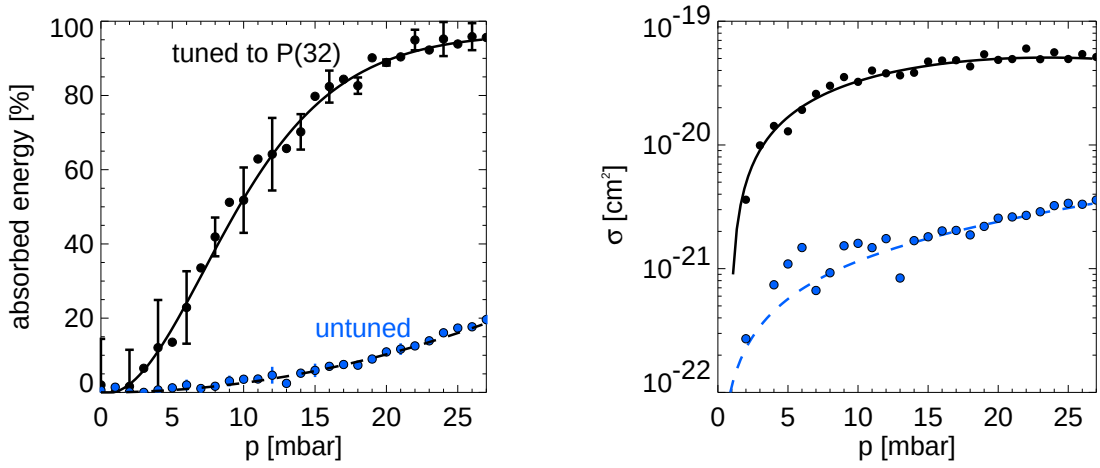

(a) Absorbed laser energy

(b) Absorption cross section

Figure 3.2: Absorbed laser energy (a) and absorption cross section (b) as a function of pressure for an untuned laser oscillating at 10.6 μm as well as the laser tuned for peak absorption, both at 1.8 J/cm^2 incident laser energy. The error bars represent the standard deviation of three different laser shots. The absorption data was fitted by polynomials of higher order. The curves for the cross sections were calculated from those fits by equation 3.1.

chamber. The bandwidth for resonance detuning is around 10 nm (FWHM) as determined from the decrease of absorption in 20 mbar from 90 percent down to almost zero. Changing the wavelength by a few nm around the resonance can adjust any absorption in between the extremes. An absorption close to 100 percent is not favourable because of the strong temperature variation along the channel. A stronger heating and rarefaction near the anode compared to the cathode then leads to asymmetric initial conditions for the discharge. Especially at high pressures the wavelength should therefore be slightly detuned from the peak absorption. The absorption cross section (figure 3.2 b) is calculated from the measured transmissivity $T = 1 - A$ by

$$\sigma = 1/(N \cdot L) ln(1/T) \ , \qquad (3.1)$$

where N is the molecular density and L the length of the interaction volume. The absorption of the laser energy I along the gas cell is given by $\partial I/\partial z \sim -\sigma \cdot I$ assuming $\frac{1}{c}\partial I/\partial t \ll \partial I/\partial z$ which is the case for the short laser pulse length. This leads to an exponential decrease of energy deposition along the channel, causing an exponential temperature decay along the channel. However, the absorption also depends on the incident laser energy. Saturation effects in NH_3 lead to a decreased absorption cross section for higher energy densities. The saturation was measured in 4.5 and 10 mbar ammonia for an energy density ranging from 0.6 to 1.8 J/cm^2 (figure 3.3). The cross section varies by more than a

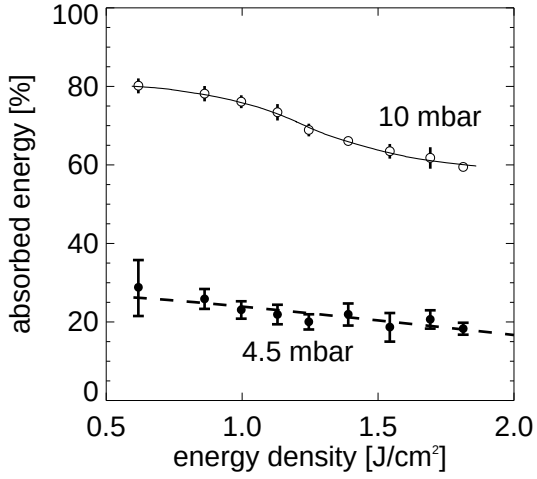

Figure 3.3: Absorption as a function of incident laser energy density.

factor of two for the 10 mbar gas fill. The temperature near the entrance is therefore somewhat decreased compared to the exponential case. A maximum temperature of the laser heated gas between 1000 and 2000 K can be estimated from the absorbed energy and the heat capacity of ammonia. The better absorption at higher pressures is compensated by the increasing mass of the gas. Therefore the highest temperatures are obtained at around 15 mbar. The saturation, the temperature dependence of the heat capacity of ammonia as well as the onset of dissociation at a temperature around 2000 K make a precise calculation of the laser gas heating rather complex. An interaction model was developed in [Ols81a] to calculate the temperature of the laser heated gas in longer gas cells, including saturation effects. For an energy density of 2.5 J/cm^2 temperatures changing almost linearly from 1500 K at the entrance down to 700 K near the exit of the chamber were calculated for a 25 mbar gas fill [Ols81a]. The same paper reports in detail on cross sections of other ammonia lines as well as resonance lines of different organic gases which are appropriate candidates for CO_2 laser heating. Ammonia was chosen for the GSI experiment, because of its small heat capacity, fast vibrational-translational relaxation time and because of the fact that NH_3 leaves no carbon deposits in the chamber after the discharge.

3.1.3 Channel initiation

The expansion of the heated gas and the creation of a rarefaction channel on the predefined discharge axis lead to a decrease in breakdown voltage and thus guide the discharge along the laser path, while the surrounding gas wall contributes to the stability of the discharge channel. The reduction of breakdown voltage due to the laser pulse is illustrated in figure 3.4.

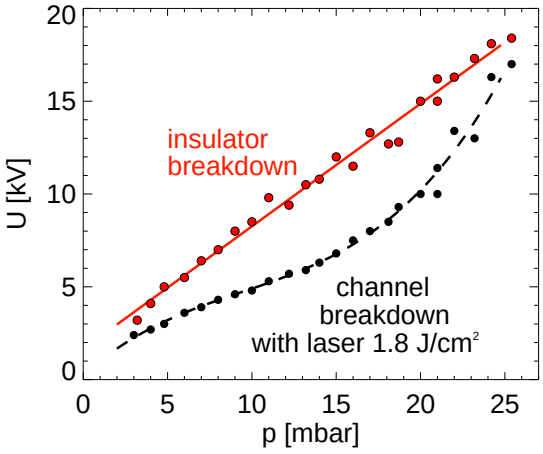

Figure 3.4: Breakdown voltage as a function of pressure. With the laser pulse breakdown occurs along the channel, without the laser around the insulators and along the chamber wall.

For the measurement the prepulse capacitor was charged step by step to higher voltages until a breakdown occurred within 10 μs after the laser pulse was fired. Without the laser pulse the breakdown occurs around the insulators and the current flows on the chamber wall (insulator breakdown). The laser shows the biggest effect for a pressure of 15 mbar, reducing the channel breakdown voltage by 40 percent of the value for an insulator breakdown. At low pressures the absorption is too small to show a big effect while at higher pressures the entire laser energy is absorbed in the first few centimeters of the chamber so that no gas is heated near the cathode. The insulator breakdown does not occur between the two electrodes directly but from the electrodes to the wall, which is possible at a lower threshold voltage. Therefore the laser reduces the gas breakdown voltage by more than 40 percent. A direct measurement in this experiment is not possible due to the metallic chamber. Olsen [Ols81b] measured a reduction in breakdown voltage of 60 percent for an energy deposition of 2 J/cm^2 in an insulating ammonia gas cell at 25 mbar. For 30 J/cm^2 the breakdown voltage was reduced by more than 90 percent.

With a *pd* product in the GSI experiment of around $5 \cdot 10^2$ $mbar \cdot cm$ the discharge behaviour is characterized by the linear right-hand branch of the room temperature Paschen curve (chapter 2.1.1 figure 2.1). A reduction of breakdown voltage of 40 percent should be caused by a similar reduction of gas density. Assuming the ammonia Paschen curve for a dc-discharge a measured channel breakdown voltage of 7 kV at 15 mbar corresponds to a density reduction of 70 percent

due to the laser.

The breakdown voltage shows an almost linear decrease with incident laser energy density (figure 3.5). A lower laser energy limit for a successful channel creation is reached when the channel breakdown voltage with laser pulse becomes comparable to the voltage for insulator breakdown, in the case of a 15 mbar gas fill at an energy density of around 0.5 J/cm^2. If the discharge voltage is higher than the voltage for insulator breakdown, the laser pulse will successfully produce channels and a breakdown along the wall is avoided. No upper voltage limit could be measured in the accessible parameter range up to 20 kV. At voltages a few kV above the breakdown limit it is possible to create channels with discharge-trigger delays up to milliseconds, which shows that the gas density in the rarefaction channel remains low for this timespan.

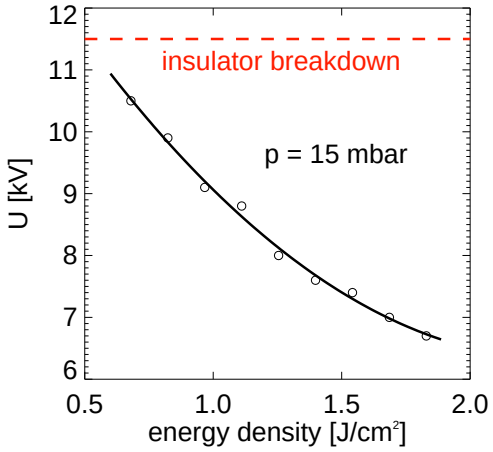

Figure 3.5: Breakdown voltage for 15 mbar as a function of deposited laser energy.

The hydrodynamics of the laser heated gas was simulated by the one-dimensional Lagrangian fluid code CYCLOPS (chapter 2.5). Figure 3.6 shows the evolution of the gas density during the first 20 μs after the laser pulse. A Gaussian temperature profile reflecting the laser energy distribution with a maximum temperature of 800 K, a FWHM of 7 mm and a flat gas-density distribution at 15 mbar were assumed as initial conditions. After a few microseconds a gas-density bubble is formed while a pressure wave is expanding radially with a velocity of around 0.5 $mm/\mu s$ (figure 3.6). At 15 μs the density on

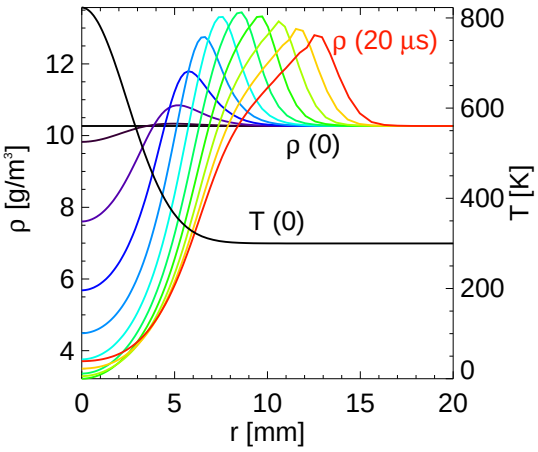

Figure 3.6: Hydrodynamics of the laser heated gas as calculated by CYCLOPS. The graph shows the temporal evolution of the gas density profile during the first 20 μs in 2 μs steps as well as the initial temperature profile after the laser heating with a maximum temperature of 800 K at an initial pressure of 15 mbar.

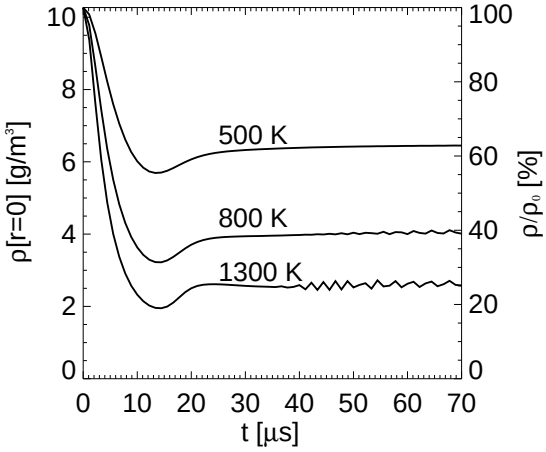

Figure 3.7: Evolution of the gas density on axis for three different initial gas temperatures, an initial gas pressure of 15 mbar and a FWHM of the temperature profile of 7 mm.

axis has dropped by more than 60 percent. CYCLOPS runs show that the size of the density

bubble does not depend on the maximum initial temperature but only on the shape of the laser footprint. The temporal evolution of the gas density on axis for different initial temperatures of the laser heated gas at a pressure of 15 mbar is shown in figure 3.7 . For 500 K the gas density drops by 40 percent within the first 15 μs, for 1800 K by 80 percent. A minimum gas density is reached at 15 μs. After this time the density increases by a few percent until it reaches a steady state at around 25 μs with only a small increase for the next hundreds of microseconds. The same behaviour can be observed for different initial gas pressures. The time where the minimum gas density is reached depends only on the width of the initial temperature profile but not on the gas pressure or the maximum temperature. For Gaussian profiles the width and the time of the minimum density scale roughly linearly for widths of a few mm to cm. In a simulation with an initial temperature profile of 10 mm FWHM the minimum gas density is reached at 20 μs. The evolution of the rarefaction channel manifests itself indirectly in the discharge delay

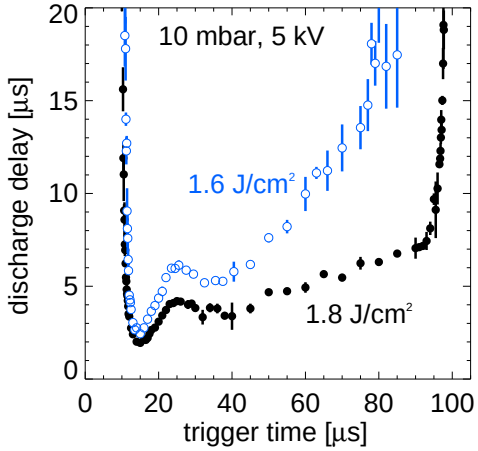

Figure 3.8: Discharge delay at different discharge trigger times with respect to the laser heating.

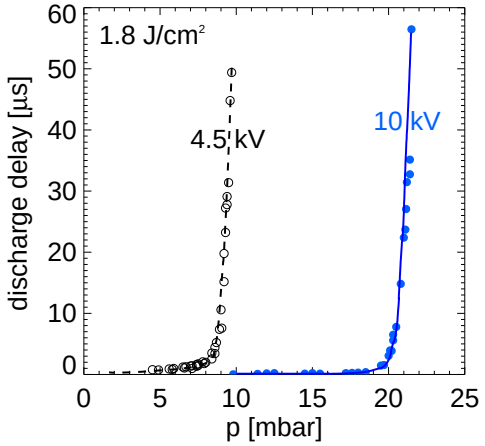

Figure 3.9: Discharge delay as a function of pressure for 4.5 kV and 10 kV. The graph shows the sudden increase of the delay as the pressure exceeds a critical value.

(figure 3.8). At voltages a few kilovolt above the breakdown limit the discharge ignites instantaneously without any internal delay. For a voltage close to the breakdown limit (dashed curve in figure 3.4) the discharge ignites after a certain delay depending on voltage, pressure and the laser-pulse characteristics. The jitter of this delay is of the order of tens of nanoseconds for delays up to a few microseconds. When the filling pressure is increased above a critical value, the delay increases fast in the tens of microseconds range (figure 3.9). In this regime, the jitter in the order of tens of microseconds does not allow reproducible discharge conditions. For even higher pressures no channel can be created. Already during this delay a very weak channel self emission can be recorded with an image intensified camera. While at this time the gas pressure is still too high for an electron avalanche a small current is driven through the rarified gas, causing additional joule heating and gas rarefaction. When the density drops below a critical value a cascade breakdown occurs and the discharge channel is formed. The same behaviour was observed at the Berkeley experiments [Vel98] during the so called "laser induced resistor phase" in between laser pulse and prepulse-discharge. The minimum discharge delay is obtained for a trigger delay of 15 μs with respect to the laser pulse. This minimum and the subsequent increase of the delay by a few percent shows the same behaviour as the gas density calculated by CYCLOPS, indicating that the discharge delay is determined primarily by the evolution of the gas density. At the parameters from figure 3.8 the discharge can only be created when the trigger delay is between 10 and 90 μs. The steep increase of the delay occurs at times where

the simulated gas density on the channel axis (figure 3.7) has approximately the same value. The sudden decrease and increase of the discharge delay at these times can be explained by the sensitive dependence of the delay on the pressure (figure 3.9). The gas density at these times is just at the critical value for a channel breakdown.

3.1.4 Channel stability and evolution

A series of photographs of a 44 kA main discharge in 10 mbar NH_3 recorded side-on with a gated, image intensified camera with an exposure time of 100 ns is shown in figure 3.10. The discharge was triggered 15 μs after the laser pulse. The pictures show reproducibly straight,

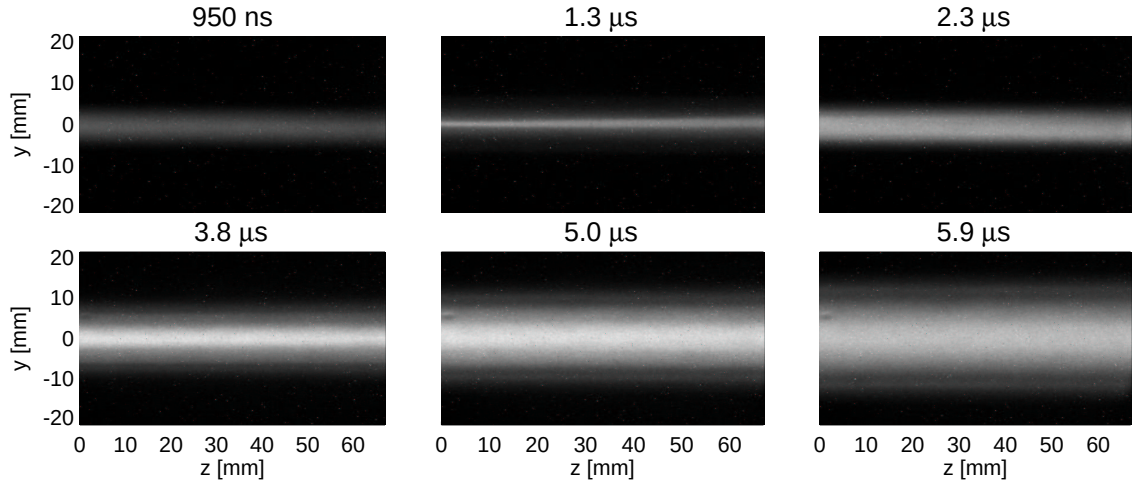

Figure 3.10: A series of fast-shutter photographs of a 44 kA discharge in 10 mbar taken at different times.

stable channels for at least 15 μs, also after the peak current is reached at 4 μs. Due to the size of the vacuum windows, only the central section of the channels with a length of 70 mm is visible. Straight channels can be produced up to pressures of 20 mbar for times before the current maximum. However above 15 mbar the channels show instabilities mainly of the kink type at times later than 3 to 4 μs. A lower pressure limit is set by the decreasing absorption and the onset of insulator breakdown. Straight, stable channels were created at pressures as low as 2 mbar. Prepulse discharges with 1 kA and main discharges with reduced bank capacity at 20 kA and a current-rise time of 2.5 μs are stable throughout the entire investigated pressure range from 2 to 25 mbar. Stable discharges were also produced with a preceding prepulse channel triggered 10 μs before the main bank and 15 μs after the laser pulse, up to pressures of 20 mbar. A delay exceeding 20 μs between prepulse and main discharge creates stable channels only during the first 3 to 4 μs.

The kink instability, which was observed in previous Sandia National Laboratory experiments [Ols82] in channels above 30 kA during the current rise, is not seen in the GSI experiment at most discharge conditions. In the worst case instabilities became visible after 3 to 4 microseconds. MHD modes typically require timescales of the order of an Alfvén transit time to grow [Man84]. The growth rate Γ of the kink instability (m=1) for a discharge in vacuum is $\Gamma_{kink} = k \cdot v_A$, where k is the wave number of the instability and v_A the Alfvén speed. A similar growth rate can be assumed for the sausage instability (m=0). The Alfvén speed is calculated from

$$v_A = B_\Theta (\mu_0 n m_i)^{-1/2} \tag{3.2}$$

where n is the density of ions with mass m_i in the channel. For a 40 kA discharge in nitrogen with an ion density of $5 \cdot 10^{16}$ cm^{-3} and a channel diameter of 1 cm, the Alfvén speed

is in the order of 10^4 m/s. An instability with a wavelength of $\lambda = 1$ cm and a wavenumber of $k = 100$ m^{-1} the growth rate becomes roughly $\Gamma = v_A \cdot k = 10^6$ s^{-1}. An initial disturbance of I_0 grows to an amplitude of $I_0 \cdot exp(\Gamma t)$ in a time t. For the example given above, an initial disturbance of $I_0 = 0.1$ mm grows to 0.1 $mm \cdot exp(4) \approx 5$ mm in 4 μs.

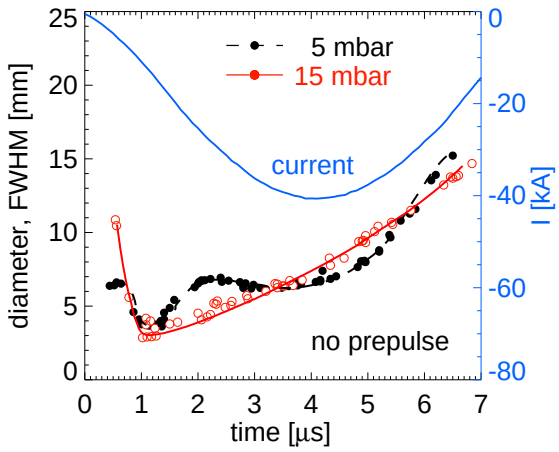

Figure 3.11: Channel evolution and discharge current for a discharge at 5 mbar and 15 mbar without prepulse discharge.

According to [Man73] the enclosing gas wall reduces the MHD instability growth rate of the discharge by a factor of $(\rho_g/\rho_{ch})^{1/2}$, where ρ_g and ρ_{ch} are the mass densities of the pinch and the surrounding gas respectively. This factor is around 1.5 to 2 for the rarefaction channel formed by the laser pulse.However, when the gas is heated by the discharge after breakdown a second shock is launched radially, increasing the mass density of the surrounding gas [Pon01]. A pressure wall with the 10-fold density in addition to the rarified gas in the channel would reduce the kink growth rate by a factor of 5 to 6. This would allow only one growth time during a first half period of the discharge and could be an important contribution to the stability of the channels. The channel evolution for different discharge conditions measured by streak and fast shutter imaging is shown in figures 3.11 and 3.12. Channel diameters were determined as the FWHM of a Gauss fit to the profiles obtained from the fast shutter images. Discharges at 15 mbar (figure 3.12) show a pinching from a diameter bigger than 10 mm down to 3 mm at around 1.2 μs. Discharges at 5 mbar show a second less pronounced pinch at the time of the current

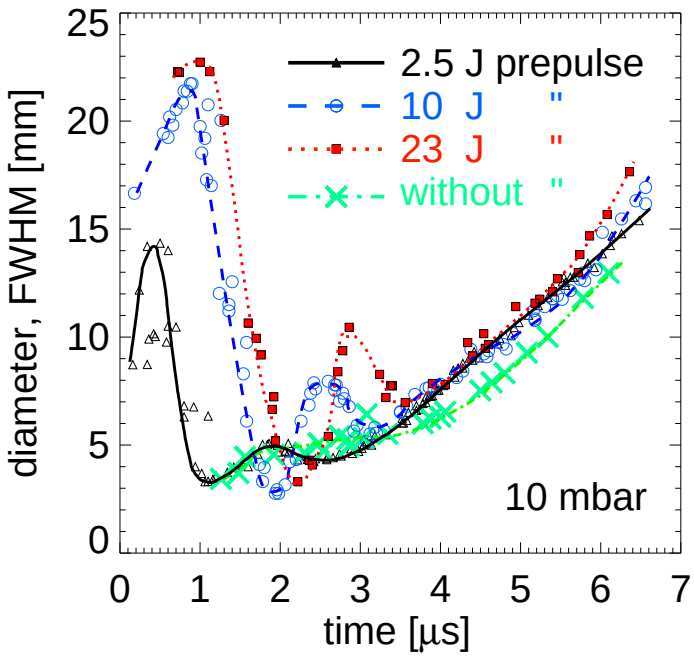

Figure 3.12: Channel evolution for a 40 kA discharge at 10 mbar with 2.5 J, 10 J, 23 J prepulse and without any prepulse.

minimum around 4 μs. Different laser energy deposition or discharge trigger delays do not show any difference in the channel diameter within the range of accuracy. Triggering the prepulse discharge prior to the high current discharge has a bigger effect on the channel evolution. Figure 3.12 shows the channel diameter evolution for a 10 mbar discharge without prepulse as well as with prepulse at different voltages. The initial conditions of the main discharge are altered considerably by the prepulse. The channel starts at larger initial diameters compared to discharges without prepulse, indicating a lower initial pressure on axis caused by the prepulse. Subsequently the discharge pinches down to around 3 mm at a time of 1.1 μs, 2.0 μs and 2.3 μs for a prepulse energy of 2.5 J, 10 J and 23 J respectively. In all three cases a second less pronounced pinch occurs at 2.6 μs, 3.3 μs and 3.5 μs like in the 5 mbar discharge without prepulse. After the current maximum the channel expands with a radial velocity of around 1 $mm/\mu s$ independent of the predischarge.

3.2 Initiation of discharge channels by UV-laser induced ionization

A similar experiment as decribed in the previous chapter is in operation at LBNL-Berkeley, running at comparable parameters. Discharges with a length of 40 cm and currents exceeding 50 kA are produced in a gas of 5 to 10 torr, typically nitrogen. Stable channels are initiated by a sequence of four distinct steps: (1) preionization of the gas by a UV laser along the desired path of breakdown, (2) Joule heating and rarefaction of the gas along this path, (3) low energy prepulse discharge and (4) high current main discharge. A resonant two-photon absorption of the UV laser in a small admixture of benzene creates the required seed electrons. Simulations by CYCLOPS predict the formation of an on-axis low density channel by hydrodynamic expansion after the prepulse discharge. This rarefaction channel in turn will prepare the right conditions for the high current discharge to be stable and very reproducible and plays therefore the role that the CO_2 laser has in the experiment at GSI.

Good qualitative understanding of the pinch dynamics and stability of the channel by means of plasma diagnostics and simulations is the objective of the LBNL channel experiment. The experiment is described in more detail in [Tau01] and the doctoral thesis of D. Ponce [Pon02].

3.2.1 Experimental setup

Figure 3.13 shows the experimental setup. The rectangular metal chamber has inner dimensions of 406 mm x 305 mm x 280 mm. Two 15 cm diameter brass electrodes with 13 mm diameter holes for the laser are mounted on plexiglass insulators at the chamber. Insulator rings extend 10 cm into the chamber to prevent a direct breakdown toward the chamber wall. A frequency quadrupled Nd:YAG laser initiates the discharge in a nitrogen-benzene gas mixture by weakly ionizing the benzene. Nitrogen serves as a background gas, providing most of the ions in the high current discharge. The ratio between benzene and the background gas was typically less than 10 %. Up to thirty-two 50 kV, 0.15 μF capacitors in the main capacitor bank (total maximum capacity 4.8 μF) are charged up to 30 kV and switched by a high voltage spark gap. A prepulse capacitor (150 nF to 500 nF) charged between 3 kV and 10 kV is connected to the electrodes by a laser-triggered spark gap. This gap consists of a pair of brass balls in air with an adjustable spacing and was triggered by the not converted first harmonic Nd:YAG beam.

3.2.2 Resonant two-photon absorption

The UV laser creates a seed of electrons along the laser path by the absorption of two photons in the benzene. Organic molecules like benzene, with many internal degrees of freedom have an ionization potential which allows two-photon but not single-photon ionization in an intense

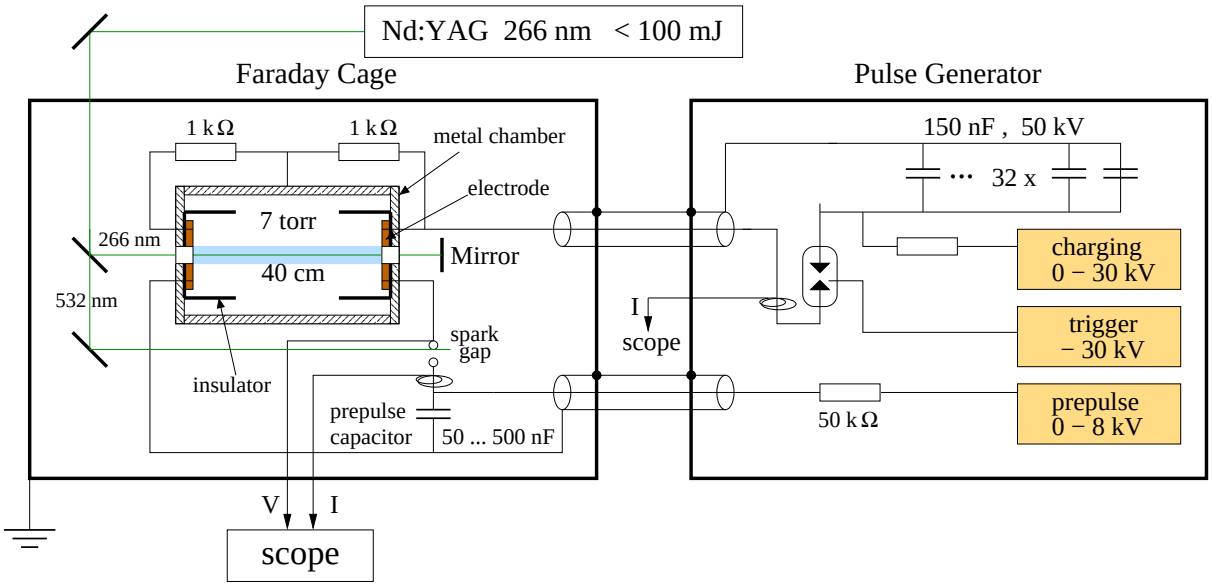

Figure 3.13: Setup of the Berkeley transport channel experiment.

UV-laser field. The number of electrons produced by a laser pulse of intensity I (W/cm^2), pulse length Δt (s) and photon energy $h\nu$ (J) is given by [Woo85]

$$n_e = \frac{n_0 \alpha I^2 \Delta t}{h\nu} \ , \tag{3.3}$$

where n_0 is the neutral molecule density and α the two-photon ionization coefficient. The two-photon absorption process can in most cases be considered as a single-photon excitation, followed by a one-photon ionization of the excited state. The ionization coefficient α therefore contains the cross section σ_1 for photoexcitation of the intermediate state and its photoionization cross section σ_2. The first discharge channels at Berkeley were initiated by a KrF laser at 248 nm in benzene [Tau96]. The two-photon ionization coefficient was measured for benzene at this wavelength [Woo85] to be $\alpha = 8.0 \cdot 10^{-27}\ cm^4/W$. The photoionization threshold of benzene is 9.25 eV while the photon energy at 248 nm is only 5 eV. Only two photons provide therefore the energy, required for ionization. Electron densities above $10^{12} cm^{-3}$ have been measured in a few torr of benzene, when irradiated with laser energies of a few tens of mJ [Fro82]. The typical laser output for the initiation of discharge channels at Berkeley was 150 mJ in a 20 ns pulse, with less than half of the energy coupled to the benzene. A typical gas mixture was 0.5 torr benzene and 6 torr nitrogen. Laser energy measurements behind the gas filled chamber show an exponential laser absorption with roughly 80 percent absorbed at 2 torr of benzene [Vel98].

Channels were also initiated by a frequency quadrupled Nd:YAG laser at 266 nm with an energy of 100 mJ and a pulse width of 10 ns. The photon energy at this wavelength is 4.7 eV making a two-photon absorption process in principle possible. However, to successfully initiate channels the benzene pressure had to be as high as 1 torr, indicating a smaller α.

3.2.3 Channel initiation

The preferred technique for the formation of stable, reproducible channels was a sequence of four steps [Vel98]. First a seed of electrons is created by two-photon absorption of the frequency quadrupled Nd:YAG laser ($\lambda = 266$ nm). The unused frequency doubled component of the laser ($\lambda = 532$ nm) triggers the laser-spark gap for the prepulse capacitor, which is charged to a few kV. Although the prepulse voltage is immediately applied to the channel electrodes, the gas pressure prevents an instantaneous breakdown. However, the seed electrons are accelerated under the

applied electric field, causing Joule heating and subsequent expansion of the gas along the laser path. This phase which lasts for some microseconds up to tens of microseconds, depending on the voltage, initial pressure and laser pulse characteristics was called the laser induced resistor (LIR) [Vel98]. Once the density drops below a critical value the electron avalanche occurs and a low energy prepulse discharge is formed. The prepulse creates a long-lived gas-density depression with a density reduction of 90 percent, estimated by CYCLOPS-simulations [Pon01]. This rarefaction channel serves as a preferred electric breakdown path for the following high current discharge, which is triggered 30 to 40 μs after the prepulse breakdown occurs. The channel-initiation sequence is illustrated in figure 3.14. Once the prepulse discharge has been

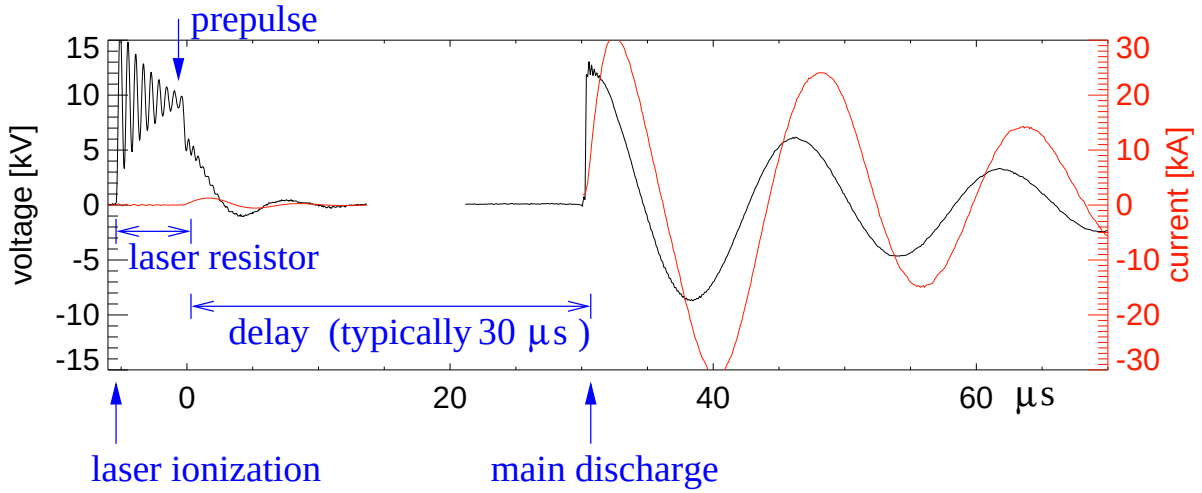

Figure 3.14: The channel-initiation sequence used at the Berkeley experiment: (1) laser ionization, (2) laser induced resistor phase, (3) low energy prepulse and (4) high current discharge. The sudden drop of the prepulse voltage at $t \approx 0$ μs indicates the occurrence of the avalanche.

initiated successfully, the high current main discharge has been found to be always stable and reproducible [Pon01]. The benzene consumption by the high-current discharge is significant and leaves a carbon residue inside the vacuum chamber, which requires frequent cleaning.

3.3 Ion beam initiated channels

3.3.1 Motivation

For an application in heavy-ion beam fusion, discharges will have to be produced in gases different from ammonia or benzene, that are not compatible with a reactor environment. Seed electrons can then be created with femtosecond-lasers in any gas [Yu98]. In experiments at GSI, stable discharges were also initiated by the ion beam from the UNILAC linear accelerator. Seed electrons that guide the discharge are created as the ion beam ionizes the background gas along the channel axis. A 2 mm diameter, circular beamlet of Ni^{+12} ions was used to produce free-standing discharges in ammonia and argon without a laser. Beam currents as low as 5 μA at 11.4 AMeV energy were sufficient to reproducibly initiate stable discharges of 50 cm length at currents in excess of 55 kA. In following beamtimes, stable channels were also created in N_2, air, He, Kr and Xe [Nef02, Pen02]. The possibility to initiate discharge channels with the ion beam increases the attractiveness of the channel-transport scenario because of the flexibility in choosing the filling gas and the simple discharge-initiation mechanism.

3.3.2 Discharges in ammonia and argon

Ion beam initiated discharges in ammonia and argon were created by a Ni^{+12} UNILAC-beam . The setup was the same as in figure 3.1. A beam mask with a single 2 mm diameter hole aligned exactly to the channel axis was used to prepare a narrow beamlet which defines the size of the ionization channel. The total beam current was around 50 μA measured in the last Faraday cup before the beam mask. The beam intensity behind the 2 mm diameter hole can be estimated to be roughly 5 μA, assuming a Gaussian beam profile with $\sigma = 5\ mm$. The discharge is triggered 20 μs after the beginning of a 50 μs long macro pulse.

An upper limit for the electron density in the gas along the ion beam can be estimated from the energy conservation, assuming that the total beam-energy loss in the gas is used to ionize always the electron with the lowest ionization potential in the gas atoms, and that no recombination occurs. The energy loss of the Ni^{+12} beam can be obtained from semiempirical stopping-range data tables [Zie96] as $E = 507\ eV/(10^{15} atoms/cm^2)$. At a gas pressure of 10 mbar this corresponds to an energy loss of $E \cdot \rho$, roughly 150 keV/cm for each ion. An electric current of $I = 5\ \mu A$ with a charge state of $q = 12+$ carries per time $\Delta t = 20\ \mu s$ a number of ions of $N = I \cdot \Delta t/(q \cdot e) = 5.2 \cdot 10^7$. Therefore the total beam energy loss per volume for a beam with cross section $A = \pi \cdot 1\ mm^2$ is $\Delta E = N/A \cdot 150\ keV/cm = 2.5 \cdot 10^{14}\ eV/cm^3$. Consequently, with an ionization potential of $\chi = 12\ eV$ for the first electron, the maximum number of electrons that can be produced by the beam is $\Delta E/\chi \approx 2 \cdot 10^{13}\ cm^{-3}$. The exact electron density must be calculated from the cross sections in a ballancing model, including also recombination. This value might be one or two orders of magnitude below the upper limit, estimated above. However, even then the electron density is comparable or higher than the electron densities obtained by the UV-laser induced ionization (chapter 3.2), which shows, that an ion beam as available at GSI is at least as suited to initiate discharge channels as a strong UV-laser.

The low energy prepulse was applied optionally before the main discharge. If the prepulse discharge was created successfully, the following high current discharge was always stable and reproducible. All discharges were stable even at very late times with and without the prepulse in ammonia and argon gas, with the capacitor bank charged to 25 kV, yielding a maximum discharge current of 55 kA. Channels in NH_3 could only be produced at pressures around or below 5 mbar. At higher pressures the discharge broke always down around the insulator tubes towards the metallic chamber. Figure 3.15 shows a series of fast shutter photographs of an ion beam initiated 55 kA discharge in 5 mbar NH_3 with an additional 10 kV prepulse, fired 10 μs before the main discharge. The exposure time was 30 ns. Even after

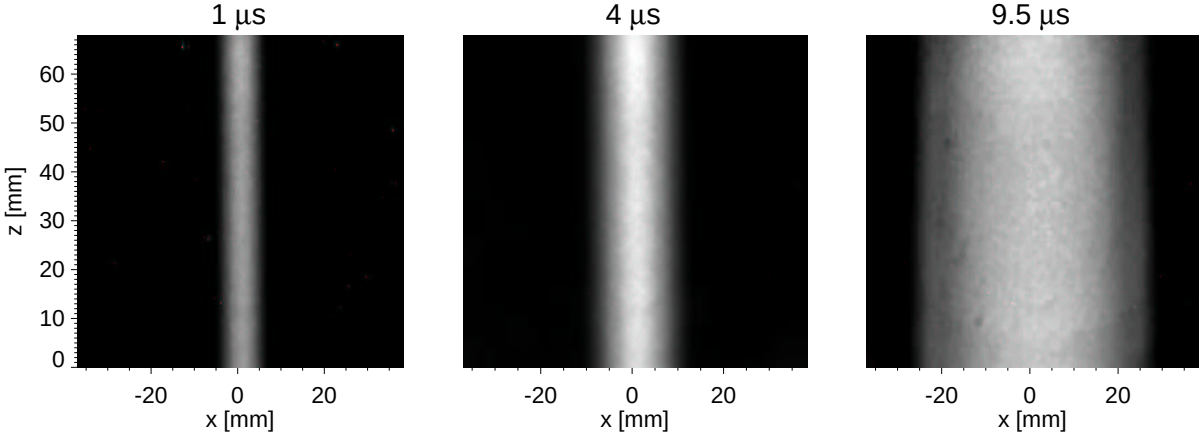

Figure 3.15: Fast shutter photographs of a 55 kA discharge in 5 mbar NH_3.

9 μs which is already during the negative half period of the current, the discharge shows no sign of instabilities. The same behaviour was observed without the prepulse in both gases.

The channel evolution and the discharge current are shown in figure 3.16 for a discharge with and without a preceding 10 kV prepulse. The channels with the prepulse are slightly bigger

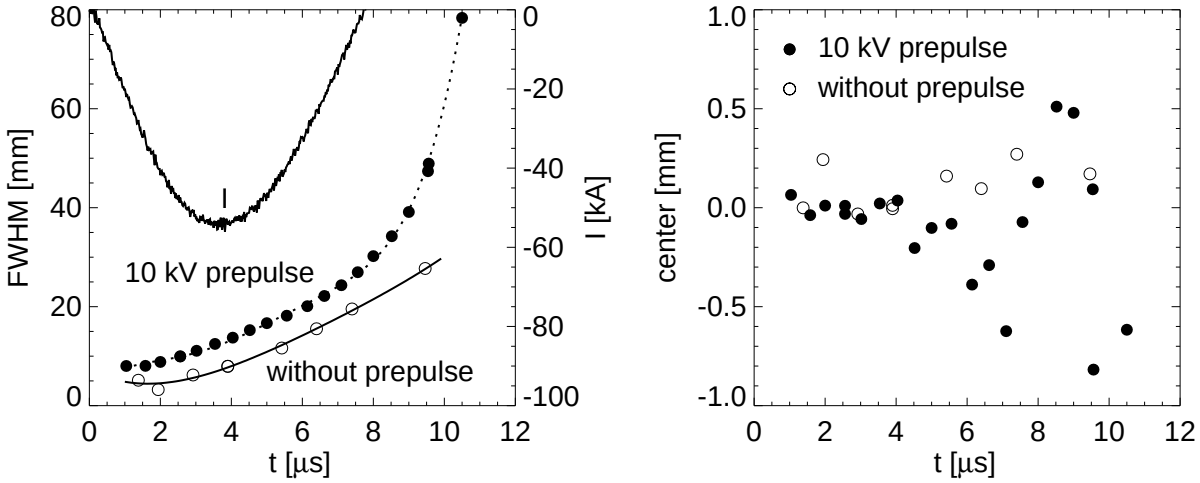

Figure 3.16: Channel evolution of a 55 kA discharge in 5 mbar NH_3.

than channels without because the prepulse discharge reduces the initial gas pressure for the main discharge, leading to a faster expansion. The channel diameter was determined from the FWHM of a Gaussfit to the plasma-self emission profiles. The center position of the channel shifts by a few 100 μm during the discharge (right graph of figure 3.16). This shift is more than a factor of three smaller than the shift in CO_2 laser initiated channels. If a prepulse is used, the position of the main discharge varies stronger in time than without. The rarefaction channel, which has a diameter of several mm allows the discharge to shift easier within this density depression. A variation of the discharge position by several 100 μm causes problems for an application in a fusion reactor, where the ion beam has to be guided to a small target. Also for diagnostics, measuring a certain plasma parameter at a fixed position at different times, a moving discharge becomes problematic since the relative radial position is continuously changing. For the Faraday rotation measurements presented in chapter 4.1.4 and measurements with magnetic probes [Pen02] the discharge position has to be known precisely at all times or the shifting must be suppressed as good as possible. Discharges in ammonia show the same behaviour. While the shift without the prepulse is less than 200 μm, the maximum displacement of the channel axis relative to the ion beam can be as much as 1 mm when a prepulse is used before the main discharge. In discharges without prepulse, the initial channel diameter is comparable to the size of the ion beamlet. A comparison of the channel evolution of discharges in 5 mbar NH_3 and 20 mbar Ar is shown in figure 3.17. Due to the higher mass the expansion velocity of discharges in

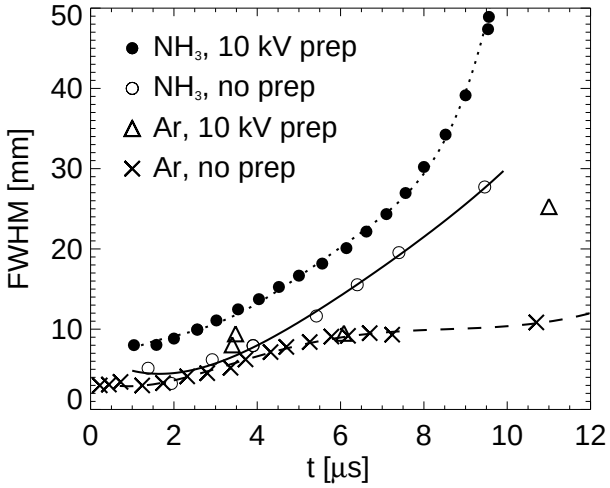

Figure 3.17: Comparison of discharges in 5 mbar NH_3 and 20 mbar Ar with and without prepulse.

argon is considerably smaller than in ammonia. However, measurements with magnetic probes inserted into the plasma have shown in a following beamtime, that for discharges in rare gases a considerable fraction of the discharge current flows outside the visible discharge channel in this configuration [Pen02].

The ion beamlet is deflected by the azimuthal magnetic field of the discharge. This field causes a force which is always directed towards the discharge axis. For an ion travelling exactly along the discharge axis the magnetic field vanishes and the ion will not be deflected. A combination of a fast plastic scintillator (BC 400) and an image intensified fast shutter camera was used to investigate the effect of the discharge on the beamlet. For a discharge aligned exactly to the ion beam axis, as it should be the case for an ion beam initiated discharge, the beamlet does not move at the scintillator during the discharge. If the channel position moves during the discharge, the beam spot at the scintillator follows this movement. An observation of the beam position at the scintillator represents a very sensitive method to detect movements of the discharge. The position of the beamlet at the scintillator was recorded in pictures with an exposure time of 10 μs, opening the camera 1 μs before the discharge ignites and closing after the first half current wave before the current is reversed. Figure 3.18 shows the time-integrated movement of the beamlet for a 55 kA discharge in ammonia with and without prepulse. During discharges

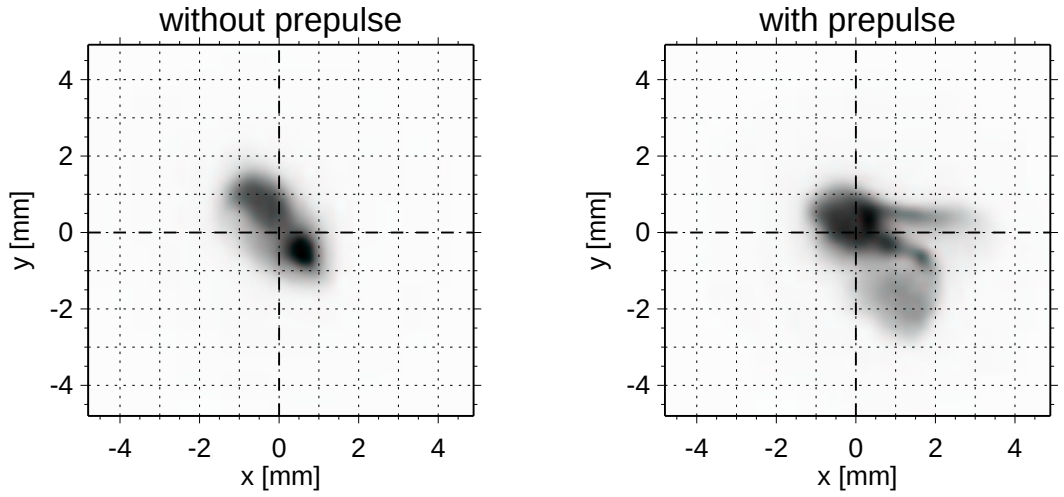

Figure 3.18: Light emission recorded from a fast plastic scintillator during the first half period of the discharge in ammonia with and without prepulse. The exposure time was 10 μs.

without prepulse, the beamspot does not move by more than 1 mm across the scintillator, indicating that the discharge axis is always aligned closely to the beam axis. If a prepulse is used, the beamlet is deviated by up to 3 mm from the initial position. These larger shifts compared to the movement of the discharge measured by fast shutter imaging (figure 3.16) can be explained if the discharge is not only shifting vertically but is actually tilting so that the displacement near the scintillator is bigger than in the center of the channel where the fast-shutter images are recorded. The movement of the main-discharge after the prepulse is not reproducible from shot to shot. If the CO_2 laser is fired into the gas before the discharge is triggered, the channel follows the laser path rather than the ion beam axis (figure 3.19). The discharge moves by several millimeters causing the beamlet to follow its axis. Two focal spots can be seen where the intensity is higher, indicating exactly the discharge axis. The laser beam can be aligned to the beam axis by adjusting the laser mirrors to minimize the movement of the beamlet. However, the overall motion of the discharge itself is always bigger with laser initiation than with ion beam initiation. Discharges in argon show again the same behaviour. The ion beam scattering is more pronounced due to the higher mass of the gas, therefore the pictures look more smoothed. A pure main-discharge does not show any significant movement of the beamlet during the first half

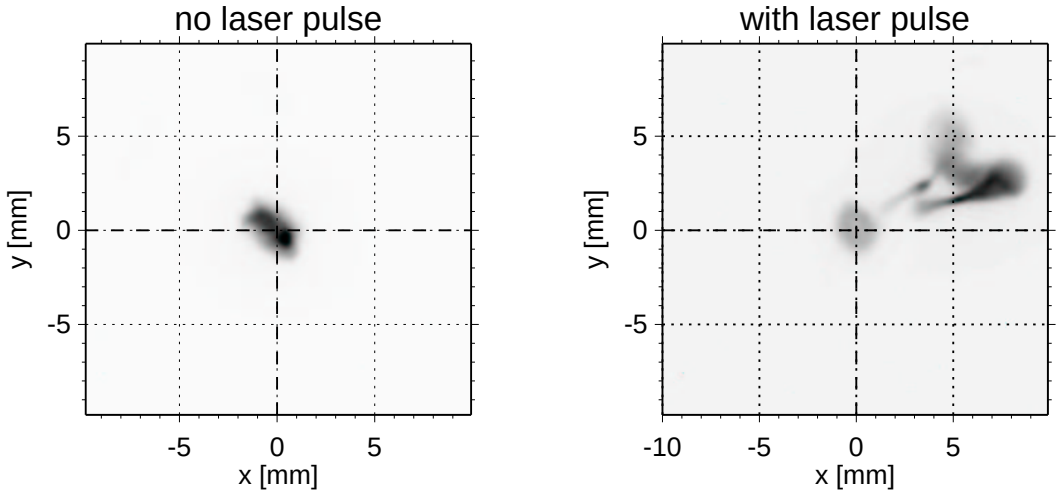

Figure 3.19: Light emission recorded from a fast plastic scintillator during the first half period of the discharge in NH_3, with and without laser pulse. No additional prepulse was applied.

period. An additional prepulse shifts the discharge by several millimeters during the first half period (figure 3.20).

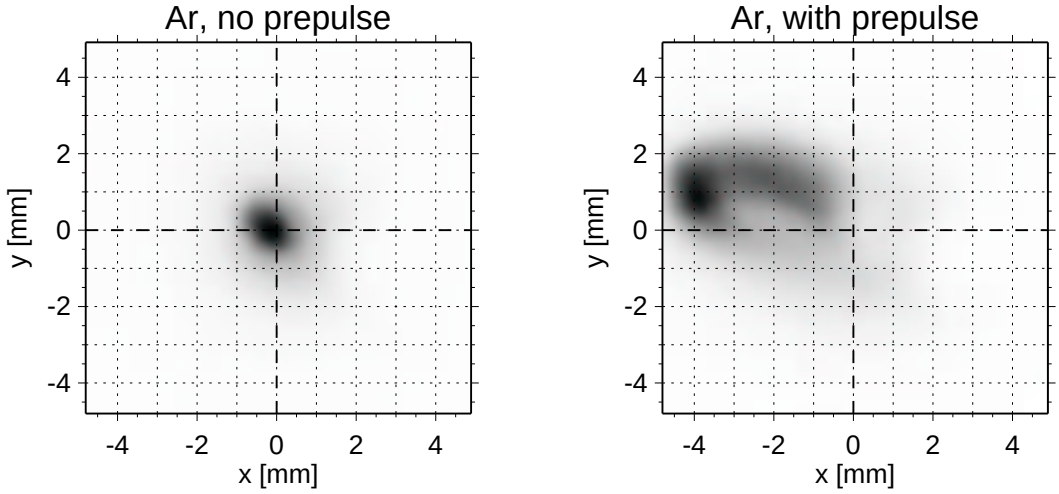

Figure 3.20: Comparison of the time integrated motion of the beamlet in a 20 mbar Ar discharge with and without preceeding 10 kV prepulse.

These preliminary measurements show that ion beam initiated transport channels are in many respects superior to laser initiated channels. The stability of those channels, even without the creation of a gas-rarefaction zone could be explained with the very symmetric initial conditions of the discharge. If the ionization channel created by the ion beam reduces the initial disturbances of the discharge to a minimum, even a large MHD-instability growth rate would require a long time to develop instabilities. (Detailed measurements of ion beam initiated channels will be described elsewhere [Nef02, Pen02]).

Chapter 4

Channel Diagnostics

For an understanding of the channel dynamics and stability, the plasma has to be diagnosed with techniques extending the simple fast-shutter photographs and electric measurements described so far. Detailed experimental data of discharges at different parameters are crucial for benchmarking simulation codes like CYCLOPS which can later be used to predict the performance of discharge channels beyond the scope of the present experimental capabilities and to engineer channels adapted to a certain application.

This chapter summarizes several diagnostic techniques, which were applied to measure different plasma parameters at the channel experiments at GSI and Berkeley. Most of the techniques rely on measurements of the refractive index, which depends in a plasma strongly on the electron density. Chapter 4.1.1 describes an imaging interferometer which was used at GSI to determine the electron density with spatial resolution. Measurements at two wavelengths allow also an estimation of the gas density, and show a radially expanding gas wall as well as the rarefaction channel created by the laser or the prepulse discharge, which plays an important role for the stability and initiation of the discharges. The expanding density wave was studied in detail by the schlieren and shadowgraphy techniques both at Berkeley and at GSI (chapter 4.1.3).

The plasma self emission of the channels at GSI was investigated by spectroscopy in the visible range (chapter 4.2). Measurements of the Stark broadening of the Hydrogen-Balmer lines represents another means to determine the electron density for a comparison with the data from the interferometer. A rate model was developed (chapter 4.2.3) to calculate the population densities of different energy levels, to fit the experimental spectra and to obtain the electron temperature. A measure of the conductivity, which depends mainly on the temperature is crucial for an understanding of the charge neutralization of space charge dominated ion beams propagating through the plasma (chapter 2.4).

The ion optical properties for single particles are determined by the magnetic field inside the plasma and thus by the current density distribution. Chapter 4.1.4 describes a Faraday polarimeter which was developed at Berkeley to measure the magnetic field inside the channel without disturbing the plasma. The small rotation angles require a big experimental effort. The performance of the whole setup and the first preliminary measurements are presented. An unconventional method to obtain information about the magnetic field, using the ion beam from the GSI-UNILAC linear accelerator as probe, will be described in chapter 5.
Unless stated otherwise, described measurements were preformed at the GSI experiment.

4.1 Refractive index measurements

In a plasma, the refractive index is primarily a function of the electron density, which is the main plasma parameter determined by refractive-index measurements. Typical plasma diagnostics based on refractive effects include interferometry, schlieren imaging, shadowgraphy and Faraday rotation measurements. While the first technique gives a direct measure of the refractive index μ, the schlieren and the shadowgraphy techniques probe the gradient $d\mu/dx$. The Faraday-rotation technique is based on the birefringence of a plasma under the influence of a magnetic field and thus causes a rotation of the plane of polarization of a linearly polarized wave penetrating the plasma.

An electromagnetic wave exerts a force on the charged constituents of the medium through which it propagates. This force accelerates the charges which in turn modify the time-varying electromagnetic field. A solution of an electromagnetic wave in a plasma can be obtained by solving the wave equation for a plane wave in the small amplitude approximation [Jah71]. The plasma-refractive index follows then as

$$\mu = \left(1 - \frac{\omega_p^2}{\omega^2(1 \pm \omega_e/\omega)[1 - i(\nu\omega)]}\right)^{1/2}, \tag{4.1}$$

where $\omega = 2\pi c/\lambda$ is the frequency of the electromagnetic wave, $\omega_p = (n_e e^2/\epsilon_0 m_e)^{1/2}$ the *electron plasma frequency* and ν the effective number of collisions per second that an electron makes with heavy particles.

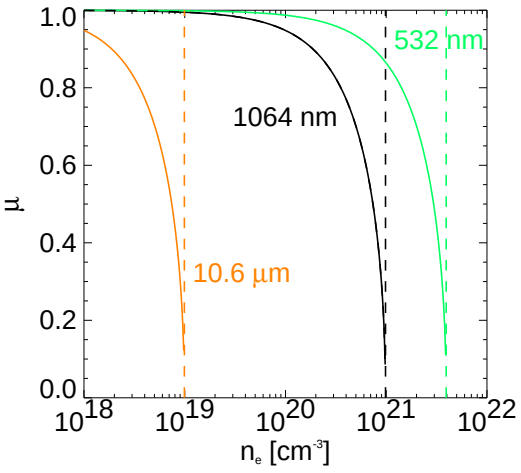

Figure 4.1: Refractive index as a function of electron density for the lasers used in the experiments.

The effect of a static applied magnetic field B_0 is expressed by the *electron cyclotron frequency* $\omega_e = eB_0/(m_e c)$. In the special case of negligible magnetic field and collisions equation 4.1 simplifies to

$$\mu_{\text{electrons}} = \sqrt{1 - \frac{\omega_p^2}{\omega^2}} = \sqrt{1 - \frac{n_e}{n_c}}, \tag{4.2}$$

where

$$n_c = \frac{4\pi^2 c^2 \epsilon_0 m_e}{e^2 \lambda^2} = \frac{\pi}{r_e \lambda^2} \tag{4.3}$$

is the cutoff density and $r_e = e^2/(4\pi\epsilon_0 m_e c^2) = 2.818 \cdot 10^{-15}\ m$ is the classical electron radius. At an electron density approaching n_c the refractive index becomes zero and the wave cannot penetrate the plasma any more. In experiments lasers are used typically as light source due to their coherence, brightness and small bandwidth. The dependence of the refractive index on the plasma density for different laser wavelengths is illustrated in figure 4.1. The cutoff density is marked by the vertical line for each wavelength. The cutoff density for 1064 nm is around $10^{21}\ cm^{-3}$ which is well above the densities encountered in the channel plasma.

The index of refraction for a neutral gas or dissociated atoms is given by the Gladstone-Dale relation [Mer81]

$$\mu_{\text{gas}} = 1 + K(\lambda) \cdot \frac{\rho}{\rho_{atm}}, \tag{4.4}$$

where $K(\lambda)$ is a gas specific constant, ρ the gas density and ρ_{atm} the gas density at atmospheric pressure. Equation 4.4 can be derived using a model of a harmonic electron oscillator. Apart from the immediate neighborhood of the resonance frequencies of the gas, K is only weakly

dispersive. Near an absorption frequency μ becomes complex, with the imaginary part representing the light absorption in the gas. The exact Gladstone-Dale relation for this wavelength range must be derived from a quantum mechanical solution for the refractive index. Close to a resonant wavelength, the gas exhibits anomalous dispersive behaviour with K being many orders of magnitude higher than in the non-resonant case [Mer81]. For ammonia gas the used wavelengths of 532 and 1064 nm are situated far away from resonances. The Gladstone-Dale constant of ammonia gas at a pressure of one atmosphere and a temperature of 25^oC in the visible wavelength region is $K = 3 \cdot 10^{-3}$ [Uni95].

4.1.1 Two-color imaging interferometry

The discharge plasma of both channel experiments was investigated by an imaging interferometer of the Michelson type. The interferometer at GSI was designed after a very similar setup at Berkeley [Pon01, Pon02]. The GSI interferometer was operated at two different wavelengths to measure both the electron and the neutral gas density in the discharge as well as the gas density of the laser heated gas with spatial and temporal evolution.

Experimental setup

The experimental arrangement is shown in figure 4.2. A Q-switched Nd:YAG laser (New-wave

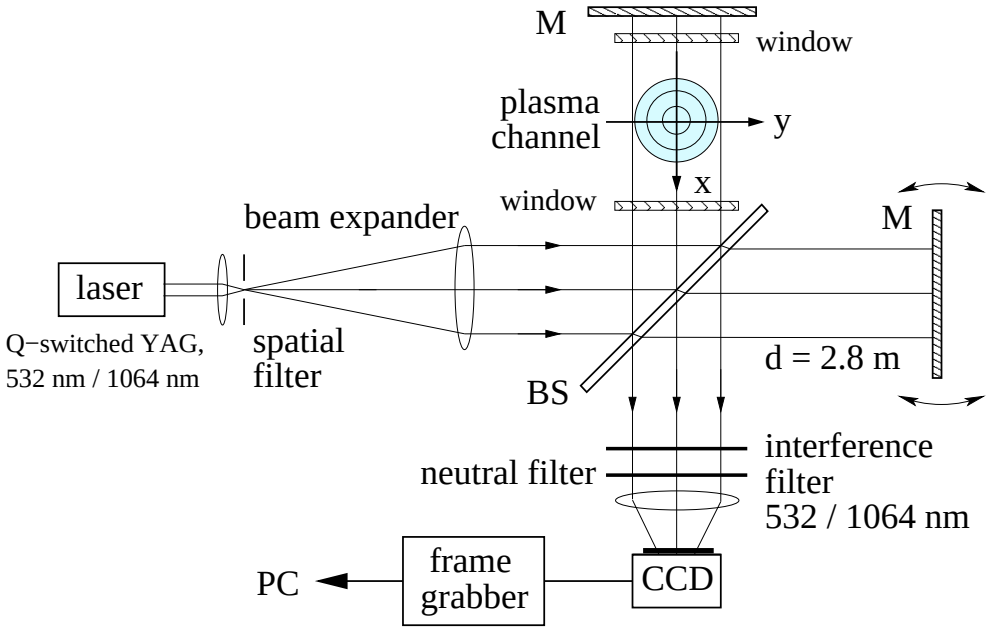

Figure 4.2: Setup of the Michelson interferometer.

Minilase I) at either 1064 nm or the first harmonic at 532 nm in a 5 ns pulse is enlarged by two telescopes to a parallel beam of more than 200 mm size. Two 20 μm pinholes in the foci of the telescopes, clean the beam from non-Gaussian contributions and improve the beam quality. While most of the beam is blocked by an aperture the remaining central 50 mm diameter beam with a Gaussian wavefront is split in two by a 50/50 beam splitter. One beam probes the plasma twice side-on and is then recombined with the undisturbed reference beam at the beam splitter. Both arms of the interferometer with a length of roughly 2.8 m must be adjusted to the same optical length within a few millimeters, since the coherence length of the pulsed laser, determined by the bandwidth, is only 7 mm. A mismatch of the two wavefronts by one coherence length causes a drop of the fringe contrast by a factor of 1/e. The two vacuum windows on either side of the channel are slightly tilted relative to the laser-beam axis to avoid

ghost images due to reflections. An interference filter for either 532 nm or 1064 nm and a neutral filter with a transmission of 10^{-5} are used to screen the plasma - self emission. The image is then recorded by a low cost CCD camera (Phytec VCAM-020) and digitized by a frame grabber (Matrix Sigma-SLG). The camera operates with an exposure time of 1/128 s which maximizes the time window for the recording of the laser pulse. However, the time resolution is set by the 5 ns pulse duration of the laser. Therefore it is not necessary to use a fast shutter camera, which is usually blind at 1064 nm because of the photo cathode which was used. The use of neutral filters is necessary to block the discharge light which is transmitted through the bandpass filter and integrated by the low-speed CCD camera over the entire discharge time during 1/128 s. A laser output with an energy of a few mJ per pulse is more than sufficient to outreach the remaining plasma-self emission by orders of magnitude and to give enough laser power onto the CCD detector. A camera objective images the position of the channel onto the CCD chip. The Michelson-style arrangement was preferred here because of its simplicity and its high sensitivity. The laser probes the plasma twice and the fringe shift will be twice as big as for e.g. a Mach Zehnder interferometer. Both the incoming and the reflected beam are aligned to exactly overlap within a few 100 μm to assure the desired spatial resolution. The mirror for the reference beam is slightly tilted relative to the laser beam axis. In this way a fringe pattern with the number of fringes proportional to the tilting angle is observed. If the angle is too large the fringes disappear. A tilting of the mirror in the other plane rotates the fringe pattern. In the measurements the null fringe pattern was arranged to show typically between 5 to 10 fringes in the whole field of view perpendicular to the channel axis. Since the laser can operate at two different wavelengths it is possible to distinguish between the electron density and the neutral gas density which affect the index of refraction in different ways (equations 4.2 and 4.4). The refractive index for a certain electron density increases with the laser wavelength λ. Electrons have by far, especially at 1064 nm, the largest contribution to the refractive index. The reproducibility of the discharge allows in practice to perform the measurements for certain discharge parameters independently, at each wavelength, in different shots. In a somewhat improved apparatus with an additional beam splitter and a second camera the measurement could also be performed for both wavelengths at the same time.

Fringe pattern analysis

The refractive index and thus the electron density follows from an evaluation of the measured fringe shift pattern. The fractional fringe shift $K(y)$ is determined by a computer program which traces and averages several fringes by Gauss fits for each fringe and y as shown in figure 4.3. In this way the accuracy which usually depends on the quality of the optics with a minimum planarity of $\lambda/2$, is improved considerably if the z symmetric discharge does not vary across the interferogram. The position of the null fringes before the plasma channel formation is obtained from the region outside the plasma where the refractive index remains unchanged. When the channel expands until it covers the entire field of view, the absolute fringe shift can not be measured any more. The 40 mm window allows to perform measurements up to 8 μs after the breakdown depending on the pressure. Later times are of minor interest for ion beam transport experiments. The optical stability of the entire setup does not allow to determine the null-fringe position from a separate calibration picture taken shortly before the discharge since the fringes change their position from shot to shot.

Since the pictures are recorded side-on the fringe shift $K(y)$ for a given change in refractive index $\Delta\mu(r)$ follows from an integration over the whole line of sight

$$K(y) = 2 \cdot \frac{1}{\lambda} \int_{x_1}^{x_2} \Delta\mu(r) \cdot dx, \tag{4.5}$$

where λ is the laser wavelength, and $x_{1,2}$ the boundary positions of the plasma channel. The

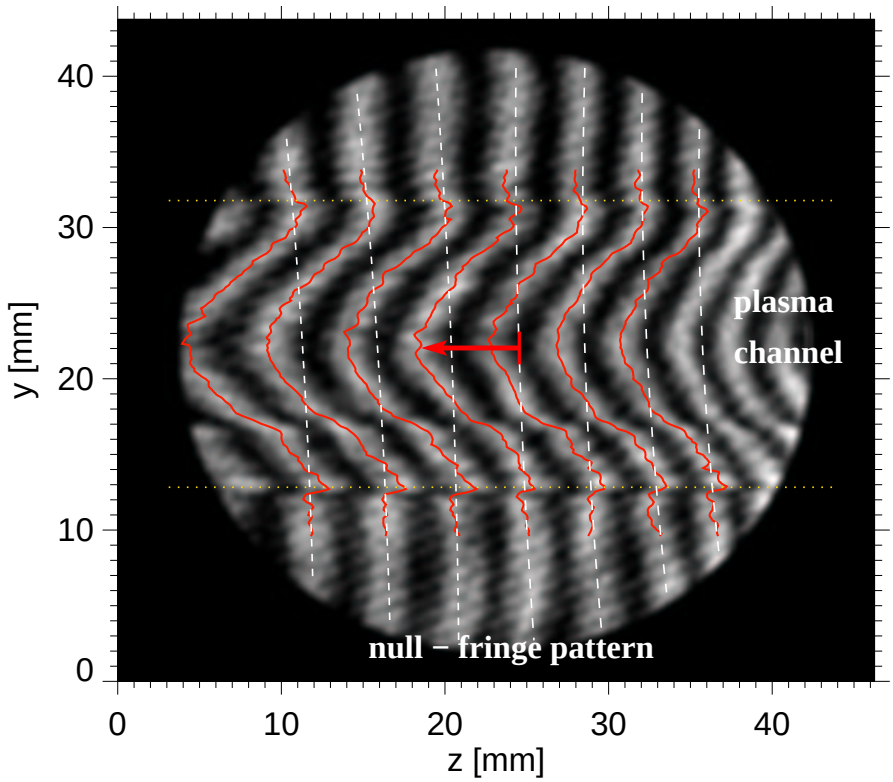

Figure 4.3: A typical fringe pattern during a discharge. The fractional fringe shift is determined by a computer program which traces several fringes (red lines). The null fringe position (white dashed lines) is subtracted and the fractional fringe shift is calculated from the fringe spacing.

factor 2 accounts for the fact that the laser probes the plasma twice. Since the plasma has a cylindrical symmetry, equation 4.5 can be rewritten as an Abel integral equation [Hut81]

$$K(y) = \frac{4}{\lambda} \int_y^R \frac{\Delta\mu(r) \cdot r}{\sqrt{r^2 - y^2}} dr \ , \tag{4.6}$$

where the integration has to be performed from the position of interest y to the outer radius R of the plasma cylinder. The radial dependence follows from the inversion of equation 4.6

$$\Delta\mu(r) = -\frac{\lambda}{2\pi} \int_r^R \frac{dK(y)}{dy} \cdot \frac{dy}{\sqrt{y^2 - r^2}} \ , \tag{4.7}$$

which is called the 'Abel inversion' [Hut81]. Many different methods have been developed for a numerical Abel inversion [Ahm81, Tho95]. In this case the radial distribution was calculated by a matrix method from a discrete set of 20 data points equally distributed from the center of the channel (y=0) to the outer edge (y=R) [Tho95] as shown in figure 4.4. The total refractive index is then given by

$$\mu(r) = \mu_0 + \Delta\mu(r) \ , \tag{4.8}$$

where μ_0 is the refractive index of the gas filled chamber before the plasma channel is formed determined by the gas pressure (equation 4.4). The refractive index change $\Delta\mu$ is negative for the contributions from the electrons and positive for the contribution from the gas. In the case

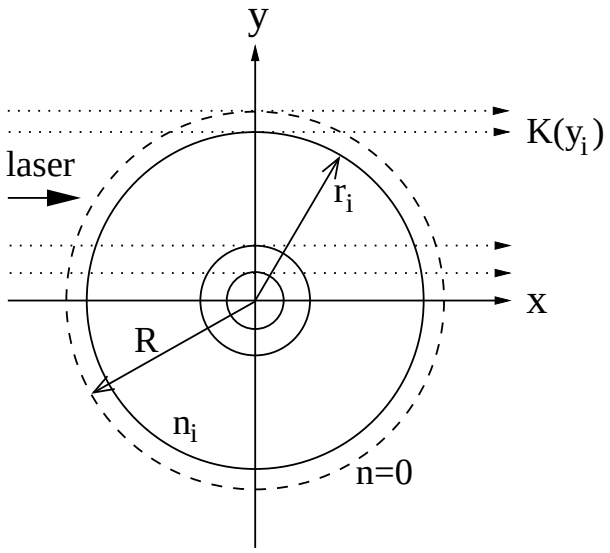

Figure 4.4: Geometry of the Abel inversion problem.

of negligible contribution from the neutral gas the electron density follows from equation 4.2 as

$$n_e = \frac{\pi(1-\mu^2)}{\lambda^2 \cdot r_e} \tag{4.9}$$

Since the Abel inversion (equation 4.7) is only valid for axial symmetric plasmas, only one half of the fringe shift profile from $y = 0$ to y_{max} must be considered. In practice both halfs are averaged. However, the difference between the two halfs is even for unstable discharges minor. The error in fringes obtained from the fringe counting procedure is used to estimate an error in the Abel inverse. In this case the Abel inverse is performed three times using the profiles of the average, the maximum and the minimum fringe shift. The obtained density limits are used as error bars. This estimation gives only a lower limit of the error.

Measurement of the electron density

Figure 4.5 (a) compares the measured fringe shift profiles of a 45 kA discharge in 5 mbar ammonia recorded 3.5 μs after the breakdown, at both laser wavelengths. At this time a maximum fringe shift of around 1.5 fringes is observed at a wavelength of 1064 nm. In the measurement at 532 nm the fringe shift is only half as big. At the edge of the plasma channel a narrow region with a positive fringe shift of around 0.1 fringes (indicated in red) can clearly be identified at 532 nm, which is caused by a gas wall pushed outwards by the expanding plasma column. Figure 4.5 (b) shows the Abel inverted electron density profiles obtained for 532 nm and 1064 nm from equation 4.9 with the assumption that μ inside the plasma is only determined by the plasma electron density. The gas wall was excluded from the Abel inversion by setting the fringe shift artificially to zero from the positive values. Both measurements agree within a few percent although the interferograms were taken in two independent discharges performed with an interruption of several weeks. This result justifies the assumption that the refractive index inside the plasma is determined mainly by the electron density within the precision of the measurement. The gas wall is also visible in the measurements at 1064 nm but the fringe shift is considerably smaller.

In the following the Abel inverted electron density profiles for different discharge conditions are determined from the 1064 nm measurements since the fringe shift is bigger and thus the accuracy is better. However, in all cases the density derived from the interferograms taken at 532 nm shows roughly the same profile. The temporal evolution of the electron density distribution for discharges at 5, 10, 15 and 20 mbar ammonia is summarized in figure 4.6. While

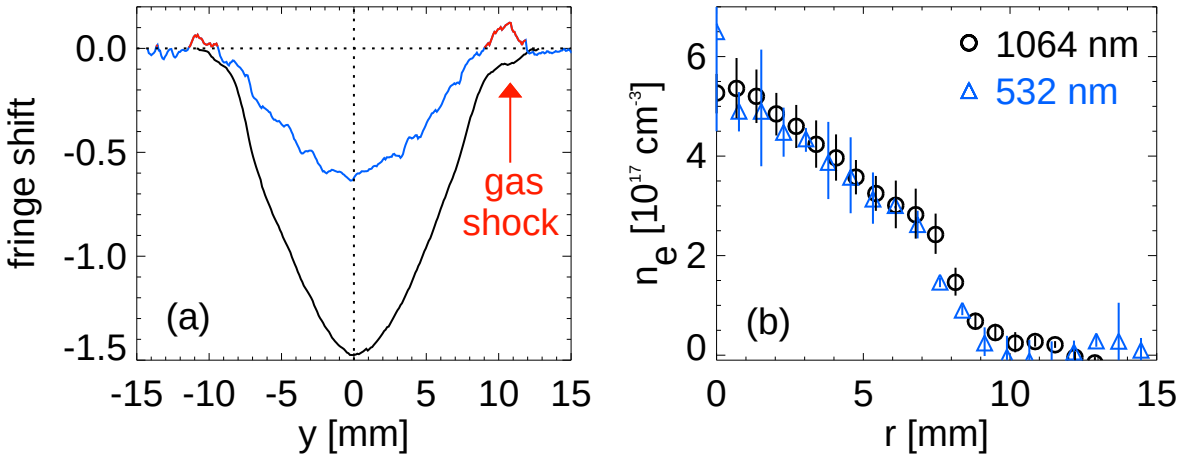

Figure 4.5: Comparison of the fringe shift (a) and the Abel inverted electron density (b) at 532 nm (blue) and 1064 nm (black) in a 45 kA / 5 mbar discharge without prepulse, 3.5 μs after the breakdown. The positive fringe shift in the 532 nm measurement indicates the gas shock.

the diameter of the channel is steadily increasing the on-axis density shows a maximum at around 4 μs just at the time of the current maximum. At all pressures a distinct shoulder at the edge of the channel is formed after a few μs which remains for the rest of the examined time interval. At a pressure below 10 mbar a central density depression is observed around the time of the first pinch (curves for 1.96 μs at 5 mbar, and for 1.84 μs at 10 mbar in figure 4.6) surrounded by a region of higher electron density. This distribution may be due to the skin effect (chapter 2.1.3) which concentrates the current flow at the edge of the channel. At higher pressures ($\geq$ 15 mbar) the density shows a steep profile at early times with the gradient increasing towards the channel axis. This behaviour is already visible in the interferograms which show an almost triangular fringe pattern. After the current maximum the profile flattens while the shoulder at the edge of the channel is formed. At times later than 5 to 6 μs an almost homogeneous electron density is measured in the central half of the channel. The electron density distribution inside a 20 kA discharge or in discharges with a preceding low energy prepulse shows the same behaviour. Both the density depression around the pinch time as well as the shoulder at later times are observed also at this current.

The temporal evolution of the central electron density is plotted in figures 4.7 and 4.8. The density was determined both at 532 nm (triangles) and 1064 nm (circles) using equation 4.9 with the assumption that $\mu_{gas} = 1$. Figure 4.7 compares the density in a 45 kA discharge at a pressure of 5 mbar, 10 mbar, 15 mbar and 20 mbar. In all cases the electron density peaks at around 4 μs which is also the time of the current maximum. The highest density reached at 5 mbar is around $5 \cdot 10^{17}$ cm^{-3}. This corresponds to half of the number of electrons contained in the ammonia gas at this pressure, which indicates, that nitrogen must be present as NIV. The electron density scales roughly with the initial gas pressure, reaching around 10^{18} cm^{-3} at 10 mbar, $1.5 \cdot 10^{18}$ cm^{-3} at 15 mbar and $2 \cdot 10^{18}$ cm^{-3} at 20 mbar. Therefore the degree of ionization does not depend on the pressure within the accuracy of the measurement. Each data point in figure 4.7 to 4.8 was obtained from a separate discharge, a fringe pattern analysis and an Abel inversion. The points are scattered strongly, indicating that the actual error is much bigger than the error bars. This is partially due to the fact that the undisturbed fringes are not always perfectly straight and an absolute reference could not be taken, since the unstable optical setup causes the fringes to move from shot to shot. The error bars do not contain systematic errors caused by a curvature of the reference fringes. The Abel inversion routine represents

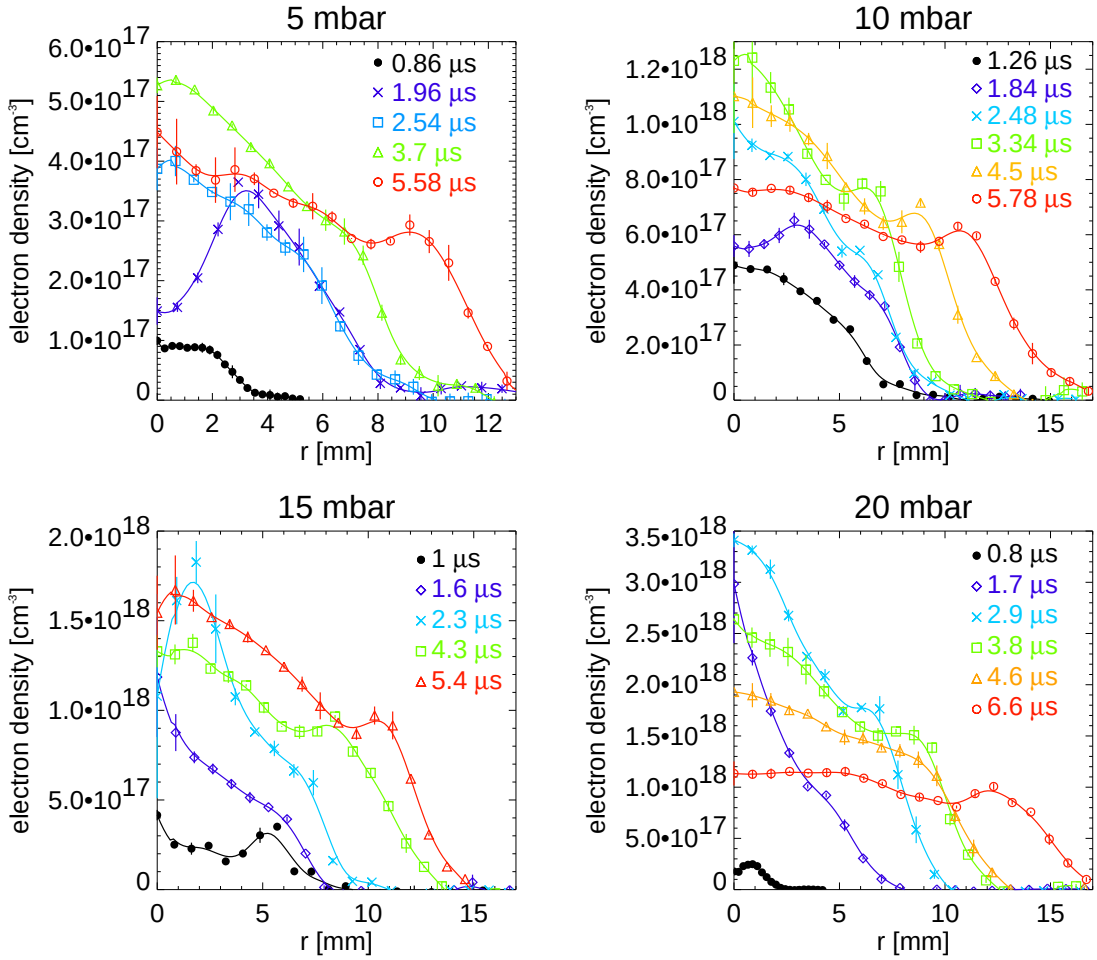

Figure 4.6: Electron density profiles in a 5, 10, 15 and 20 mbar 45 kA discharge without prepulse at different times. The distinct shoulder at the edge of the channel is for all pressures especially at late times clearly visible.

another error source. Since the profiles are described by only 20 discrete data points, the error is especially in the center very big. An integrated line density value would give a more precise density parameter.

A comparison of the central density for discharges in 10 mbar at different discharge currents is shown in figure 4.8. At a lower current of 20 kA (black) the density is smaller by roughly a factor of two. The density maximum is reached earlier at around 2 to 3 μs which is also the time of the current maximum at this bank capacity. The effect of the prepulse on the electron density profile is illustrated in figure 4.9 for two different times after the breakdown. All three interferograms were taken at 1 ± 0.1 μs and $4 \pm$ $0.1 \mu s$. At the beginning of the discharge (1 μs) the channel has a bigger diameter when a prepulse is used. After the current maximum (4 μs) the channel diameter does not depend on the prepulse voltage any more. This is in agreement with the fast shutter images of the plasma light emission (page 19). After the pinch at around 2 μs also the density profile and especially the position of the shoulder does not depend on the prepulse voltage.

Gas density measurements

The height of the neutral gas wall which was already mentioned in figure 4.5 can be estimated from the fringe shift measured at 532 nm by the Gladstone-Dale relation (equation 4.4). The

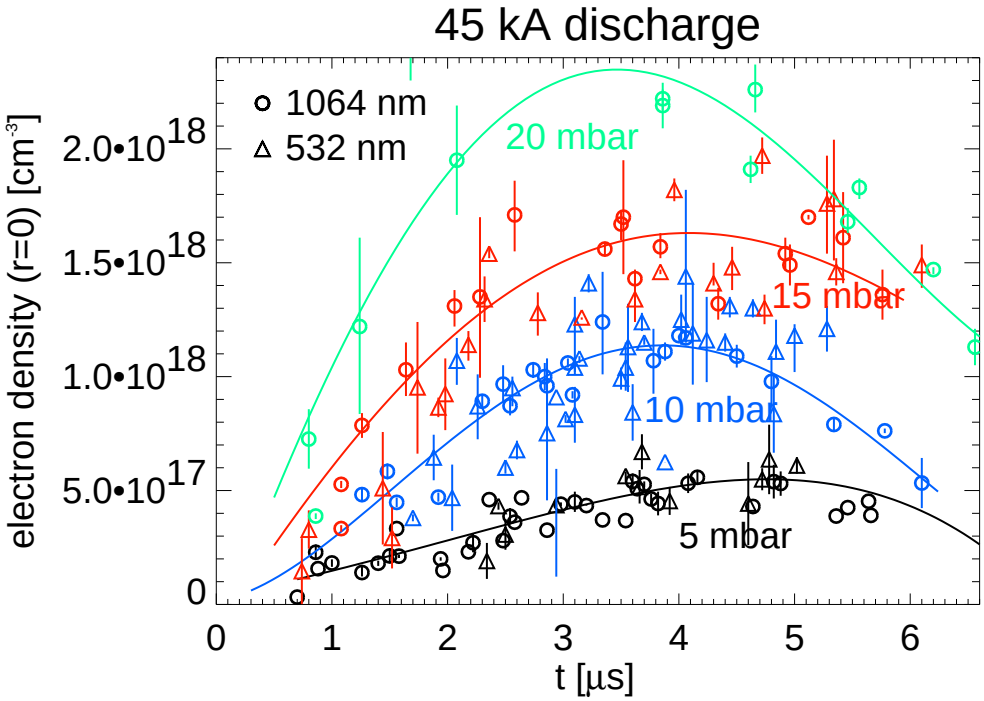

Figure 4.7: Time evolution of the electron density on the discharge axis for a 45 kA discharge in 5, 10 15 and 20 mbar pressure without pre-discharge.

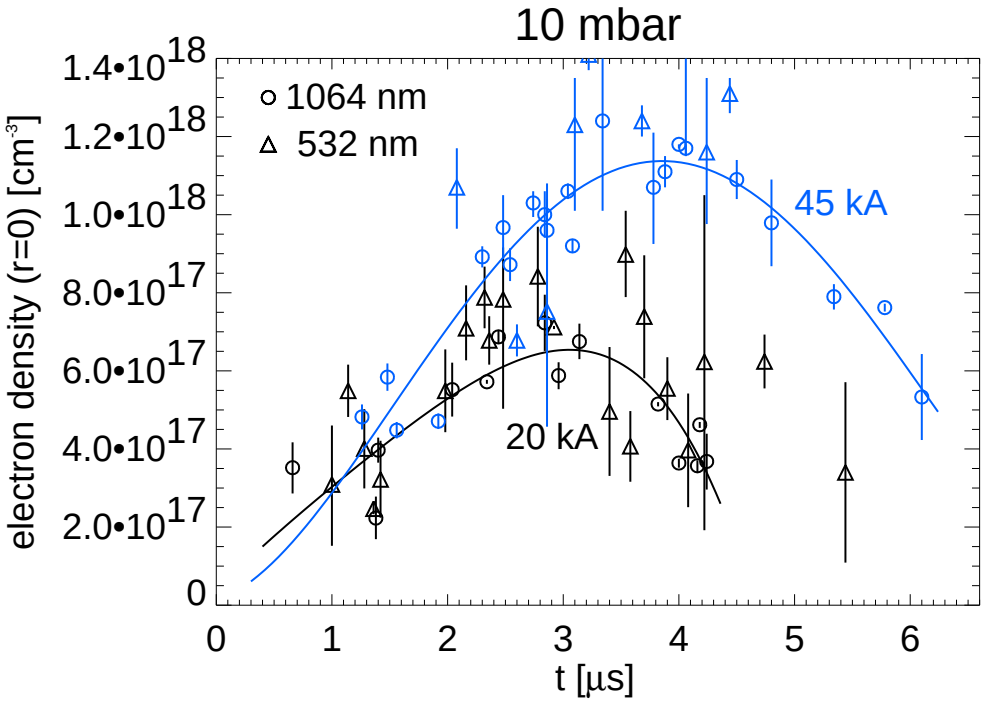

Figure 4.8: Comparison of the on-axis electron density at 10 mbar for a 20 and a 45 kA discharge without prepulse.

ratio between the gas density ρ and the initial density ρ_0 at this pressure is then given by

$$\frac{\rho}{\rho_0} = \frac{(\mu_0 - 1) - \Delta\mu}{\mu_0 - 1}, \tag{4.10}$$

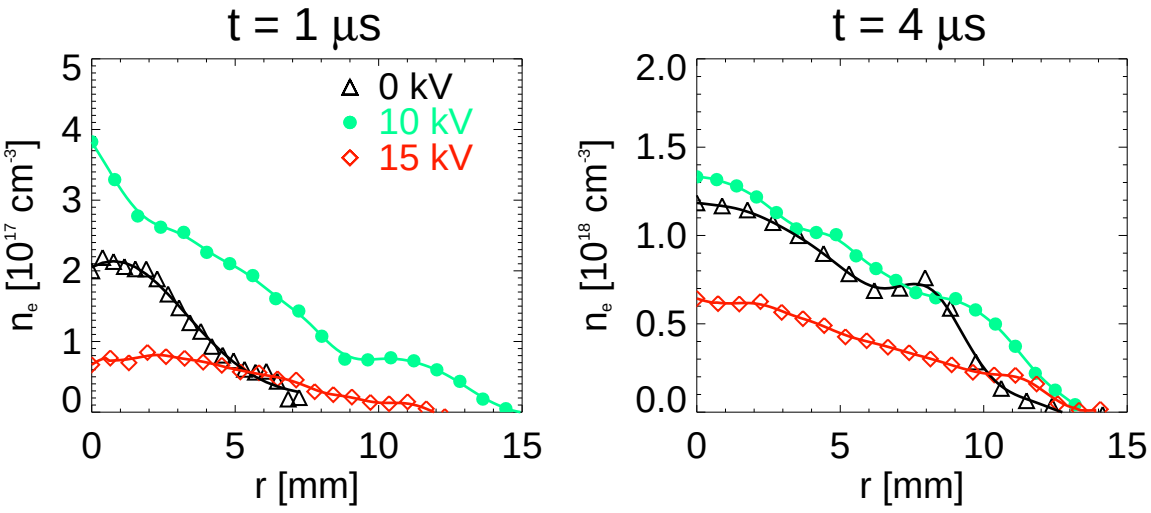

Figure 4.9: Comparison of the electron density profile of 45 kA discharges in 10 mbar ammonia without prepulse (black), with a 10 kV prepulse (green) and 15 kV prepulse (red).

where the refractive index at the pressure p is calculated by

$$\mu_0 = 1 + K \cdot \frac{p}{1\ \text{atm}}. \tag{4.11}$$

In this case the contribution from the electrons was excluded from the Abel inversion by artificially setting the fringe shift to zero inside the wall. Figure 4.10 shows the fringe shift as well as the Abel inverted neutral gas density for the discharge from figure 4.5. Although the

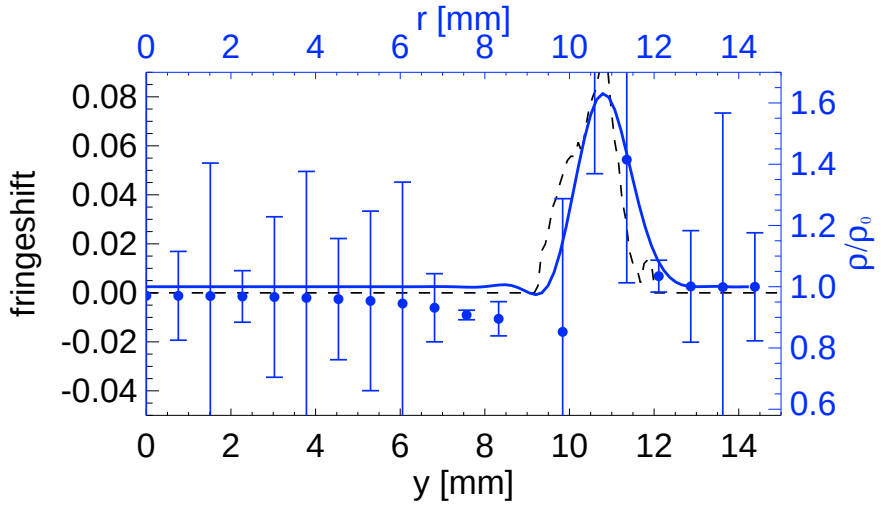

Figure 4.10: Fringe shift caused by the neutral gas shock in a 45 kA discharge in 5 mbar ammonia (black dotted line). The Abel inverted gas density is shown in blue.

fringe shift is only 1/10 fringes which is comparable to the error it can be estimated that the density in the wall is roughly by a factor of 1.5 higher than the initial density at 5 mbar. The higher the initial gas pressure, the stronger and faster is the gas shock. Figure 4.11 shows the Abel inverted neutral gas density in a 45 kA discharge in 15 mbar at different times. Both the radial expansion as well as an increase of the shock density can clearly be observed. The highest compression ρ/ρ_0 in the shock is around 4 at a time of 5 μs. This gas shock, which is visible for discharges without prepulse and surrounds the plasma column, plays an important role for the

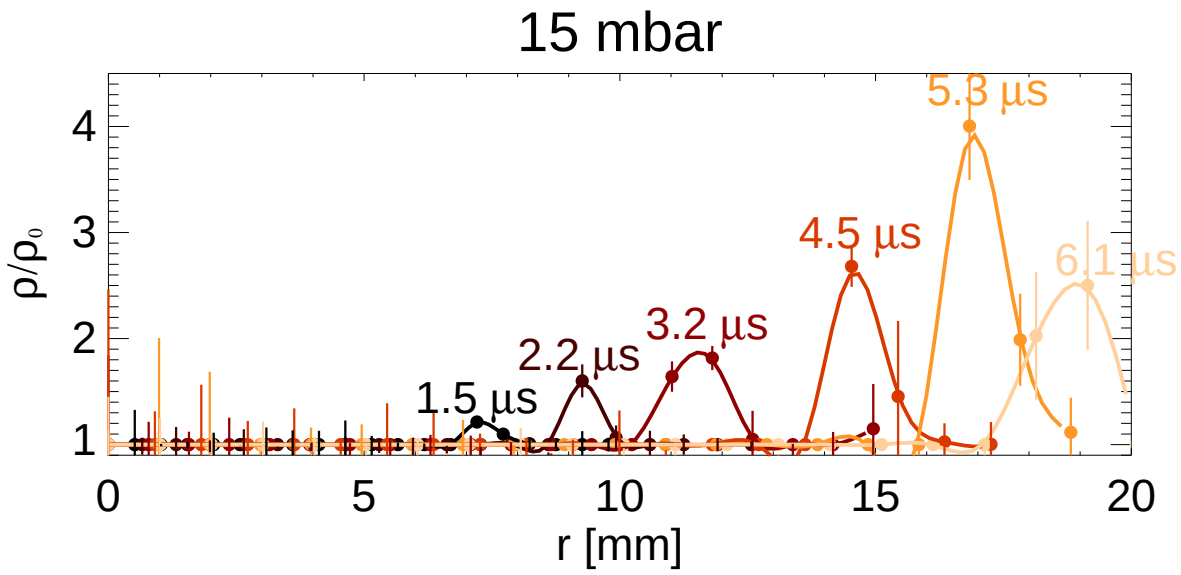

Figure 4.11: Evolution of the radial neutral density profile in a 45 kA discharge in 15 mbar ammonia. A radially expanding shock is visible with an increasing shock density.

stability of the discharge channel as already mentioned in chapter 3.1.4. The additional mass density outside the current carrying region stabilizes the channel and decreases the growth rate of MHD instabilities [Man73].

Neutral-gas density measurements in the low energy prepulse

Also during the low current prepulse discharge a small fringe shift can be measured at both wavelengths. While at 532 nm the shift is in the order of 0.4 fringes, the shift is roughly half at 1064 nm. In analogy to the measurements of the laser rarefaction channel it can therefore be assumed that this shift is caused mainly by changes of the neutral gas density. The small shift which is not much bigger than the error does here not allow to rule out any small contribution from plasma electrons. An interferogram recorded in a 15 kV prepulse in 15 mbar ammonia is shown in figure 4.12 (a). The picture shows the gas shock surrounding a channel of reduced gas density. The Abel inverted density profiles for different times are shown in figure 4.12 (b). The wall has a width of about 1mm and expands radially with a velocity around 1 $mm/\mu s$. The peak density in the shock reaches twice the initial value at 15 mbar. The shock leaves a low density channel behind with the density reduced by around 80 percent. The size of the rarefaction channel grows as the shock expands and reaches a diameter of 20 mm at a time of 6 μs after the breakdown. A similar behaviour is measured for a 10 kV prepulse in 10 mbar ammonia (figure 4.13). Since less than half the energy is dumped into the gas the shock and the formed density depression are less pronounced. The highest density reached in the shock is around 1.4 times the initial density at 10 mbar. The density in the rarefaction channel decreases from 50 percent of the initial value shortly after the breakdown down to 80 percent after 8 μs.

If the high current discharge is triggered 15 to 50 μs after the prepulse where the shock has disappeared, the gas is already strongly rarified and a second pronounced shock can not be formed. In the interferograms no sign of a gas shock was visible both at 1064 nm and 532 nm at any pressure when a prepulse was used before the high current discharge. This is also in agreement with the interferometric measurements at Berkeley [Pon01, Pon02], where a prepulse is always used. Without a surrounding gas wall the channels are consequently less stable than discharges with such a wall, where the prepulse is not used. This was also confirmed

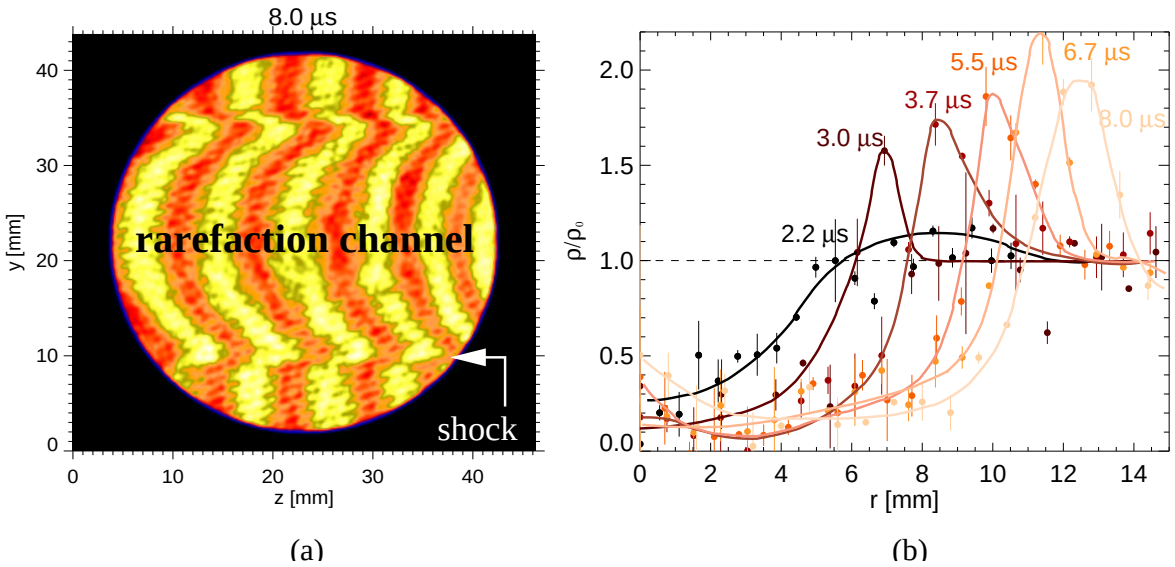

Figure 4.12: (a) Interferogram of a 15 kV prepulse in 15 mbar ammonia. (b) The Abel inverted neutral gas density for different times.

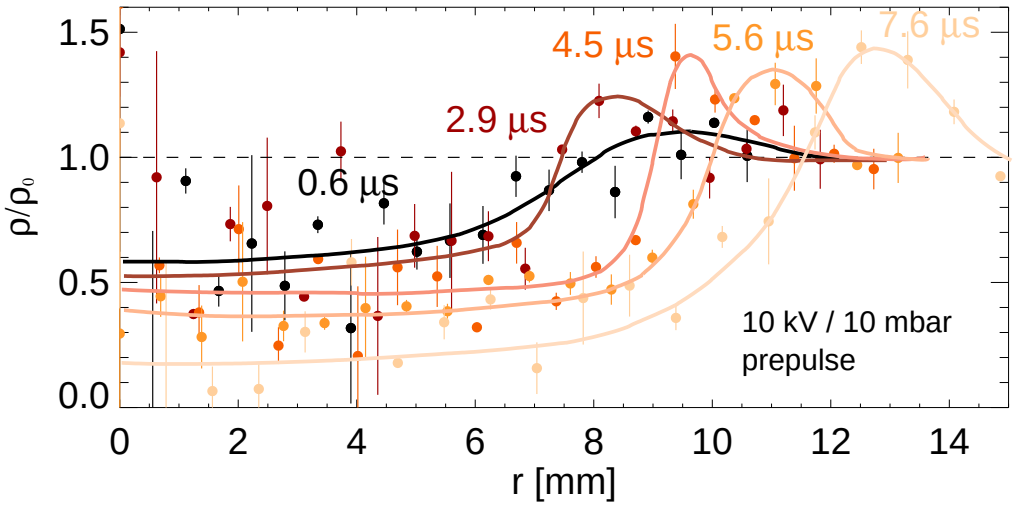

Figure 4.13: Evolution of the gas density in a 10 kV prepulse discharge in 10 mbar ammonia.

in both framing and interferometric images of the channel (compare chapter 3.1.4). High current discharges at GSI with a preceding low energy discharge are most stable when the delay between prepulse and main discharge are in the order of 10 μs. This time is big enough to decrease the gas density on the channel axis but short enough for the shock to remain in the vicinity of the discharge. At longer delays above 15 μs the missing gas wall leads to a higher instability growth rate. In the experiments, channels with such delays were only stable up to 3 μs after the breakdown. The Berkeley experiment showed an improved channel stability with the prepulse also with delays of 50 μs between prepulse and main discharge. However, in those experiments the rarefaction channel is not formed by the laser itself but by the low energy prepulse. The discharges were also initiated at lower pressures and typically with lower prepulse voltages.

Observation of the rarefaction channel created by the laser-gas heating

At a wavelength of 532 nm the formation of a low density channel can also be observed after the laser is fired. Figure 4.14 shows the fringe shift caused by a neutral density change at different times after the laser pulse. At a time of 25 μs after the laser, where the on-axis density has

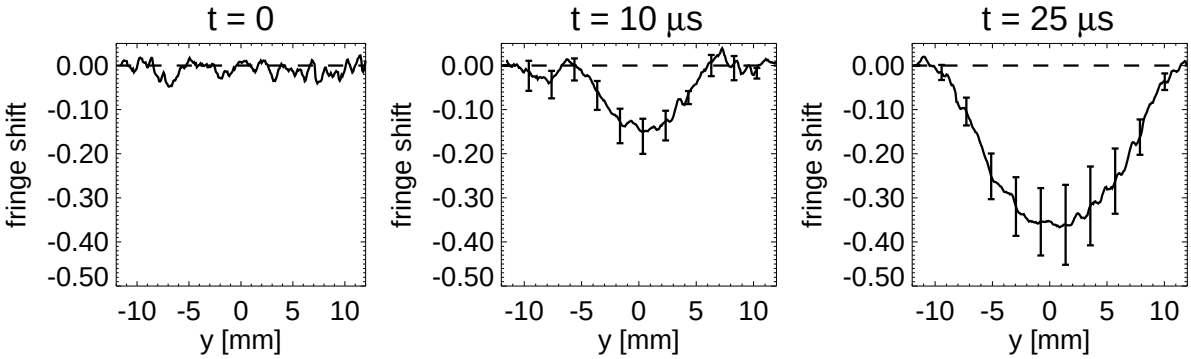

Figure 4.14: Fringe shift caused by the rarefaction channel at different times after the laser pulse.

just reached its minimum value (chapter 3.1) a fringe shift of more than 0.35 fringes was clearly observed. For the measurement a 1 J/cm^2 laser pulse tuned around the peak absorption was fired into a 15 mbar ammonia gas fill. The error bars were calculated as the standard deviation of the fringe shift of five independent shots for each time. Since the expected fringe shift was very small, the mirrors were adjusted to screen only 5 fringes in the field of view. Since the refractive index depends only weakly on the wavelength, the fringe shift at 1064 nm is only half as big as at 532 nm (equation 4.5). The radial density profiles calculated by an Abel inversion as described above are plotted in figure 4.15 (a) for different times. At 10 μs after the laser,

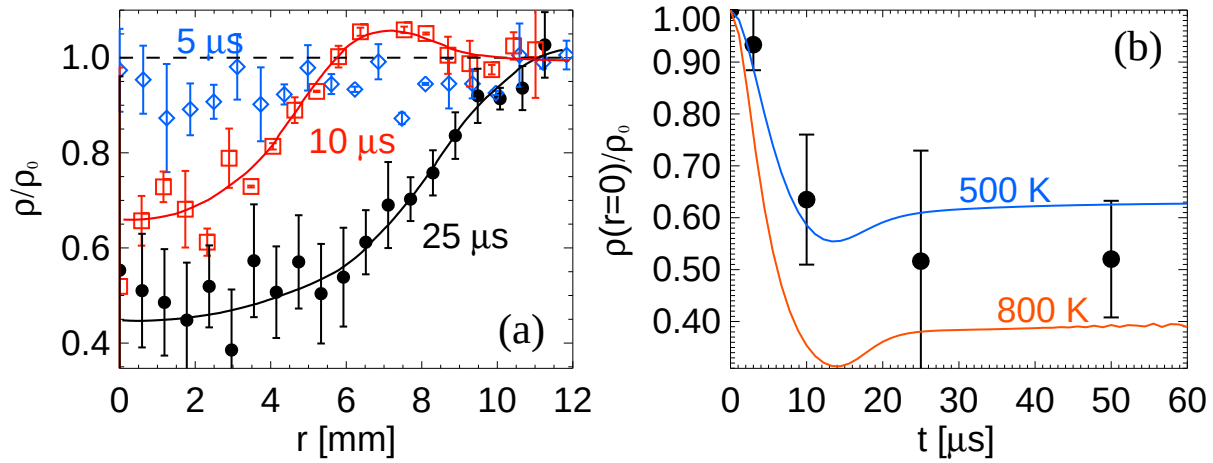

Figure 4.15: Abel inverted gas density profile for different times (a) and the time evolution of the gas density on axis (b).

the gas density on axis has dropped by 30 percent. A weak pressure wave can clearly be seen at r = 7 mm. After 25 μs the central density reaches half the value of the initial density. At this time the pressure wave has reached the edge of the field of view. Since no undisturbed region remains as a reference the absolute fringe shift could be smaller by the amplitude of this

pressure wall. The time evolution of the on-axis gas density is shown in figure 4.15 (b). For comparison the results from a CYCLOPS calculation (figure 3.7) are plotted for an initial gas temperature of 500 K and 800 K. The measurement indicates in accordance with the simulation a decrease of density during the first 10 to 20 μs. After this time the density remains at a low value for milliseconds. At 2 ms after the laser, the on-axis density is still reduced by 40 percent. After 2 s the rarefaction channel has disappeared. Although due to the small fringe shift and the large errors a precise gas density measurement is not possible, the formation of the rarefaction channel can clearly be observed. The size of the channel, the density reduction, as well as the temporal evolution point towards the results obtained by CYCLOPS and agree also with the measurements of the breakdown voltage and the discharge delay. In an alternate determination of the gas density, measurements of the scattering of a heavy ion beam from the UNILAC accelerator in the ammonia gas showed similar results [Nef02].

4.1.2 Shadowgraphy

A refractive index gradient bends a traversing light ray towards the direction of higher index of refraction. This effect is caused by a wavefront distortion due to different propagation velocities in regions of different refractive index [Jah71]. If lenses in the optical system do not compensate such refractive effects, light rays from the laser probing the plasma may be displaced in the image plane of the camera, simulating a different origin. In the setup of the interferometer described above, the camera was focused onto the target. However, the laser probes the plasma twice and either the image of the channel or the mirror image must be out of focus and therefore deflections of the rays are not completely compensated.

The same system can be used as a shadowgraphy-diagnostics for gradients simply blocking the reference beam. Deflected rays from the gradient of the gas shock or steep electron density gradients will create a dark region on the camera from where the rays have been deflected and a brighter region where they end up (figure 4.16). A series of shadowgraphic images of a high

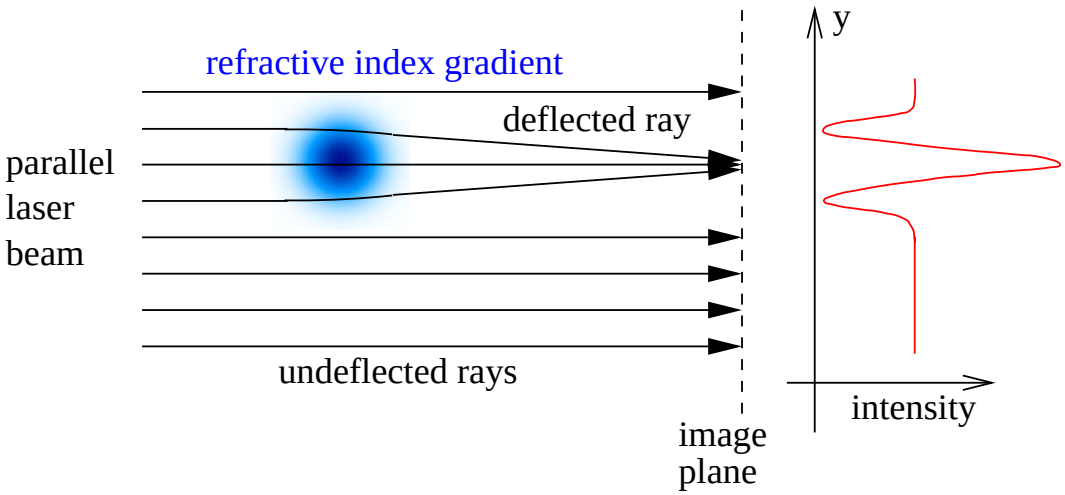

Figure 4.16: Working principle of shadowgraphic imaging. Rays which are deflected due to density gradients create brighter regions at the position where they meet the image plane. The intensity at their original position is decreased.

current discharge in 15 mbar ammonia is shown in figure 4.17. Already 1 μs after the breakdown, a weak gas shock is visible on either side of the channel. Dark and bright stripes appear also directly on the channel axis and remain visible for another microsecond. This observation is due to extremely steep electron density gradients which occur in the early phase of high current discharges without prepulse at pressures above 10 mbar. This steep density profile was already

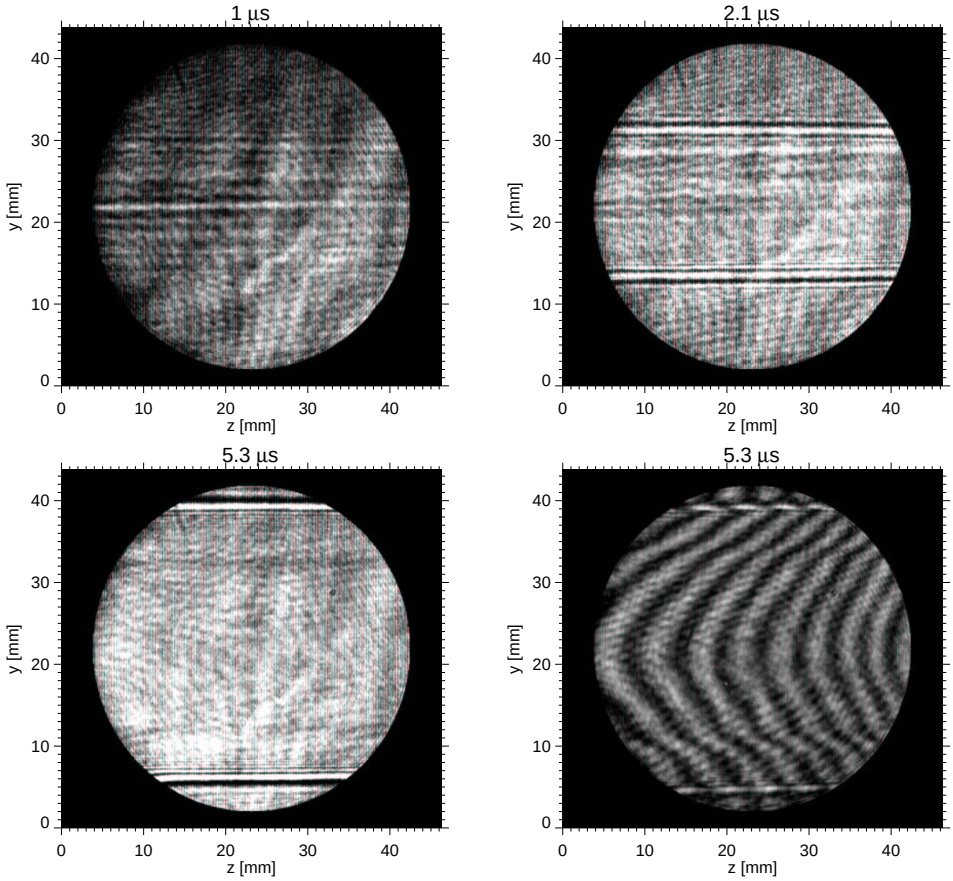

Figure 4.17: A series of shadowgraphic images of a high current discharge in 15 mbar. The last picture was recorded with an unblocked reference beam. The shadowgraphic effect is also visible in the interferogram.

seen in the interferometric measurements (compare curves for 10 mbar and 15 mbar at around 1.5 μs in figure 4.6). As the electron density profile flattens at later times the structure inside the plasma channel disappears while only the expanding gas shock remains. The increasing contrast between the bright and the dark stripes confirms an increasing gas density gradient in the shock as was also shown in figure 4.11. Together with the contrast the size of the dark stripe increases with time which is due to both a broadening of the gradient region and the increase of deflection angle. At high pressures above 15 mbar the deflection is so large, that the interferometric fringe pattern is interrupted at the position of maximum gas density gradient. At lower pressures the deflection was too small to interrupt the fringes. A quantitative density gradient measurement by shadowgraphy is difficult. The shadowgraphic images were mostly used to measure the position and expansion velocity of the gas shock. Figure 4.18 shows the radial position of the shock as well as the velocity for different discharge parameters. The expansion of the shock can be fitted well with $r_{\mathrm{shock}} \sim t^{2/3}$. At times before 1.5 to 2 μs the shock density is still too small to measure the position. At later times the shock expands radially with a velocity between 1.5 and 2 $mm/\mu s$ for 45 kA discharges in 20 mbar ammonia. For lower gas pressure the expansion velocity is higher, reaching up to 3 $mm/\mu s$. Only a small difference in both radial position and velocity of the shock is found for 20 kA and 45 kA discharges in 15 mbar (figure 4.18 (b)). Although less energy is deposited into the gas in the first case, the current maximum is reached at an earlier time, which might explain the small difference. A prepulse charged to 15 kV causes a weak shock with an expansion velocity of only 1 $mm/\mu s$.

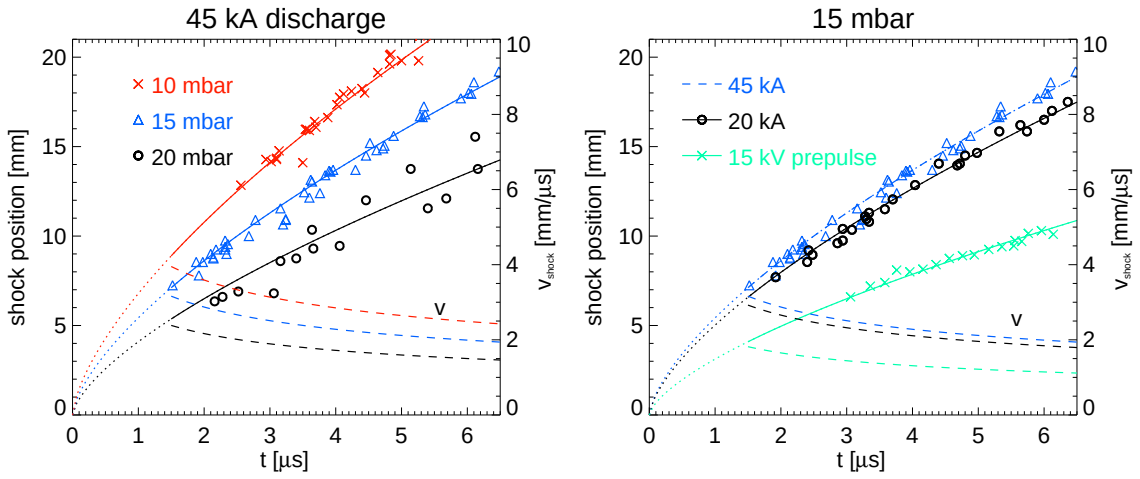

Figure 4.18: (a) Radial shock position and velocity (dotted lines) for a 45 kA discharge in 10 mbar, 15 mbar and 20 mbar ammonia. (b) Comparison of the shock expansion for a 45 kA, 20 kA discharge and a 15 kA prepulse in 15 mbar.

4.1.3 Schlieren imaging

As already mentioned above, the neutral gas wall which surrounds the discharge plays an important role for the stability of the plasma channel. A better diagnostics than shadowgraphy is the schlieren imaging which is also used to detect refractive-index gradients but is more sensitive. A schlieren diagnostics was used both at Berkeley and GSI, mainly for shock velocity measurements in the prepulse discharge where the fringe shift recorded by the interferometer is too small to accurately determine the shock position. The setup as used at GSI is shown in figure 4.19. The arrangement is very similar to the interferometer but a 5 mW cw HeNe laser at 633 nm

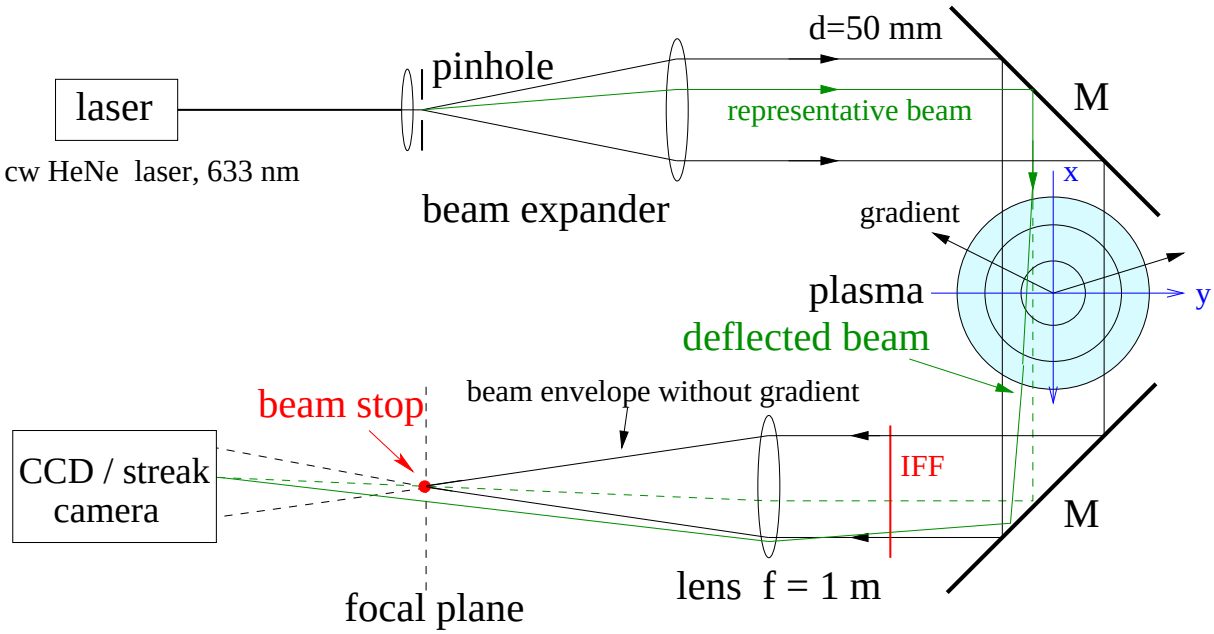

Figure 4.19: Setup of the schlieren diagnostics.

was used instead of the pulsed laser. This allows the use of a streak camera which is much better suited to measure the time evolution of the shock. The expanded laser beam probes the plasma only once from a side and is then focused by a f = 1 m lens, the 'schlieren-head' onto a beamstop. The beamstop has a size slightly bigger than the laser focal spot, so no light reaches the camera. When a refractive index gradient is present inside the plasma, rays penetrating this region are deflected from their initial path by the angle

$$\alpha = \int_l \frac{1}{\mu}\frac{\partial \mu}{\partial y} dx \ , \tag{4.12}$$

where α is given in rad. The integration has to be performed over the whole line of sight. Only refractive index gradients $\partial\mu/\partial y$ perpendicular to the probing beam contribute to the deflection angle. In cylindrical coordinates $\partial\mu/\partial y$ can simply be calculated by

$$\frac{\partial \mu(x,y)}{\partial y} = \frac{\partial \mu(r)}{\partial r} \cdot \frac{y}{r} \ , \tag{4.13}$$

where $r = \sqrt{x^2 + y^2}$. For small deflection angles, the displacement of those rays in the focal plane of the lens is given by

$$d = \alpha \cdot f \ , \tag{4.14}$$

where α is the deflection angle in rad and f the focal length. If d is bigger than half the size of the beamstop, the rays can pass and are detected on the camera. The camera objective

images the apparent position of the channel onto the CCD chip. In this way, the rays are always recorded at the same position, no matter how much they have been deflected. Intensity changes due to focusing or defocusing effects caused by gradients which form the shadowgraphic images mentioned above are also compensated. However, this is only true for an ideal lens. A knife edge (razer blade) which can only visualize deflections in one direction was used as an unsymmetric beamstop. The knife edge has the advantage that it can be adjusted to the focal spot size of the laser. By orienting the edge both up and down in different shots, one can distinguish between positive and negative gradients. The knife edge must be oriented parallel to the plasma channel, since the deflections are always perpendicular. To see gradients in both directions at the same time, a symmetric beamstop is necessary. The tapered tip of a knife can be used which also allows adjustments to the focal spot size but is not perfectly symmetric. Cylindrical wires of the proper thickness were also used but they cause problems due to reflections. Experiments were also performed with a glas plate with a 300 nm thick gold coating and a 100 μm diameter hole. The hole was created by a 10 mJ Nd:YAG laser pulse of 5 ns duration focused to a small spot by a f = 25 mm lens onto the gold coating. While one shot is already enough, about 5 shots were used to make the hole as round as possible. The schlieren pictures were either recorded by a fast shutter camera with an exposure time of 100 ns (PCO Dicam PRO) or a streak unit (Hamamatsu C2830) with a time resolution of 250 ns, determined by the slit width. An interference filter for 633 nm (10 nm FWHM) placed before the camera blocks most of the discharge light. In high current discharges at very high pressure, the plasma self emission is so strong that the 5 mW laser can not compete even with the interference filter used. A small aperture (few mm) around the focal spot can reduce the plasma self emission considerably without disturbing the laser. However, the aperture must be big enough for the deflected rays to pass.

Schlieren images of the low energy prepulse

A typical schlieren - streak picture of the low energy prepulse is shown in figure 4.20. The prepulse capacitor was charged to 10 kV and fired 15 μs after the laser pulse. The gas pressure was 10 mbar. For the picture 50 streak images from independent discharges were averaged to improve the quality. The low jitter of only a few ns and the good reproducibility of the prepulse discharge simplify this averaging process. Around 2 μs after the breakdown, the shock becomes visible. The temporal evolution is fitted well by $y \sim t^{2/3}$ as it was already the case in the high current discharge measurements mentioned above. One can clearly distinguish two dark regions on either side which are separated by a region of less intensity. This effect is caused by the positive and the negative gradient of the pressure wave, which are both visible since a symmetric beamstop was used. The highest intensity and thus the biggest density gradients are reached at around 6 μs after the breakdown. After this time the intensity drops gradually until the wave becomes invisible after 15 μs. Beginning from 5 μs a second broader region of less intensity can be seen around y = 10 mm on both sides. This schlieren images are caused by the gradient of the rarefaction channel which is broader and thus less steep. The position of this

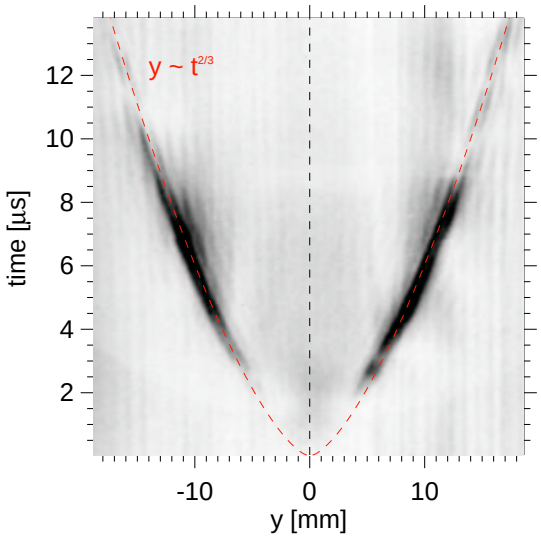

Figure 4.20: Schlieren - streak image of a 10 kV prepulse in 10 mbar ammonia.

gradient does not change from 5 μs until the end of the measurement at 15 μs. Although the shock is clearly visible on a single schlieren-streak picture the effects mentioned become only visible when several pictures are averaged.

The schlieren method is better suited to measure the shock velocity in prepulse discharges since in the very narrow shocks the gradient is big even when the maximum density is small. The expansion of the shock was measured in prepulse discharges with different pressures (a), voltages (b), delays (c) and laser energies (d). The results are summarized in figure 4.21. In all cases the

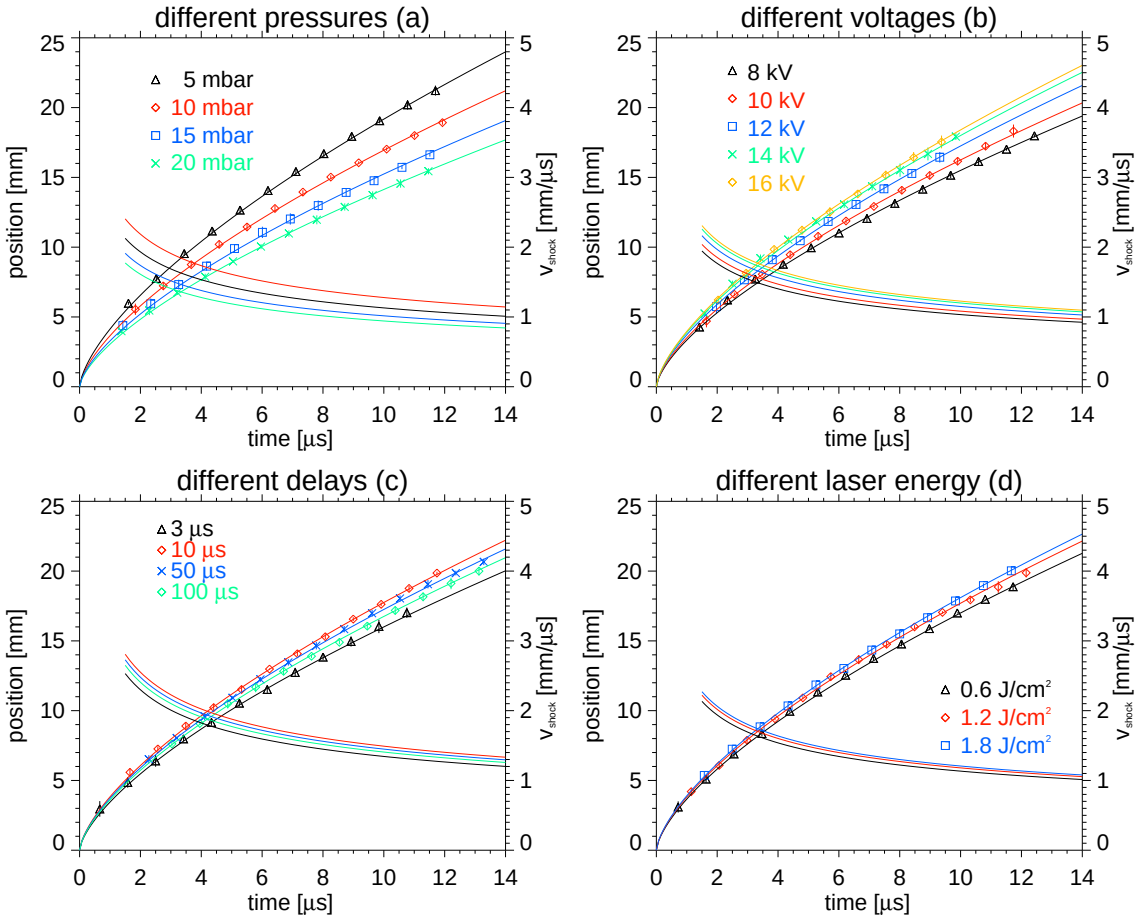

Figure 4.21: Expansion of the shock and shock velocity for different pressures, voltages, laser energies and delays between laser and prepulse.

shock is expanding with a velocity of around 1 $mm/\mu s$. Variations in the velocity are smaller than 20 percent. At high gas pressures, the shock expands slower than at a lower pressure due to the higher mass density of the gas. After 10 μs the shock has moved only to r = 13 mm at a pressure of 20 mbar while it reaches a distance of 19 mm from the axis at a pressure of 5 mbar. The more energy is dumped into the gas by the prepulse the faster the shock expands. The initial gas pressure has the biggest effect on the shock velocity. Figure 4.21 compares the expansion of the shock for prepulse voltages of 8 kV, 10 kV, 12 kV, 14 kV and 16 kV corresponding to an energy of 6.4 J, 10 J, 14.4 J, 19.6 J and 25.6 J. The expansion of the shock can be used indirectly to estimate the evolution of the gas pressure in the laser-rarefaction channel. Figure 4.21 (c) shows the expansion for different delays between laser pulse and prepulse discharge. A laser pulse of 1.6 J/cm^2 was used for the measurements. At a delay of 3 μs the gas pressure inside the rarefaction channel has only droped by a few percent. After 10 μs when the pressure has almost droped to its minimum value the expansion velocity is highest according to figure 4.21 (a). At later times the gas density in the rarefaction channel increases slowly which leads to a

reduced expansion velocity of the shock in the subsequent prepulse. If the delay between laser and prepulse discharge is kept constant at 15 μs, the density in the rarefaction channel is only determined by the laser energy. Higher energy will cause a lower pressure by the time when the prepulse is triggered and consequently a higher expansion velocity of the shock, in agreement with the measurements (figure 4.21 (d)). However, also this effect is only minor.

The data from figure 4.21 can be used in future to benchmark simulation codes and therefore to predict the evolution of the rarefaction channel. Measurements from Berkeley performed with a setup very similar to the one from GSI are compared to the results from a CYCLOPS calculation (figure 4.22) The deflection angle was calculated from the simulated gas density

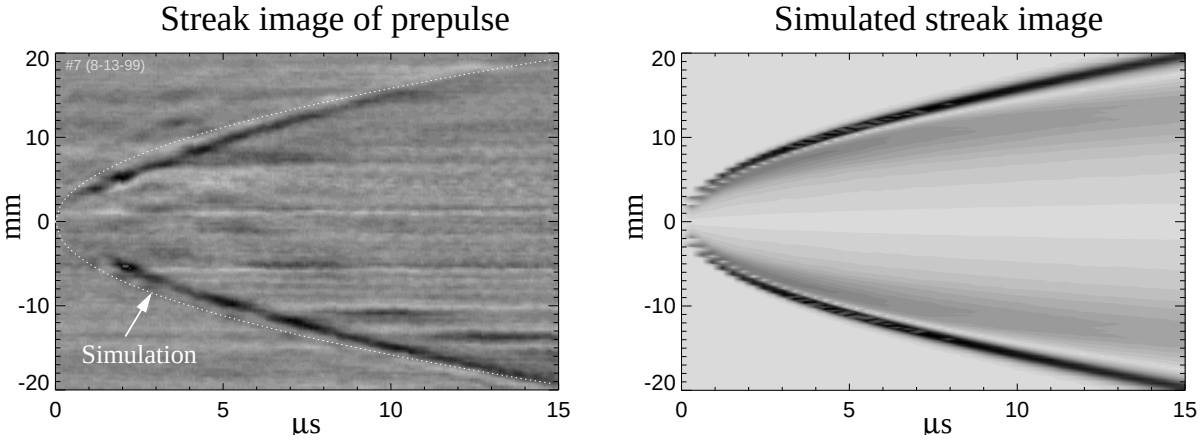

Figure 4.22: Comparison of a measured and a simulated streak image for a 7 kV prepulse in a gas mixture of 5 torr Nitrogen and 2 torr Benzene at Berkeley.

profiles at different times (figure 4.23) by

$$\alpha(y) = 2 \int_0^{x_{max}} \frac{1}{\mu(r)} \frac{\partial \mu(r)}{\partial r} \frac{y}{r} dx \ , \tag{4.15}$$

where $\mu(r)$ was calculated from the Gladston-Dale relation for nitrogen [Wea90]. The intensity

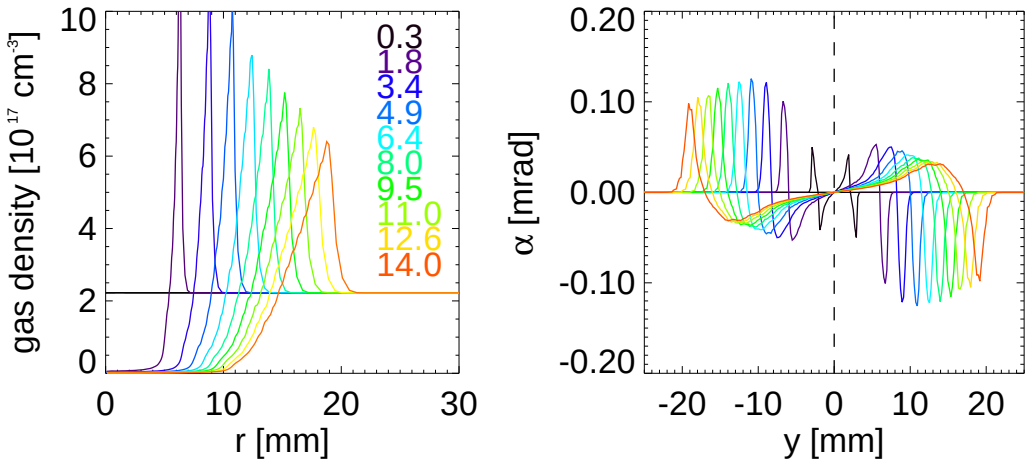

Figure 4.23: The radial gas density profile in a 7 kV prepulse simulated by CYCLOPS (left) as well as the derived deflection angle profile (right).

in the simulated streak picture from figure 4.22 represents here only the absolute value of the

deflection angle. An intensity calibration of the schlieren setup (see below) could in principle be used to reconstruct a more realistic intensity distribution. However, even in this comparison the simulated and the experimental streak pictures look very similar. Both pictures show a strong gradient which represents the steep outer gradient of the shock. The inner gradient is considerably smaller and is invisible in the experimental image. In the simulation the energy of the prepulse was deposited instantaneously at t = 0 while in reality the energy is gradually transfered to the gas during the first μs of the discharge. For this reason, the simulated shock expands in the beginning faster than in the measurement. After a few μs simulation and experiment show the same expansion velocity. The initial size of the conductivity profile was a free parameter in the simulation, which was adjusted within reasonable limits to obtain the same shock velocity.

High current discharge measurements

Also in high current discharges without preceding prepulse a gas shock is formed which can be recorded with the schlieren imaging technique. The shock becomes visible around 1 μs after

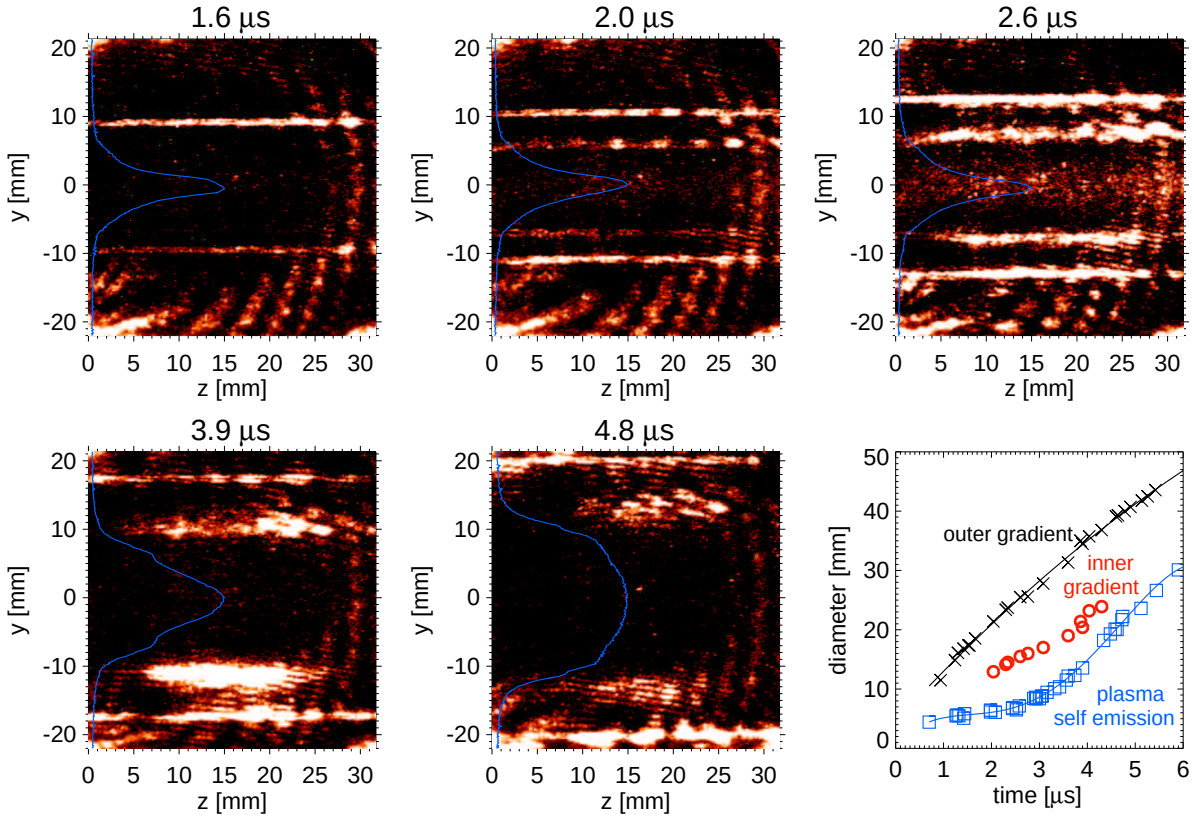

Figure 4.24: Schlieren images caused by neutral gas density gradients in a 20 kA discharge in 10 mbar ammonia. The intensity profile of the plasma self emission is shown in blue. The last graph shows the position of the outer gradient, the inner gradient as well as the diameter (fwhm) of the self emission profile.

the breakdown. However, at this time it is still so weak, that only the steeper outer gradient of the shock can be seen. After 2 μs, also the inner gradient of the shock becomes visible. The profile of the plasma-self emission ditribution is shown in blue. The temporal evolution of the outer gradient, the inner gradient as well as the diameter (FWHM) of the plasma-self emission distribution are sketched in figure 4.24. During the first μs of the discharge, the gas wall is well separated from the inner region of plasma self emission. After 3 μs the diame-

ter of the light-emission distribution grows faster than the shock expands and the plamsa fills the entire space between the shock. At this time when the shock forms the actual edge of the plasma channel, the additional mass density surrounding the current carrying region has the biggest contribution to the stability of the discharge. The outer gradient expands with a velocity ranging from around 4 $mm/\mu s$ in the beginning down to 3 $mm/\mu s$ after 6 μs. The inner gradient only expands with a velocity of 2 $mm/\mu s$ which leads to a broadening of the shock.

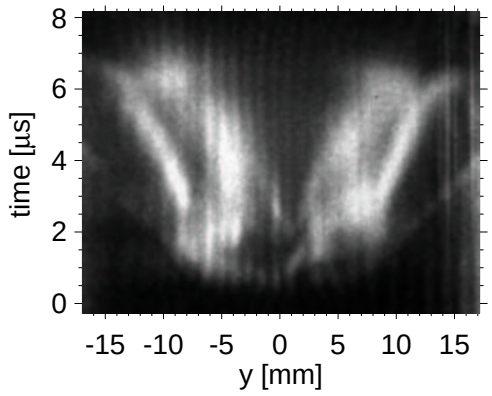

Figure 4.25: Schlieren-streak image of a 45 kA discharge in 10 mbar triggered 10 μs after a 10 kV prepulse. The schlieren are in this case caused by electron density gradients.

The size of the gas shock (distance between inner and outer gradient) increases from around 4 mm at 2 μs to 8 mm at a time of 4.8 μs. While the size of the inner gradient increases from around 1 mm at the beginning to about 5 mm at 5 μs the outer, steeper gradient always has a size of roughly 1 mm. As early as 1.6 μs after the breakdown the expanding shock becomes visible. A streak schlieren picture of a 45 kA discharge in 10 mbar with a preceding 10 kV prepulse, triggered 10 μs before the main discharge is shown in figure 4.25. In this case the schlieren are caused by electron density gradients which are much broader than the gas shock gradients. A gas shock can also be seen in the picture, reaching the edge at around 4 μs but it is much weaker than the schlieren structure inside the channel. A simple estimation of the refractive index gradients in the electron density profiles from figure 4.6 give deflection angles in the order of 0.1 mrad, which is comparable to the gradients caused by the gas shock in prepulse discharges. High current discharges without the prepulse show a schlieren image very similar to the one from figure 4.25. The double structure of each wing in figure 4.25 could be explained by the observed shoulder in the electron density profiles (see figure 4.6). The dark region would then indicate the position of the shoulder, where the gradient vanishes.

Estimation of the refractive index gradient

Quantitative gradient measurements are very difficult with the schlieren technique. However, an estimation of the deflection angle is possible with an intensity calibration of the schlieren system. For this calibration the beamstop (knife edge) was displaced from its initial position by a few μm and the laser intensity distribution on the camera was measured without any refractive index gradient pressent. The intensity as a function of displacement is plotted in figure 4.26. At the initial position, the knife edge is located exactly in the middle of the laser focal spot and blocks half of the total intensity. As the knife edge is moved away from the laser spot, more light can pass the beam stop and the intensity increases until it reaches the maximum value when the knife edge is entirely outside of the laser spot region. In the same way the intensity decreases as the beam stop moves closer to the laser focus until the entire beam is blocked and a minimum intensity is reached. The diameter of the laser focal spot can be estimated from the size of the region where the intensity changes from the maximum to the minimum, which is in this case 200 μm. The maximum deflection angle can now be estimated from a series of discharges at different beam stop positions. A 45 kA discharge in 5 mbar ammonia shows intensity variations due to deflections up to a beam stop position of 0.15 mm. At bigger displacements the schlieren image stays dark. At a pressure of 10 mbar intensity changes can still be recorded at a beam stop position of 0.24 mm. According to equation 4.14 and a focal lengths of the schlieren head

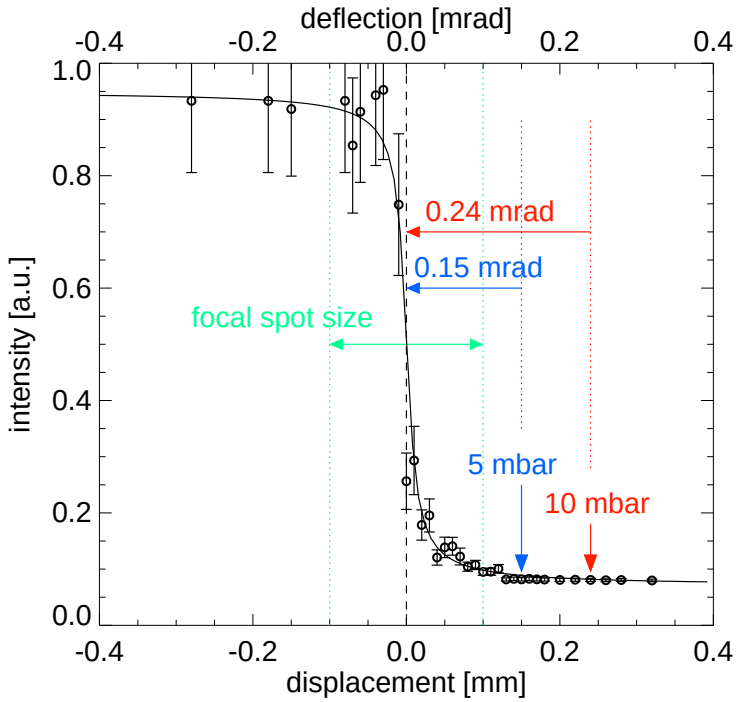

Figure 4.26: Intensity calibration of the schlieren setup. Without any density gradients present, the beamstop was moved by a certain displacement and the intensity was measured on the camera. A laser focal spot size of 200 μm can be estimated from the size of the region with intermideate intensity.

of f = 1000 mm the maximum deflection in those discharges corresponds to 0.15 mrad and 0.24 mrad for the 5 mbar and the 10 mbar discharge respectively. A 15 kV prepulse discharge in 10 mbar still shows schlieren at a beam-stop position of 0.5 mm corresponding to a maximum deflection of 0.5 mrad. This value is just a little above the deflection in a prepulse at Berkeley calculated by CYCLOPS (figure 4.23). The electron density gradients in high current discharges are smaller than the gas density gradients in the prepulse which explains this observation.

Also the direction of the gradient can be determined from the schlieren measurements. In an arrangement of the knife edge which can only detect deflections in the negative y direction, measurements of 20 kA discharges show only the inner gradient of the gas shock at the negative y position (right picture in figure 4.27). Is the knife edge oriented in the opposite way, only the inner gradient at the positive y position is visible. Since a light ray is deflected towards higher refractive index, this observation confirms the assumption, that the light results from the inner gradient of the shock. With a symmetric beam stop both, the positive and the negative gradient of the gas shock are visible on both sides of the channel. Also the direction of the electron density gradients in figure 4.25 can be explained in this way. If an unsymmetric beamstop is used only one of the two wings in figure 4.25 remains visible. The gradient at the positivive y position is only visible if the blade is arranged that only deflections in the positive y direction can pass. An increasing electron density towards the channel axis causes a decreasing refractive index gradient and thus deflects rays at a positive y position towards the positive y direction. The opposite is true for the gradient at the negative y position.

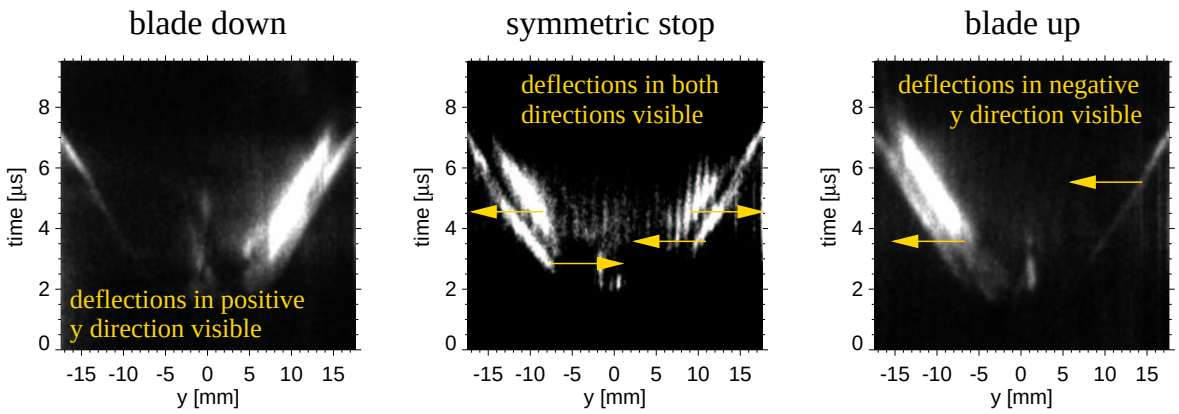

Figure 4.27: Comparison of schlieren streak images of a 20 kA discharge in 15 mbar with a symmetric beamstop (middle) and unsymmetric beamstops oriented with the blade down (left) and up (right).

4.1.4 Development of a Faraday polarimeter for magnetic field measurements

The current-density distribution inside a plasma channel is of great interest since it determines the transport properties. Different diagnostic techniques can be used to measure magnetic fields inside plasmas. Among those are simple coils inserted into the plasma [Pen02], measurement of Zeeman splitting by spectroscopy [Dav97], laser induced fluorescence (LIF) [Noo97] and the Faraday polarization technique [Loc68]. Magnetic probes not only perturb the discharge but are frequently destroyed by the plasma. Spectroscopic techniques and LIF require very high experimental precision and often expensive equipment like tunable dye-lasers or multiple spectrometers.

Measurements of the Faraday rotation of the polarization plane of a laser beam passing through the plasma provide an alternative means for the determination of the magnetic field distribution without disturbing the plasma. The rotation φ of an electromagnetic wave propagating parallel to a magnetic field B in a plasma is given by [Jah71]:

$$\varphi[rad] = 2.62 \cdot 10^{-19} \lambda^2[\mu m] \int n_e[cm^{-3}] B[T] dl[m] \tag{4.16}$$

where λ is the wavelength of the probing beam and n_e the electron density. The integration has to be performed over the whole line of sight of the laser beam. To obtain information about the magnetic field, a simultaneous interferometric measurement of $\int n_e dl$ is necessary for a deconvolution of the rotation data.

Design considerations

The rotation angle increases with the square of the wavelength λ. Therefore a laser in the infrared region is advantageous to obtain larger rotation angles. In the experiment described here, the maximum rotation for a discharge current of 40 kA, a plasma density of $10^{17}\ cm^{-3}$ and a wavelength of 10.6 μm (CO_2 laser) is only about one degree. The 'side-on' measurement of the z-pinch plasma and consequently the integration over many different radial positions in the plasma leads only to a very small difference in rotation for very different current density distributions: Figure 4.28 shows the expected rotation angle profile for a homogeneous distribution (black) and the case where the current flows only at the edge of the channel (red). The rotation angles differ only by a few tens of degrees (blue curve) for those two extremely different cases. To distinguish

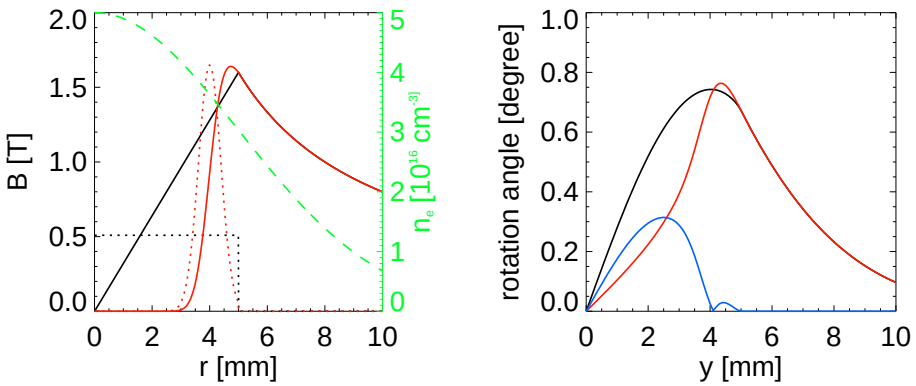

Figure 4.28: Expected Faraday rotation angles for two different current density distributions (red and black) as a function of distance y of the probing laser beam from the discharge center. The assumed electron density (green), the magnetic fields (solid line) and the current density distributions (dotted lines) are ploted as a function of radius r. The blue curve shows the difference in rotation angle for the two cases.

between different magnetic field distributions a sensitivity of around 0.01^o is required in this case. In the visible range the sensitivity has to be better by a factor of hundred.

Rotation angles as small as 0.01^o have already been measured in previous experiments [Gri68, Fal68] using a HeNe laser at 632.8 nm, while higher wavelengths were used for plasmas with smaller magnetic fields mainly the poloidal fields in tokamaks [Sol86, Ric92, Kun78, Job92, Ma79, Hut81]. Rotation angles are measured by analyzing polarizers, which are oriented under some angle to the initial polarization of the probing beam. Different angles are converted into different intensities which are easily detected by conventional means. If the rotation angles are big enough at a wavelength in the visible range simple PIN photodiodes can be used which outreach the performance of similar detectors for the infrared region by orders of magnitude [Mar94]. Better detectors and optics make it much easier to measure small angles in the visible range. Going to higher wavelengths on the other hand increases the rotation angles with λ^2. The deflection of the laser beam due to electron density gradients (chapter 4.1.3) also scales with λ^2 and can become a problem for the rotation measurement at high wavelengths. An upper limit is finally set by the cut-off frequency of the plasma (equation 4.3). As a compromise, a CO_2 laser with an intermediate wavelength of 10.6 μm together with fast Mercury-Cadmium Telluride (HgCdTe) detectors for the analyzer was chosen for the Faraday polarimeter at the Berkeley channel experiment. A CO_2 laser has been used before to measure the Faraday rotation in a theta pinch plasma [Jar77].

The half-shadow principle

The sensitivity of the setup can be strongly increased, using a detection scheme with two analyzers, operating on the so called "half-shadow principle"[Loc68, Fal68]. In this configuration the linearly polarized laser beam after probing the plasma is split into two beams of equal intensity by a polarization insensitive beam splitter (PIBS) (figure 4.29). The two analyzing polarizers

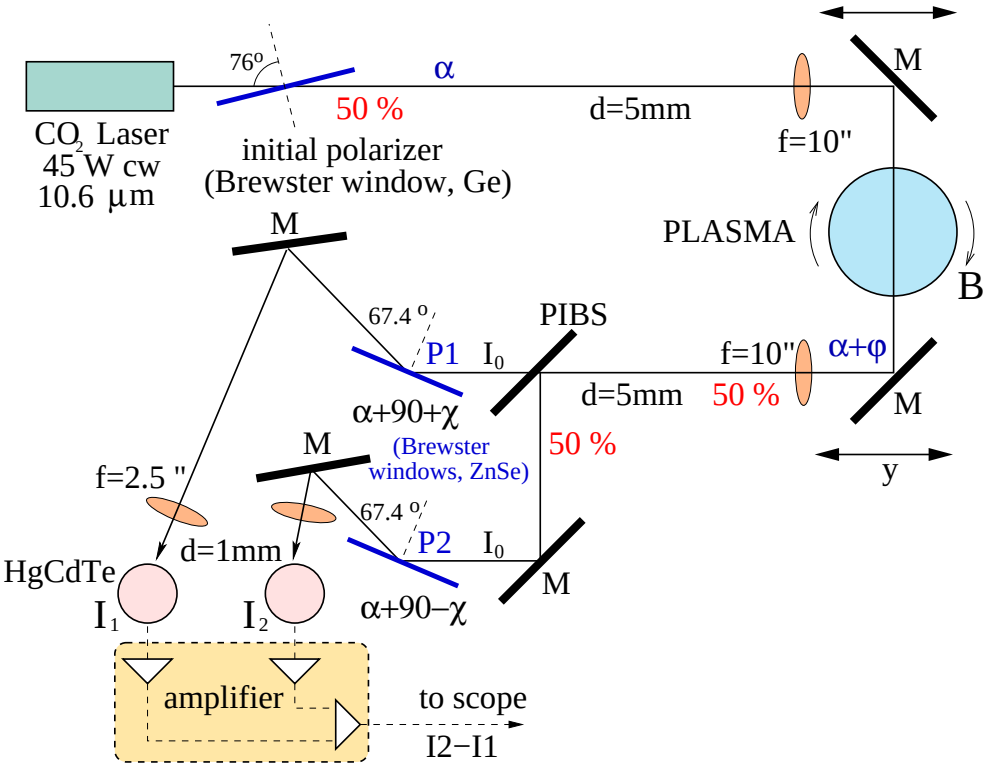

Figure 4.29: Setup of the half-shadow Faraday polarimeter using a cw CO_2 laser and HgCdTe detectors.

P1 and P2 are oriented $90^o - \chi$ and $90^o + \chi$ relative to the initial polarization α (figure 4.30). Therefore the intensities on the two detectors are

$$I_1 = I_0 \cdot sin^2(\chi - \varphi) \tag{4.17}$$

$$I_2 = I_0 \cdot sin^2(\chi + \varphi) \tag{4.18}$$

where φ is the Faraday-rotation angle, I_0 the laser intensity before the polarizers and χ is called the half-shadow angle. The difference signal $\Delta I = I_2 - I_1 = I_0 \cdot sin(2\chi)sin(2\varphi)$ changes its sign

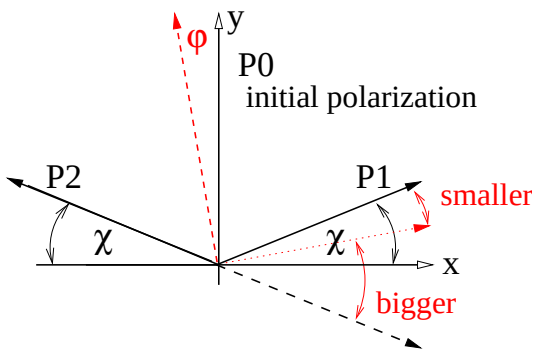

Figure 4.30: Orientation of the polarizers P1 and P2 relative to the initial polarization of the laser beam P0 using the half-shadow principle.

when the direction of the magnetic field is reversed. By measuring also the sum of both signals one gets an expression which is independent of the initial laser power I_0:

$$\frac{I_2 - I_1}{I_2 + I_1} = \frac{sin(2\chi)sin(2\varphi)}{2 \cdot sin^2\chi} \tag{4.19}$$

The half-shadow angle χ determines the sensitivity of the setup. The contrast dI/I_1 is given by

$$\frac{dI}{I_1} = 2\frac{sin(2\chi)cos(2\varphi)}{sin^2(\chi - \varphi)}d\varphi \tag{4.20}$$

where $dI/d\varphi$ is given by

$$\frac{dI}{d\varphi} = \frac{d}{d\varphi}I_0 sin(2\chi)sin(2\varphi) = 2I_0 sin(2\chi)cos(2\varphi). \tag{4.21}$$

For very small φ we obtain

$$\frac{dI}{I_1} \approx 4 \cdot ctg(\chi)d\varphi \tag{4.22}$$

The sensitivity increases as the half-shadow angle is reduced. This can also be seen in figure 4.31: The signal dI has its maximum for $\chi = 45^o$. However the background I_1, I_2 decreases for smaller χ. Having enough laser power available the contrast can thus be increased by choosing a smaller half-shadow angle. A polarizer with high extinction ratio ϵ increases the background $I_1 = I_0 \cdot (sin^2(\chi - \varphi) + \epsilon)$ independent of χ. Therefore the contrast has a maximum value and decreases for bigger or smaller χ. If the initial power is less than half the value needed to saturate the detector the best half-shadow angle is 45^o. For higher laser power the half-shadow angle must be reduced in order to prevent saturation. The background signals on the detectors stay then constant while the contrast increases (figure 4.31 b). In the case from figure 4.31 using a poor quality polarizer with an extinction ratio of 0.1 the maximum laser power that could be used is 5 W. For higher powers even a half-shadow angle of 0^o would lead to a saturation of the detector. A good extinction ratio is only for small χ of importance. With an initial

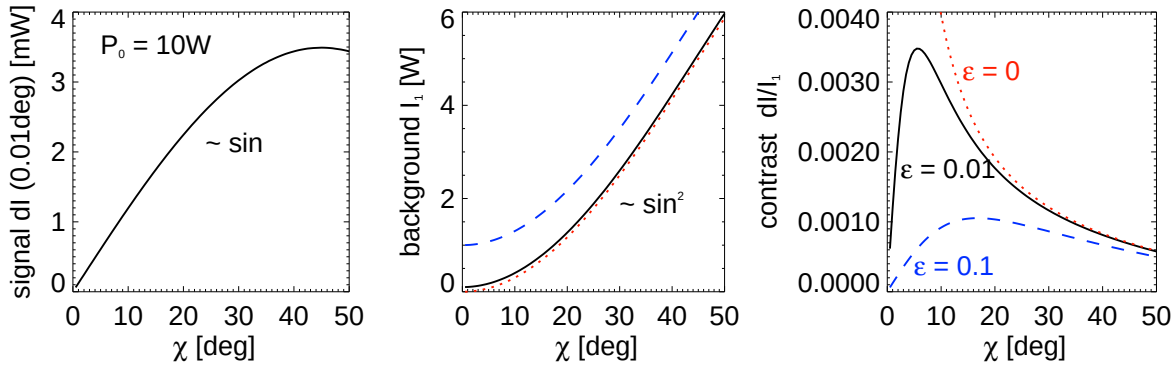

(a) Signal, background and contrast as a function χ for a laser power of 10 W.

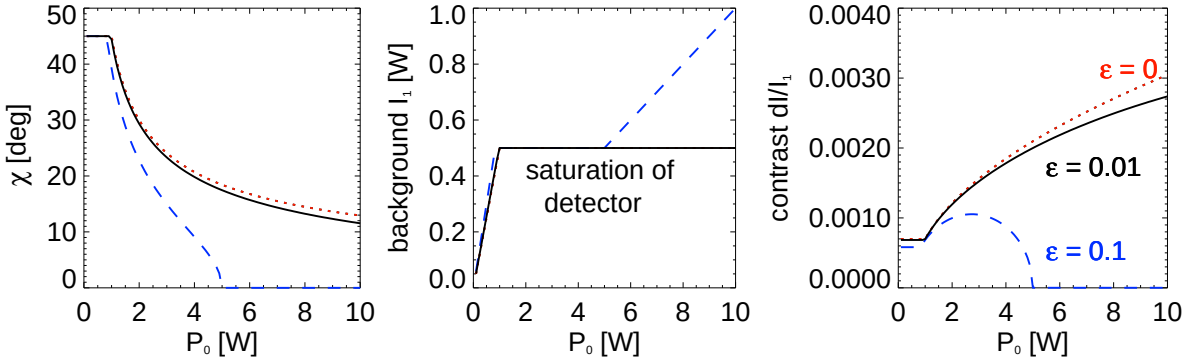

(b) Half-shadow angle, background and contrast for a rotation signal of 0.01^o as a function of laser power.

Figure 4.31: Signal dI for a rotation of 0.01^o, background I_1 and the contrast $= dI/I_1$ as a function of half-shadow angle χ (a) and the initial laser power P_0 (b) for three different extinction ratios ϵ of the polarizers.

power $I_0 = 10\ W$, a half-shadow angle $\chi = 10^o$ and an extinction ratio of the coated Brewster polarizers $\epsilon = 0.01$, the contrast for a rotation signal of 0.01^o is better than $3 \cdot 10^{-3}$. This is an order of magnitude higher than for a detection scheme with only one analyzing polarizer.

In reality the two half-shadow angles can never be adjusted in exactly the same way. Also the signals on the two detectors for the same half-shadow angle and absent Faraday rotation will not be exactly the same due to small differences in the sensitivity of the detectors or small differences in the optical components used. Equations 4.17 and 4.18 must then be expressed as

$$I_1 = I_0 \cdot sin^2(\chi - \varphi) \tag{4.23}$$

$$I_2 = I_0 \cdot e_0 \cdot sin^2(\chi \cdot e_1 + \varphi) \tag{4.24}$$

where e_0 and e_1 are two dimensionless factors describing the strength of the two effects described above. The difference signal ΔI then becomes

$$\Delta I = I_2 - I_1 = \frac{I_0}{2}\left[2\varphi \underbrace{(sin(2\chi) + e_0 sin(2\chi e_1))}_{\text{const}} + cos(2\chi) - e_0 \cdot cos(2\chi e_1) + e_0 - 1\right] \tag{4.25}$$

$$\Delta I = const \cdot I_0 \cdot \varphi + \text{offset} \tag{4.26}$$

The offset can therefore be eliminated by adjusting one of the half-shadow angles (e_1) to get a zero difference signal for zero Faraday rotation as required. The sum becomes

$$I_1 + I_2 = \frac{I_0}{2}\left[2\varphi \underbrace{(sin(2\chi) - e_0 \cdot sin(2\chi e_1))}_{\ll 1} + \underbrace{1 + e_0 - cos(2\chi) - e_0 \cdot cos(2\chi e_1)}_{\text{const}}\right] \tag{4.27}$$

$$I_1 + I_2 \approx I_0 \cdot \text{const} \tag{4.28}$$

The dependence of the sum signal on φ for nonzero e_0 and e_1 is negligible. For $e_0 = 0.8$, $e_1 = 1.12$ and $\chi = 10^o$ the sum changes by less than a factor of 10^{-3} for $\Delta\varphi = 1^o$. Small differences in the optical components or the sensitivity of the two detectors are acceptable if the offset in the difference signal without a magnetic field present can be removed by adjusting one of the half-shadow angles in a proper way.

The HgCdTe detectors

The signals are detected by two fast ambient temperature Mercury Cadmium Telluride (HgCdTe) detectors [Gal84], which can be thermo electrically (TE) colled and do not require liquid nitrogen. They combine the capability to measure small signals (noise equivalent power (NEP) $< 10^{-4}$ W) with a high saturation threshold ($> 0.1\ W$) and therefore have a contrast better than 10^{-3} as required (table 4.1).

Sensitive wavelength range	$2 - 12\ \mu m$
Operation temperature	278 K (5^o C), TE cooled, no liquid nitrogen
Response time	< 0.2 ns
Detectivity D^* (10.6 μm)	$> \ 3 \cdot 10^6 cm\sqrt{Hz}/W$
Active area	4 mm x 4 mm
Noise equivalent power (NEP)	$\sqrt{16mm^2 \cdot B}/D^*$
	$= 8 \cdot 10^{-5} W$ for $B = 350\ kHz$ ($\tau_r \approx 1\ \mu s$)
Saturation	> 0.5 W
Response	22 mV/W

Table 4.1: Properties of the HgCdTe infrared detectors from VIGO-Systems Ltd. [Gal84, Per96].

The difference amplifier

The voltage signal from the detector for a rotation angle of 0.01^o , $I_0 = 10\ W$, $\epsilon = 0.01$ and $\chi = 10^o$ is only around $1\ mW \cdot 22\ mV/W = 22\ \mu V$. The biggest rotation signal to be expected is around 1^o (figure 4.28) corresponding to a voltage output of 2 mV. The background signal which is adjusted by the laser power to be just below saturation is finally around $0.5\ W \cdot 22\ mV/W = 11\ mV$. A fast amplifier with a high gain is used to resolve the μA signals. The amplifier also computes the difference signal to remove the large background which is the same on both detectors and always superimposed on the actual rotation signal. The two outputs from the detectors V_1 and V_2 are first amplified in preamps to give an output of around 3 V for the background signal. The background signals are then subtracted in the difference amplifier. After this large common mode signal is removed, the remaining signal is further amplified to get an output close to the maximum output voltage of the amplifier (15 V) for the maximum rotation angle. The signal for a rotation of 0.01^o should then be comparable or bigger than the electric noise. Since we use a cw laser, the bandwidth is only limited by the performance of the amplifier. The amplifier (figure 4.32) is built up from two simple low-cost operational

amplifiers (OPA 37, Burr-Brown [Bur98]) as preamps with a gain of around 260 and a bandwidth of $B = 63\ MHz/260 = 240\ kHz$. The risetime or "time constant" of the amplifier, which is the time it takes for the output to reach a value of $(1 - 1/e) \approx 63\%$ of the final output [Per96], is given by $\tau_r = 1/(2\pi B) \approx 0.7\ \mu s$. The difference signal is computed by an instrumentation

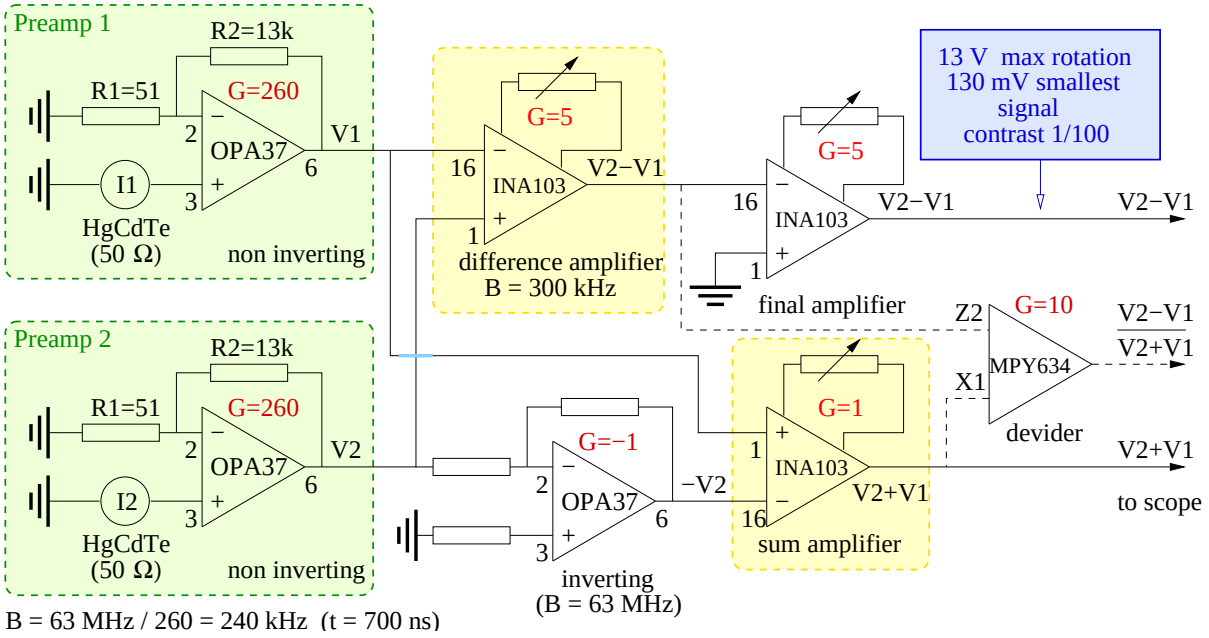

Figure 4.32: Circuit of the difference amplifier.

amplifier (INA 103, Burr-Brown) with a gain of around 5 and a bandwidth of 300 kHz. After a final amplification with another gain of 5 the overall gain of the amplifier is around 6500. With this parameters the signal for the maximum rotation of 1^o will be around 13 V and the signal for a rotation of 0.01^o around 130 mV which is then recorded on an oscilloscope. A second difference amplifier calculates the sum of both signals, after one of the two input signals V_2 has been inverted. Another instrumentation amplifier (MPY 634) finally computes the rotation signal $(V_2 - V_1)/(V_2 + V_1)$. The amplifier is carefully shielded and operated by batteries to reduce the electromagnetic noise induced by the high current discharge to a minimum.

Performance tests of the laser-detector-amplifier system

Performance of the amplifier The performance of the amplifier was tested offline with a voltage divider resistor chain, delivering a background signal of 11 mV to both inputs V_1, V_2 and a sinusoidal modulation from a function generator with an amplitude of 300 μV and a rise time of 4 μs at only one (V_1) of the two inputs. This signal simulates a Faraday rotation of around 0.2^o. The amplifier response and the input signals are shown in figure 4.33. For this test the total gain of the amplifier was adjusted to a six times higher value (36400) than initially designed to compensate for a lower laser power available for the first Faraday rotation measurements (see next section). This test was performed during a high current discharge with the amplifier box near the Faraday cage of the discharge chamber. The total noise as measured on the scope is $\pm 200\ mV$ and combines thermal noise of the detectors and amplifier, as well as electromagnetic noise induced by the high current discharge. The noise is only half as big as the expected signal for a Faraday rotation of 0.01^o (i.e. 500 mV at this gain for a laser power of $I_0 = 10\ W$). The output signal (blue curve) lags behind the input signal (black curve) by around 1.5 μs. Going back to the design gain (6500) will decrease this time response by a factor of six which is a reasonable time resolution for the rotation measurement at the Berkeley channel which has a current rise time of around 4 μs.

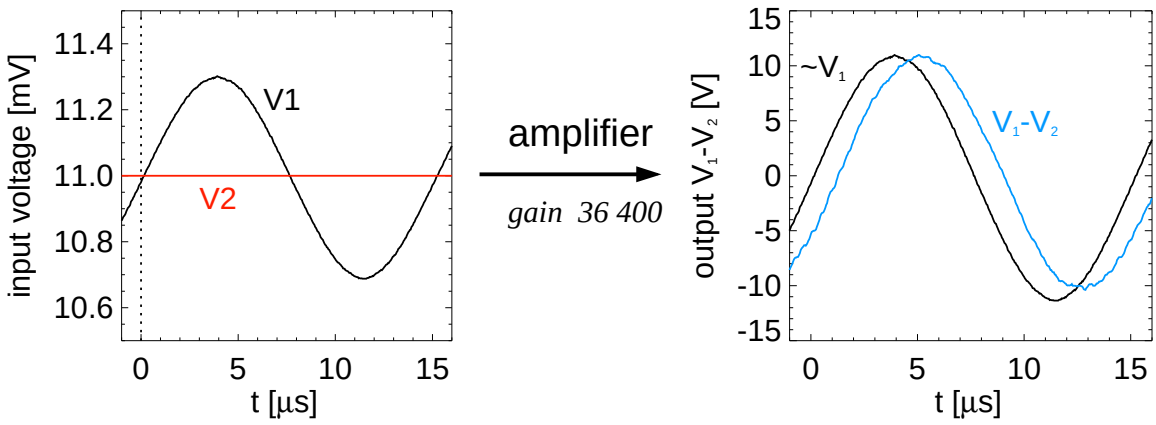

Figure 4.33: Performance test of the amplifier: The left graph shows the two input functions, the right graph the final amplifier output ($V_1 - V_2$) together with the sinusoidal input function scaled to the same maximum voltage.

Performance of the detectors The detectors were tested thoroughly for their time response and sensitivity and were found to work properly with the laser and the amplifier. However, they can be operated optionally with a thermoelectric (TE) cooler to keep the temperature at a constant value. It was found that the cooler causes a temperature gradient inside the detector and therefore an offset of the output signal in the order of 500 μV. This is an order of magnitude higher than the smallest signal which should be resolved. The connection from the cooler power supplies to the power line also creates a ground loop which introduces electromagnetic noise during a high current discharge. Both offset and noise are reduced considerably when the detector is operated without the cooler. In this case the cw laser should only be powered during the discharge to prevent unnecessary heating of the detectors. The sensitivity seems to be reduced by a factor of two when the detectors are not cooled. For all the following measurements the TE coolers where not used.

Optical stability The effect of vibrations of the optical components on the overall noise was tested previously in a slightly different setup with a 5 mW cw HeNe laser, two PIN diodes (EG&G FND-100), and a polarizing beam splitter cube using the same amplifier but with lower gain. A change of output voltage V_2-V_1 of 8 V was measured for a rotation of the laser polarization of 1^o. The noise on the scope at an average level of around 50 mV in the millisecond timescale increased up to 200 mV when the optical table was shaking. A rotation angle of 0.01^o corresponding to a signal of 80 mV could therefore be resolved in this setup. The same optical table and mounts are used for the CO_2 setup.

Other signals during a discharge Several tests were performed to investigate if signals from other effects can obscure the rotation signal. Figure 4.34 (a) shows a shot which was taken without analyzing polarizers. A rotation of the plane of polarization should in this case not cause any intensity change. However, both signals show a voltage change by up to 30% which is a bigger effect than the expected maximum Faraday rotation. Without the discharge or with the laser beam passing far outside of the channel a flat signal is recorded. The measured signal can be explained by deflections of the laser beam due to plasma density gradients. They play an important role, because they also scale with λ^2. This refraction introduces errors when it causes the beam to move across the nonuniform detector [Jar77]. In this experiment, the deflections were expected to be as big as 0.1^o. At a distance of 1.5 m this would cause a shift of

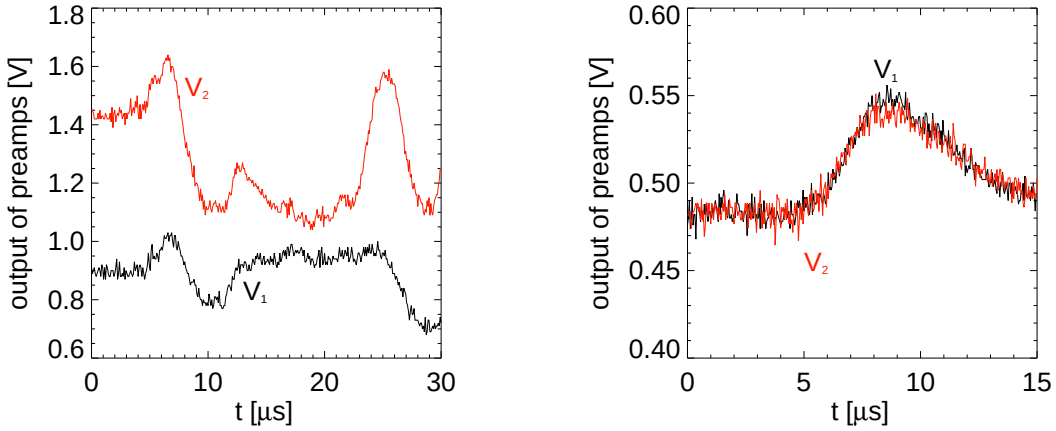

(a) Deflection due to electron density gradients

(b) Plasma self emission in infrared (2 – 12 μm)

Figure 4.34: Other signals during a high current discharge.

the laser beam of more than 2 mm at the detector which has an active area of 4x4 mm^2. The standard method for correcting deflections is to image the apparent position of the source of refraction onto the detector. For the shot in figure 4.34 (a) such an imaging lens was not used properly. Although a lens was introduced later which decreased this refractive effect by an order of magnitude the deflections could not completely be compensated because it was not possible to place the detector exactly in the image plane. Figure 4.34 (b) shows a shot without CO_2 laser. Both detectors measure a small plasma self emission in the wavelength range in which the detector is sensitive (2-12 μm). Since the signal is the same on both detectors it will be removed in the difference amplifier and is not an issue for the rotation measurement. Apertures before the final lenses with a small opening just big enough for the laser beam would reduce the plasma self emission furthermore considerably.

Performance of the CO_2 laser The first Faraday rotation measurements were performed with a surgical CO_2 laser which was not designed for scientific measurements. As a consequence it turned out that the laser output changed its plane of polarization in a periodic manner with an average frequency comparable to that of the power line (60 Hz). When no initial polarizer is used in the setup the intensity at the two detectors V_1, V_2 changes in such a way that the sum of both signals remains constant (left graph of figure 4.35). During the microsecond timescale of the discharge the laser output is constant. If the initial polarizer is used, oriented parallel to one of the polarization directions of the laser, the other one will be cut off (right graph of figure 4.35). It can then happen that the discharge is triggered at a time, where the laser output is low and the rotation measurement fails. The rather high extinction ratio of the Brewster polarizers which were used during these measurements ($\epsilon = 0.1$) allows 10% of the wrong polarization state to pass. The sudden drop of V_2 at 2.5 ms, 5.9 ms and 10.8 ms and consequently the increase of $V_1 - V_2$ by 1 V (right graph of figure 4.35) can be explained by this effect. Such an unequal variation of the intensities V_1 and V_2 causes big problems. Before the discharge is triggered the system must be adjusted to give a difference signal of zero. With such a laser this condition can never be realized. The rotation signal will always contain some offsets $(V_2 - V_1 + \text{offset}_1)/(V_1 + V_2 + \text{offset}_2)$ which reduce the accuracy. Different power on the detectors also changes the offsets differently which depend on the average temperature.

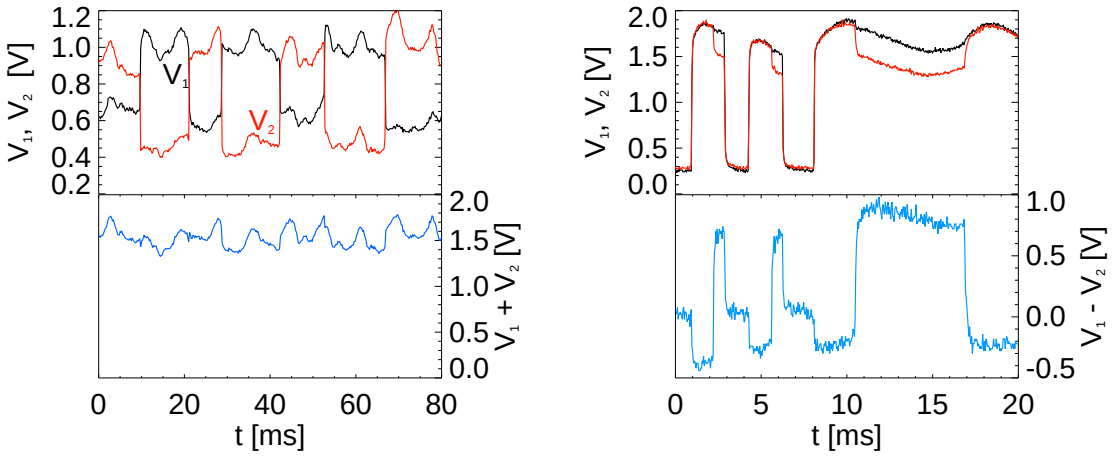

Figure 4.35: Left: Output V_1 and V_2 from the preamp without an initial polarizer. The sum stays basically constant. Right: The initial polarizer cuts off one state of polarization. The finite extinction of the polarizer allows some of the wrong polarization state to pass. The difference $V_2 - V_1$ is measured directly after the subtraction without the final amplification.

First rotation measurements

First preliminary measurements were performed with the surgical CO_2 laser mentioned above with reduced laser power and therefore reduced sensitivity of the setup. To overcome the problems caused by the changing polarization of the laser at least partially the offset in the difference signal measured shortly before the discharge ($t = -1\ \mu s$) was subtracted for each shot. The difference was measured at the final output of the amplifier, while the sum and the rotation $(V_2 - V_1)/(V_1 + V_2)$ were calculated manually after subtracting also the offsets from the two signals V_1 and V_2 directly after the preamps. Since deflections could not completely be compensated the rotation signal was extracted from the measured signal by a comparison of shots with and without an initial polarizer. Three shots without polarizer where averaged and subtracted from the average of three shots with initial polarizer. The measured rotation angles for different positions of the probing beam are shown in figure 4.36. The angles are given in arbitrary units since the difference and the sum were in this case measured at different stages of the amplifier and the angle is only proportional to $\Delta I/(I_1 + I_2)$ (equation 4.19). All signals show a delay of 1.5 μs which stems from the slow time response of the amplifier due to the higher gain (36400) which was used for this measurement. To measure at different positions, the probing beam can be moved across the discharge channel by means of two mirrors without changing the entering and exiting laser beams. The spot size of the beam inside the plasma is less than one millimeter to provide the desired spatial resolution. When the beam passes exactly through the center of the channel the rotation signal stays at zero throughout the discharge as expected. For negative positions the rotation is negative while at positive positions the rotation becomes positive since the magnetic field is reversed. The rotation profiles for $t = 2\ \mu s$, 3 μs and 4 μs are ploted in figure 4.37. For negative y the direction of the magnetic field is reversed and the rotation angles are negative. The maximum rotation at a radius of 3-5 mm indicates that most of the current flows within a small cylinder of about 1 cm diameter, which is desired for IFE transport. The magnetic field distribution can be calculated from $\varphi(y)$ and an independent measurement of the electron density $n_e(r)$ by an Abel inversion (compare equation 4.7):

$$B(r) = \frac{F(r)}{n_e(r)} r \ , \tag{4.29}$$

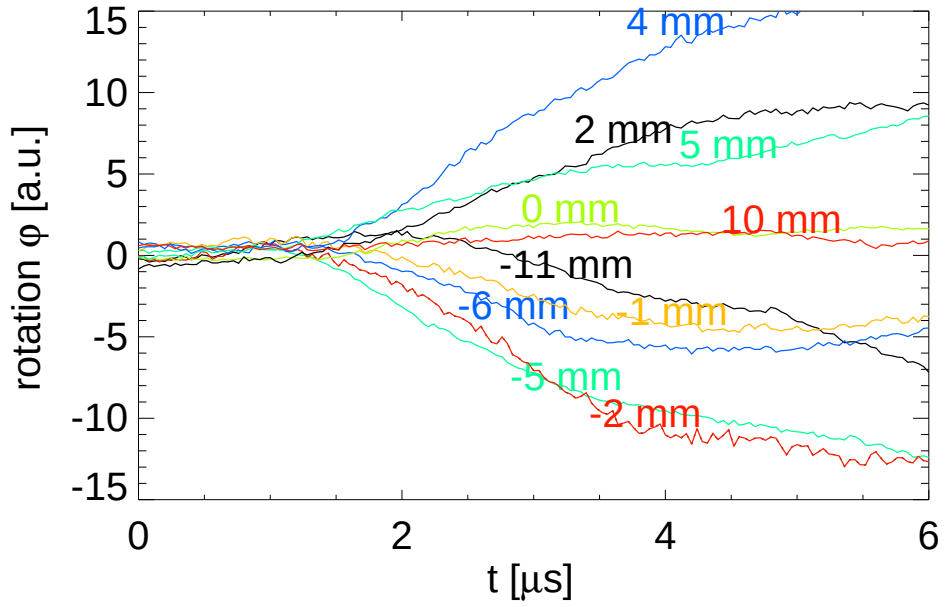

Figure 4.36: Rotation angle as a function of time for different positions of the probing beam.

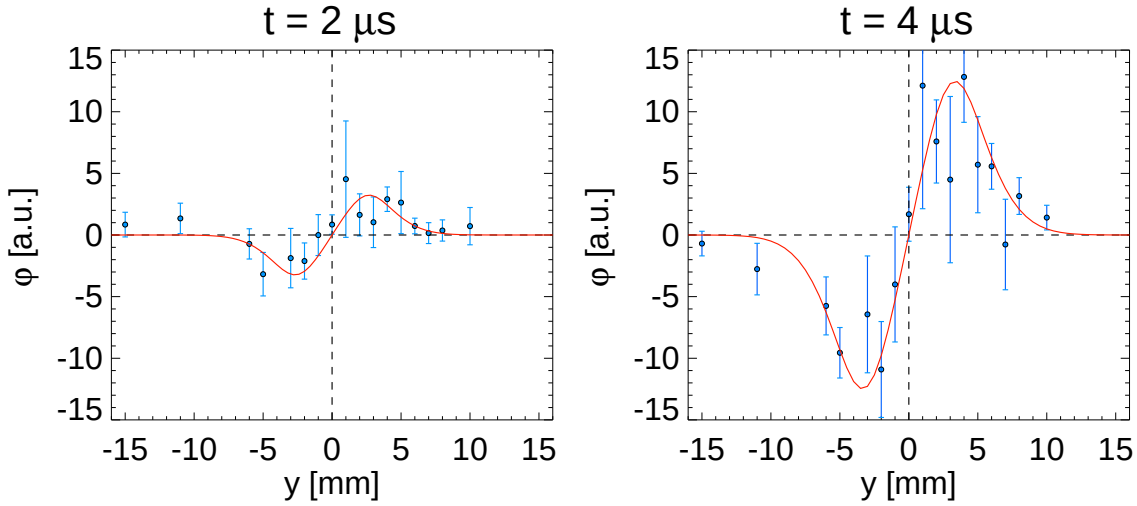

Figure 4.37: Rotation profiles for t = 2 μs, 3 μs and 4 μs. The error bars represent the standard deviation of six shots.

where

$$F(r) = -\frac{1}{\pi}\int_r^\infty \frac{\frac{d\varphi(y)}{dy}}{\sqrt{y^2 - r^2}} dy. \tag{4.30}$$

The magnetic field calculated in this way for a Gaussian electron-density distribution is shown in figure 4.38. The rotation profile $\varphi(y)$ was considered to be the red solid line in figure 4.37 at 4 μs. The magnetic field shows approximately a linear rise within the plasma column and a 1/r falloff outside. However, a slightly different fit through the data points in figure 4.37 would cause a very different current-density distribution. The error bars are in this measurement too big to make an accurate conclusion about the magnetic-field distribution.

The absolute angles can be estimated from a calibration of the setup. For this measurement

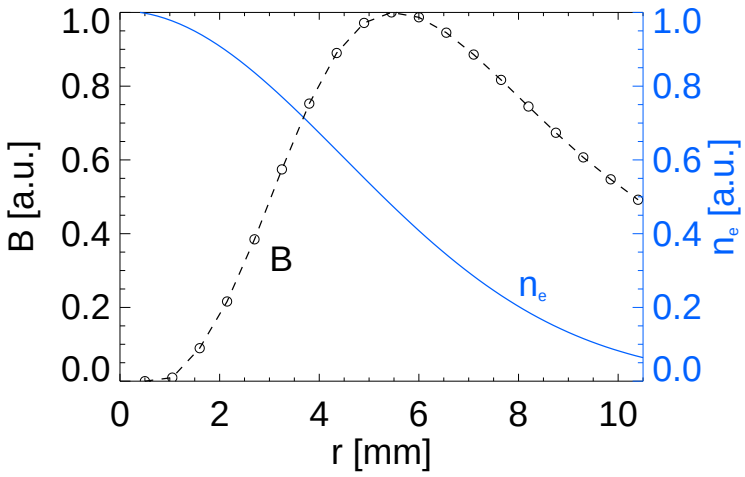

Figure 4.38: Abel inverted magnetic field distribution for a Gaussian electron density profile (blue) and the rotation profile from figure 4.37 (red solid line at 4 μs).

the initial polarizer is rotated by a certain angle and the response of the system $(V_2-V_1)/(V_1+V_2)$ is measured. The corresponding calibration factor depends on the half-shadow angle and can also be calculated from equation 4.19. Alternatively, the absolute magnetic field could also be estimated from the total discharge current, assuming that no parasitic currents flow outside the channel. For this first preliminary measurement presented here a calibration has not been done.

Conclusion

The first Faraday rotation has been measured. Experiments with reduced laser power, reduced sensitivity and the problems discussed above show that the setup works in principle. The data indicates that the current flow is confined within a small cylinder of circa 1 cm diameter during the first 5 μs. The errors (standard deviation of six shots per position) are at that time too high to make any conclusions about the current density distribution. In experiments with an improved optical setup we expect to measure with a sensitivity close to the design value. The polarimeter will be used together with a Michelson interferometer (chapter 4.1.1) to map the magnetic field distribution inside the plasma. For a proper measurement following points have to be improved:

- A better cw CO_2 is necessary with a stable polarization output and a maximum output power of 20 W (to yield 10 W after the beam splitter).
- Deflections must be better accounted for by lenses which image the plasma onto the detectors. At the same time the laser spot at the active area of the detectors should be as big as possible (around 3 mm diameter) to allow a maximum power of 0.5 W.
- A better extinction ratio of the polarizers can be achieved by using two Brewster windows in a row ($\epsilon = 0.1 \cdot 0.1 = 0.01$ as required) for each of the three polarizers.
- With 10 W available after the beam splitter the gain of the amplifier can be reduced to a gain of 6500 which will improve the time response by a factor of six.

Measurements with an improved setup of the polarimeter will be reported in the PhD thesis of D. Ponce [Pon02].

4.2 Visible spectroscopy of the plasma-self emission

4.2.1 Setup of the spectrometer

The self emission of the channel plasma at GSI was investigated by spectroscopy in the visible range. Spectra were taken 'side-on' by a grating spectrograph of the Czerny-Turner type (Jarrell-Ash Monospec 27) with a focal length of 275 mm and an aperture of f/3.8. The discharge light was collected by a f = 0.2 m lens mounted directly behind the quartz vacuum window onto the entrance slit of the spectrometer. The apparatus line broadening for an entrance slit of 20 μm and a grating with 1200 grooves/mm had a width of 0.36 nm (FWHM). This value was experimentally derived from Hg lines in a spectrum from a calibration lamp. The apparatus line profile can have a Gauss or a Lorentz shape. In this case it was a Lorentz profile. The spectra were recorded by a streak camera (Hamamatsu C2830) with the entrance slit located in the focal plane of the spectrometer. The time resolution as determined by the slit width of the streak unit was 250 ns at a streak time of 13.8 μs. Even with this exposure time and without a spatial resolution of the measurement the intensity was so weak that up to ten spectra from different discharges had to be averaged to obtain a useful spectrum. Small differences in the discharge delay due to the jitter of the breakdown were accounted for during the superposition of the individual spectra. The spectral sensitivity of the whole system including camera, the spectrometer and the optical components was measured with a spectral lamp of known characteristics. All measured spectra were corrected with this transmission function.

4.2.2 Density measurements from the Stark broadening of hydrogen lines

Discharges in NH_3 produce a number of hydrogen and nitrogen lines when the gas is dissociated into its constituents. The time resolved spectra of a 45 kA discharge in 10 mbar ammonia

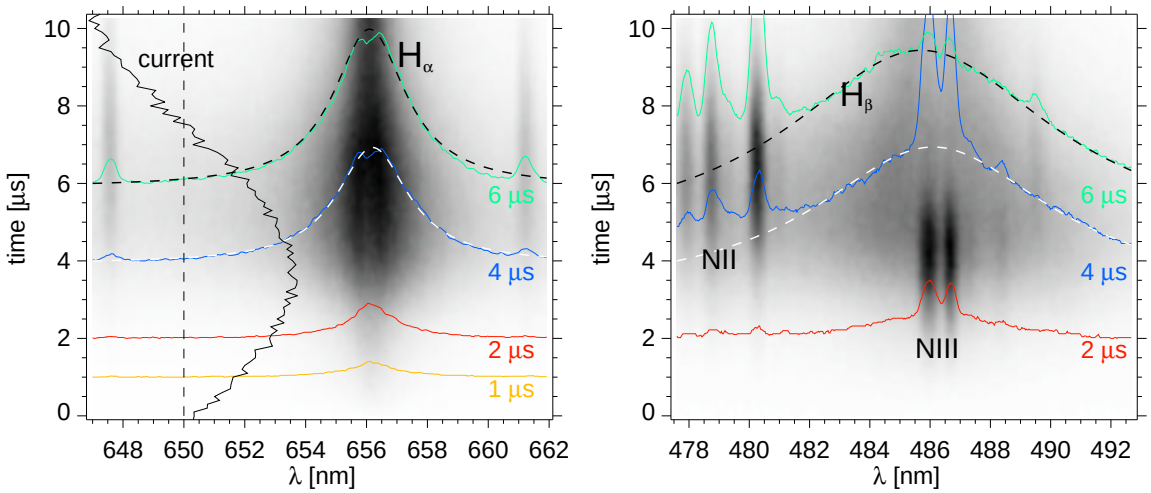

Figure 4.39: Time resolved images and spectra of the H_α and the H_β Balmer lines for a 45 kA discharge in 10 mbar ammonia. The colored curves show the spectral distribution for different times in arbitrary units. The black curve in the left figure shows the temporal evolution of the discharge current. The profiles at 4 and 6 μs were fitted with a Lorentz curve (dashed lines) in order to determine the experimental line width.

from figure 4.39 show a strong appearance of the hydrogen Balmer lines H_α and H_β at 656 nm and 486 nm respectively. For both lines the maximum line emission occurs after the current maximum of the discharge at around 6 μs. At this time the lines indicate a broadening of about 3 nm for H_α and up to 10 nm for H_β. Several effects can cause line broadening in a

plasma [Gri64]. The dominant line-broadening mechanism in dense plasmas ($n_e > 10^{15} cm^{-3}$, $T_e < 10\ eV$) is Stark broadening caused by the electric microfields of the free electrons and ions which surround the radiating atoms. Since hydrogen is subject to a linear Stark effect, the Balmer lines experience a pronounced Stark broadening which depends strongly on the density but minor on the temperature. Experimentally obtained Stark profiles can therefore be used as a measure of electron density [Hil67]. The Stark broadening of the nitrogen lines is too small so that those line widths are determined by the apparatus broadening. According to [Gri64] the electron density can directly be obtained from the linewidth $\Delta\lambda$ of the hydrogen Balmer lines by the empirical relation

$$n_e = C\Delta\lambda^{3/2} \tag{4.31}$$

where $C = 3 \cdot 10^{15} \text{Å}^{-3/2} cm^{-3}$ for H_α and $2.5 \cdot 10^{14} \text{Å}^{-3/2} cm^{-3}$ for H_β at an electron density of $5 \cdot 10^{17}\ cm^{-3}$. C depends only weakly on n_e and T. However, the ratio $C(H_\alpha)/C(H_\beta)$ changes from around 128 for $10^{16} cm^{-3}$ down to 12 at a density of $5 \cdot 10^{17} cm^{-3}$, so an initial guess of the plasma density is required for a good accuracy. The measured Balmer lines are fitted by a Lorentz curve and the line width is determined as the full width half maximum (FWHM). The Stark-line broadening follows from this measured line width by a deconvolution of the apparatus line width. Since the apparatus broadening has a Lorentz shape its line width can be simply subtracted from the measured line width to obtain the contribution from the Stark effect: $\text{FWHM}_{\text{Stark}} = \text{FWHM}_{\text{measured}} - 0.36$ nm. This method yields an electron density of $3.8 \cdot 10^{17} cm^{-3}$ for the H_α and $2.7 \cdot 10^{17} cm^{-3}$ for the H_β line at t = 6 μs in figure 4.39. The electron densities for other discharge conditions are summarized in figure 4.40. The density shows a smooth evolution in time with a distinct maximum for all pressures. At higher pressures the electron density increases, reaching a maximum of around $9 \cdot 10^{17} cm^{-3}$ for 17 mbar. The peak density is reached at 4, 5 and 6 μs for a 17, 10 and 5 mbar gas fill respectively. The densities derived from the H_β broadening are in all cases by a factor of 1.6 or more lower than the ones from H_α. The bars in figure 4.40 indicate the error returned by the Lorentz fitting routine. Since the wings are not visible and several intense nitrogen lines are superimposed to the line profile the real error can be larger. For pressures higher than 10 mbar also the wings of the H_α line are cut by the limited field of view. The integrated plasma emission from all regions of the channel has contributions from very different electron densities which can effect the line shape and introduce additional errors. Even the presence of nitrogen could influence the profiles of the Balmer lines. The measured half-width ratio H_α/H_β in this experiment is between 0.24 and 0.32 depending on the pressure. Other experiments [Wie72, Gri74] measured a ratio of around 0.22 at a density of $10^{17} cm^{-3}$. The spectroscopic measurements show the same temporal evolution of the electron density as the interferometric results (figure 4.7). The times of the maximum density agree within a few hundreds of ns. However, the absolute density values obtained from the spectroscopy are by a factor of two smaller than the ones from interferometry. This observation is due to the line integrated spectroscopic measurement, which yields a smaller averaged value of the entire density distribution.

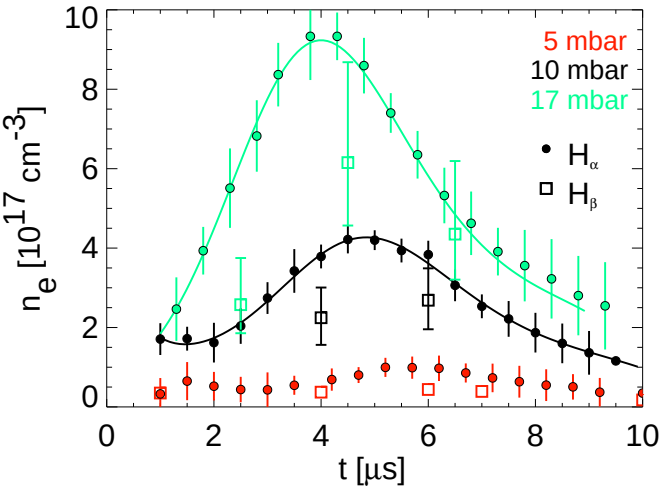

Figure 4.40: Electron densities estimated from the H_α and H_β lines by equation 4.31 for different gas pressures.

A detailed line shape analysis of the Stark-broadened Balmer lines includes the ion-microfield distribution in the APEX-approximation, the electron broadening as well as the ion Doppler broadening [Lee01]. The results for a temperature of 5 eV and a density of $1 \cdot 10^{17} cm^{-3}$, $2 \cdot 10^{17} cm^{-3}$ and $5 \cdot 10^{17} cm^{-3}$ are compared with the measurements for a 45 kA discharge at 5 and 10 mbar, 4 μs after the breakdown (figure 4.41). The intensities of all experimental and theoretical lines are normalized to the H_α line. Figure 4.41 shows that the electron density in

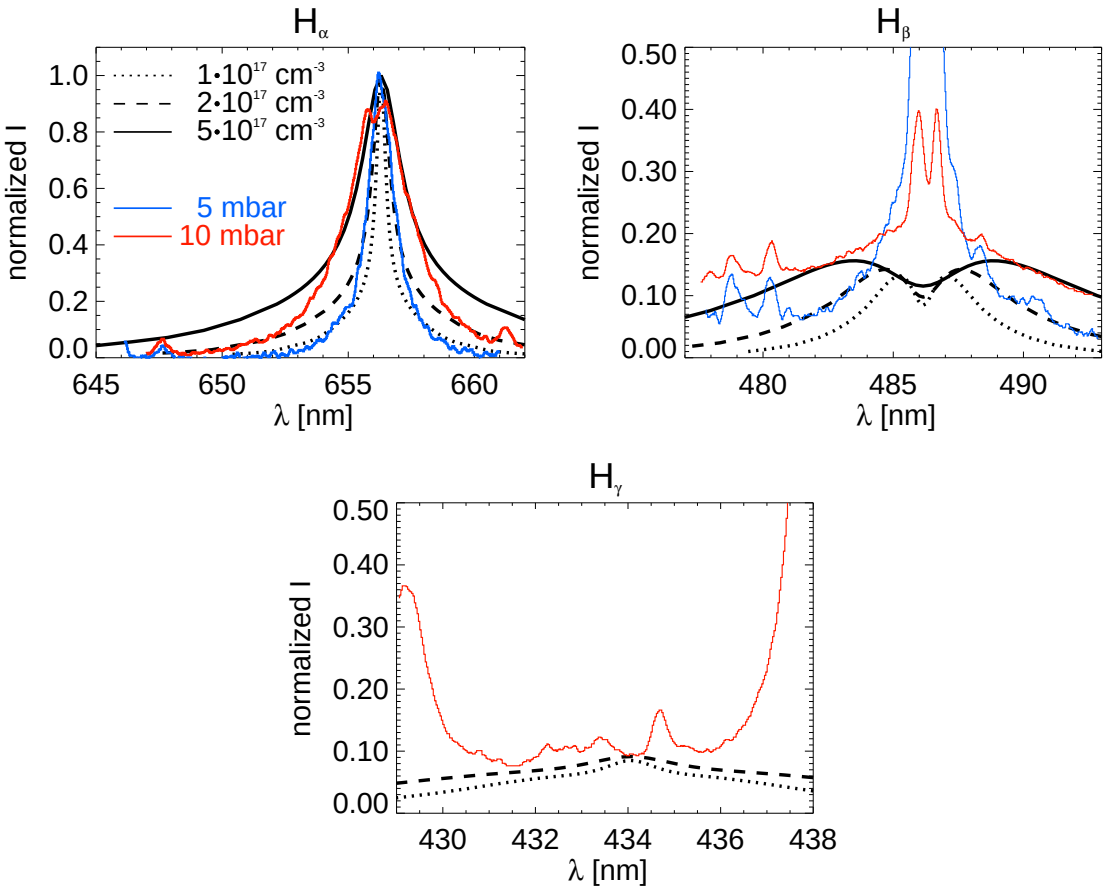

Figure 4.41: Comparison of measured (solid lines) and simulated [Lee01] (dotted lines) profiles of H_α, H_β and H_γ.

the 5 mbar discharge is between $1 \cdot 10^{-17}$ and $2 \cdot 10^{17} cm^{-3}$. At 10 mbar the density is around $5 \cdot 10^{-17} cm^{-3}$. The values derived from equation 4.31 give for 5 mbar an electron density smaller by a factor of two. In the 10 mbar case they are different only by 20 %. The H_β line can not be fitted by the theoretical line due to the intense superimposed nitrogen lines. The H_γ line was not seen in the experiments since the line is very broad and the intensity too small, in agreement with the simulation. A better consistence between the simulated and the measured H_β line can be seen in figure 4.42 which shows the spectrum of a 17 mbar discharge 10 μs after the breakdown. At that late time the temperature has dropped so much that the intensity of the nitrogen lines is weak compared to the intensity of the H_β line and the double structure of H_β becomes visible. While H_β can be described well by the theoretical line profile for $1 \cdot 10^{17} cm^{-3}$, H_α rather fits to a density between $2 \cdot 10^{17}$ and $5 \cdot 10^{17} cm^{-3}$.

A line profile can be forged by self absorption, if the optical thickness of the plasma is too high. A simple estimation gives an optical thickness around $\tau_0 \approx 2$ in this plasma for the H_α line [Ros01b]. This would increase the width by roughly 30% which would explain the difference in densities determined from H_α and H_β.

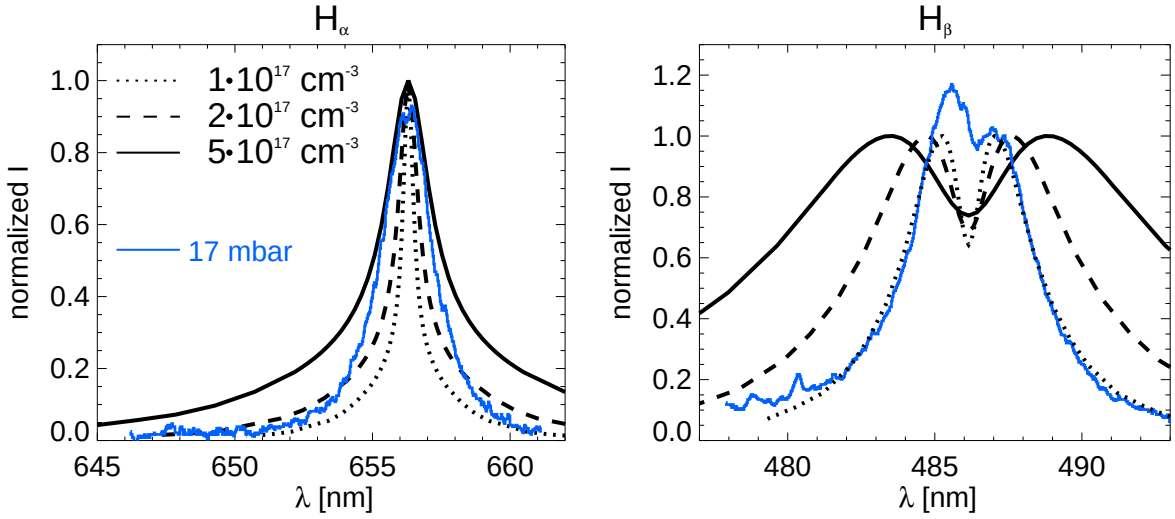

Figure 4.42: Comparison of measured (solid lines) and simulated (dotted lines) profiles of H_α and H_β. The blue curve shows the spectrum of a 17 mbar discharge 10 μs after the breakdown when the nitrogen lines are weak compared to the H_β line.

The central dip in the H_α profile which can be seen in figures 4.39 (a) and 4.41 was also observed in other experiments [Hil67]. There the dip was explained by a line reversal due to an increased excitation temperature in the center of the plasma and as a consequence the H_α line was abandoned for accurate density measurements.

4.2.3 Rate modeling of a nitrogen plasma

Since no electron temperature diagnostic was used so far at the two transport channel experiments a spectroscopic method is interesting. At very high densities, the electron temperature can be obtained from the relative intensities of nitrogen lines either of the same atom or ion, or neighboring ionization states [Gri64, Tho88]:

$$\frac{I_{ji}}{I_{kl}} = \frac{\lambda_{kl} A_{ji} g_j}{\lambda_{ji} A_{kl} g_k} exp\left(-\frac{E_j - E_k}{kT_e}\right) \tag{4.32}$$

where λ is the central wavelength of the line, g the statistical weight and A the spontaneous transition probability. The statistical weight gives the number of degenerate states in the level. Often more than two lines are compared and presented in a so called Boltzmann-plot to improve the accuracy of the temperature measurement. Figure 4.43 shows a spectrum with several nitrogen NII and NIII lines for a 45 kA discharge in 10 mbar ammonia.Nitrogen NII lines show their highest intensity at around 6 μs while the NIII lines peak earlier at about 4 μs. At this time when the current maximum is reached and the channel diameter is still small the highest temperature is expected. After the current maximum the channel expands and the temperature drops. The intensity of the NIII lines decreases while the NII lines take over, because NII has a lower ionization energy than NIII and the density of NII peaks at lower temperatures than that of NIII.

Since equation 4.32 is not valid at the low densities and high temperatures encountered in the channel plasma [Mew67], the population densities of different nitrogen levels are calculated by a collisional radiative model including electron impact ionization I, three - body recombination T, radiative recombination RR, dielectronic recombination DR, collisional excitation C as well as spontaneous transition A.

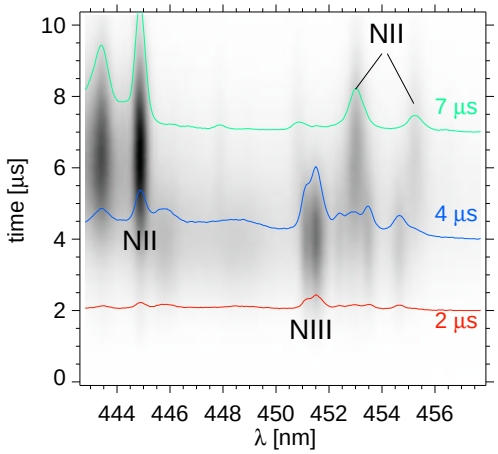

Figure 4.43: Time resolved spectrum showing nitrogen NII and NIII lines.

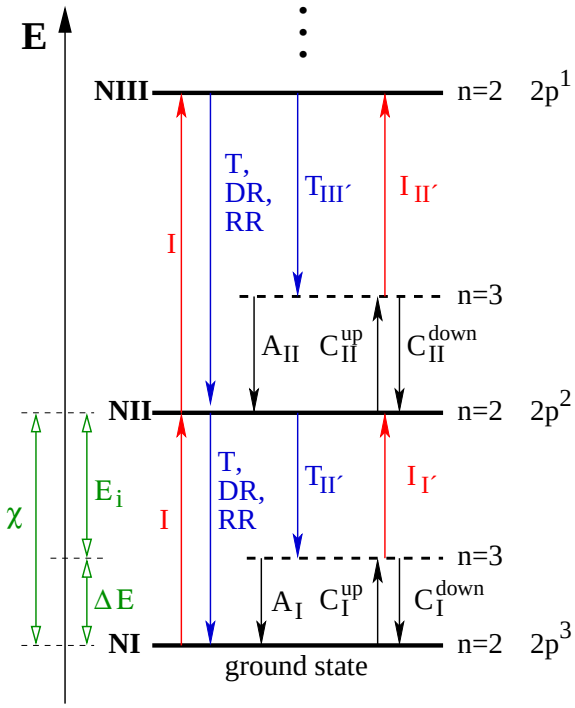

Figure 4.44: Nitrogen ground levels, first excited states (n=3) and the transitions included in the rate balance.

All the ground states from NI (neutral) to NVIII (fully ionized) are included. Excited states with principal quantum number n=3 for NI to NV are included since most of the observed NII and NIII lines belong to a transition from this energy level. Figure 4.44 shows schematically the selected atomic and ionic system and the relevant collisional and radiative processes for the first two ionization stages. The influence of higher lying levels have been partially included employing effective rate coefficient for dielectronic and radiative recombination (see below and Appendix). In the case of L-shell configurations, the number of levels of the type $1s^2 2s^n 2p^m 3l$ with $n+m = 1-4$ is enormous and can hardly be treated in a detailed LSJ-splitting model. As these levels are rather close to each other in energy, the various physical processes between all levels can be separated employing an average level in the rate equations representing all excited states of one configuration and a detailed configuration account for the spectral distribution [Ros01]. At moderate densities, the population densities between the single excited $1s^2 2s^n 2p^m 3l$- levels show a Boltzmann-distribution

$$\frac{n_i}{n_j} = \frac{g_i}{g_j} e^{-E_{ij}/T_e} \tag{4.33}$$

and the spectral distribution is reduced to [Ros00]

$$I(\omega) = \sum_{k=I}^{V} \sum_i \sum_j n_3^k A_{ji}^k \frac{g_j^k}{g^k} exp\left(-[E_j^k - E_0^k]/kT_e\right) \phi_{ji}^k(\omega) \tag{4.34}$$

where k characterizes the ionization stage (i.e. k=1 corresponds to NI), E_0^k is the reference energy level for the excited n=3 states for each ionization stage, n_3^k is the population density

of the averaged excited state of ionization stage k and ϕ^k_{ji} is the line profile (i.e. in this case determined by the apparatus line shape). If the electron temperature is sufficiently large, the exp-factor is close to one. The population densities of the excited states are calculated from a system of collisional radiative rate equations.

Rate equations

The number of transitions per unit time for a certain rate coefficient is given by $N_I = n \cdot I$, $N_{RR} = n \cdot RR$ etc. where n is the density of the level from where the transition occurs. In the following the population densities of the ground levels will be called $n(NI)$, $n(NII)$, ... and the densities of the excited states $n(NI_{n=3})$, $n(NII_{n=3})$, ... The notation $I_{I,II}$ will be used for the ionization rate in s^{-1} from the NI ground state to the NII ground state, while I_I represents the ionization rate from the first excited state of NI to the ground state of NII. The three-body recombination from the NII ground state to the excited level of NI is called T_{II}, the collisional excitation rates from and to the ground state of NI C^{up}_I and C^{down}_I and so on. The meaning of the different rate coefficients in illustrated in figure 4.44. In the case of an equilibrium the population densities of all the levels must be constant in time. Therefore we can write a rate equation for every level.For the ground states of nitrogen the balance equations become:

$$\begin{aligned}\frac{dn(NI)}{dt} = 0 = &-n(NI)\cdot[I_{I,II} + C^{up}_I] + n(NII)[\cdot T_{II,I} + RR_{II,I} + DR_{II,I}] \\ &+n(NI_{n=3})\cdot[A_I + C^{down}_I] \qquad (4.35)\\ \frac{dn(NII)}{dt} = 0 = &\, n(NI)\cdot I_{I,II} - n(NII)[T_{II,I} + RR_{II,I} + DR_{II,I} + I_{II,III} + C^{up}_{II}] + \\ &+n(NIII)[RR_{III,II} + DR_{III,II} + T_{III,II}] + \\ &+n(NI_{n=3})\cdot I_I + n(NII_{n=3})\cdot[A_{II} + C^{down}_{II}] \qquad (4.36)\\ &\vdots\end{aligned}$$

The first term in equation 4.35 describes the loss of electrons due to the ionization and excitation processes out of the ground state of NI. Recombination processes from the NII ground state are described by the second term while the last term contains the transitions to the first excited level. In a similar way the balance equations for the first excited states become:

$$\begin{aligned}\frac{dn(NI_{n=3})}{dt} = 0 = &\, n(NI)\cdot C^{up}_I + n(NII)\cdot T_{II} - n(NI_{n=3})\cdot[A_I + C^{down}_I + I_I] \qquad (4.37)\\ \frac{dn(NII_{n=3})}{dt} = 0 = &\, n(NII)\cdot C^{up}_{II} + n(NIII)\cdot T_{III} \\ &-n(NII_{n=3})\cdot[A_{II} + C^{down}_{II} + I_{II}] \qquad (4.38)\\ &\vdots\end{aligned}$$

The whole system is described by eight balance equations for the ground states and five equations for the first excited level. The rate equation for the nucleus $dn(NVIII)/dt$ is replaced by the normalization condition

$$\begin{aligned}&n(NI) + n(NII) + n(NIII) + n(NIV) + n(NV) + n(NVI) + +n(NVII) + n(NVIII) + \\ &+n(NI_{n=3}) + n(NII_{n=3}) + n(NIII_{n=3}) + n(NIV_{n=3}) + n(NV_{n=3}) = 1. \qquad (4.39)\end{aligned}$$

A complete set of the used balance equations can be found in appendix A.2. Equations 4.35 to 4.39 describe a linear system of the form

$$\mathcal{A} \cdot \begin{pmatrix} n(NI) \\ \vdots \\ n(NVIII) \\ \hline n(NI_{n=3}) \\ \vdots \\ n(NV_{n=3}) \end{pmatrix} = \begin{pmatrix} 0 \\ \vdots \\ 0 \\ \hline 1 \end{pmatrix} \tag{4.40}$$

with the matrix

$$\mathcal{A} = \left(\begin{array}{ccccccccccccc} a_{11} & a_{12} & 0 & 0 & 0 & 0 & 0 & 0 & b_{11} & 0 & 0 & 0 & 0 \\ I_{I,II} & a_{22} & a_{23} & 0 & 0 & 0 & 0 & 0 & I_{I'} & b_{22} & 0 & 0 & 0 \\ 0 & I_{II,III} & a_{33} & a_{34} & 0 & 0 & 0 & 0 & 0 & I_{II'} & b_{33} & 0 & 0 \\ 0 & 0 & I_{III,IV} & a_{44} & a_{45} & 0 & 0 & 0 & 0 & 0 & I_{III'} & b_{44} & 0 \\ 0 & 0 & 0 & I_{IV,V} & a_{55} & a_{56} & 0 & 0 & 0 & 0 & 0 & I_{IV'} & b_{55} \\ 0 & 0 & 0 & 0 & I_{V,VI} & a_{66} & a_{67} & 0 & 0 & 0 & 0 & 0 & I_{V'} \\ 0 & 0 & 0 & 0 & 0 & I_{VI,VII} & a_{77} & a_{78} & 0 & 0 & 0 & 0 & 0 \\ \hline C_I^{up} & T_{II'} & 0 & 0 & 0 & 0 & 0 & 0 & d_{11} & 0 & 0 & 0 & 0 \\ 0 & C_{II}^{up} & T_{III'} & 0 & 0 & 0 & 0 & 0 & 0 & d_{22} & 0 & 0 & 0 \\ 0 & 0 & C_{III}^{up} & T_{IV'} & 0 & 0 & 0 & 0 & 0 & 0 & d_{33} & 0 & 0 \\ 0 & 0 & 0 & C_{IV}^{up} & T_{V'} & 0 & 0 & 0 & 0 & 0 & 0 & d_{44} & 0 \\ 0 & 0 & 0 & 0 & C_V^{up} & T_{VI'} & 0 & 0 & 0 & 0 & 0 & 0 & d_{55} \\ \hline 1 & 1 & 1 & 1 & 1 & 1 & 1 & 1 & 1 & 1 & 1 & 1 & 1 \end{array}\right).$$

The 13x13 matrix $\mathcal{A}$ can be divided into four submatrices A,B,C and D as indicated by the horizontal and vertical lines. Each row describes one of the 12 balance equations. The bottom row of 'ones' represents the normalization. Most elements of the matrix are zero since only transitions from neighboring levels are possible. The submatrix A contains the transitions from and to the ground states. The matrix element $a_{11} = -(I_{I,II} + C_I^{up})$ describes the loss of electrons in NI towards NII and $NI_{n=3}$. The element $a_{12} = T_{II,I} + RR_{II,I} + DR_{II,I}$ represents the gain of electrons for NI at the cost of NII while a_{22} describes the loss of NII. The submatrix B represents all the transitions from the first excited level towards the ground state: $b_{11} = A_I + C_I^{down}$. A complete list of the matrix elements can be found in appendix A.2. The system of linear equations is solved numerically. First the *singular value decomposition (SVD)* of the matrix $\mathcal{A}$ as the product of orthogonal and diagonal arrays is computed. SVD is a very powerful tool for the solutions of linear systems, and is often used when a solution cannot be determined by other numerical algorithms. The linear system is then solved by *back-substitution* from the vectors returned by the SVD. The functions `svdcmp` and `svbksb` from the *Numerical Recipes* [Pre92] were used for those tasks.

The processes which are included in the model will be described briefly in the following:

Collisional ionization

Collisional ionization describes the process of a free electron releasing a bound electron from an atom or ion by collision:

$$N^Z + e \longrightarrow N^{Z+1} + 2e.$$

Collisional ionization can occur to a continuum of states provided that the incident electron energy ϵ is bigger than the ionization potential χ_i. The rate coefficient can be written in a

classical approximation [Sob95] by

$$I_{ij} = n_e < \sigma_i v >= n_e \cdot 10^{-8} \cdot 6\ m_i \left(\frac{Ry}{\chi_i}\right)^{3/2} \beta^{-1/2} exp(-\beta) f(\beta) \qquad [s^{-1}] \tag{4.41}$$

where $Ry = 13.6058\ eV$ is the Rydberg constant, m_i the number of electrons in the shell to be ionized and χ_i the ionization potential. The functions β and $f(\beta)$ are defined as

$$\beta := \frac{\chi_i}{kT_e}, \tag{4.42}$$

$$f(\beta) := -\beta \cdot exp(\beta) Ei(-\beta). \tag{4.43}$$

The *exponential integral* Ei is defined [Hut87, Sob95] as

$$Ei(y) := \int_y^\infty \frac{exp(-s)}{s} ds \tag{4.44}$$

and can be approximated by

$$Ei(-\beta) = -e^{-\beta} ln\left[1 + \frac{0.562 + 1.4\beta}{\beta(1 + 1.4\beta)}\right]. \tag{4.45}$$

Table 4.2 summarizes the parameters of the ground levels of nitrogen, including electron configuration, ionization energy χ_i, statistical weight g_i of the averaged lower n=2 level and the number of electrons m_i. The ionization cross sections have alternatively been calculated with

species	ground state	ionization energy χ_i	g_i	m_i
NI	$1s^2 2s^2 2p^3$	14.534 eV, 117225.7 cm^{-1}	20	3
NII	$1s^2 2s^2 2p^2$ (C-like)	29.601 eV, 238750.50 cm^{-1}	15	2
NIII	$1s^2 2s^2 2p^1$ (B-like)	47.448 eV, 382703.8 cm^{-1}	6	1
NIV	$1s^2 2s^2$ (Be-like)	77.472 eV, 624866 cm^{-1}	28	2
NV	$1s^2 2s$ (Li-like)	97.888 eV, 789537.2 cm^{-1}	8	1
NVI	$1s^2$ (He-like)	552.057 eV, 4452758 cm^{-1}	1	2
NVII	$1s$ (H-like)	667.029 eV, 5380089 cm^{-1}	2	1
NVIII	(nucleus)	-	1	-

Table 4.2: The ground states of nitrogen [Wie96].

the Coulomb - Born - Exchange approximation with effective potential and corresponding rate coefficients have been fitted to analytic formulas [Ros01b], listed in table A.2 in the appendix.

Radiative recombination

The radiative recombination process is represented by

$$N^{Z+1} + e + \epsilon \rightarrow N^Z + h\nu$$

where

$$h\nu = \chi - E_j + \epsilon, \tag{4.46}$$

ϵ is the kinetic energy of the free electron, $h\nu$ the energy carried away by the emitted photon and $\chi - E_j$ the energy released by the transition [Tho88]. The positive energy states above the ionization limit are not quantized, so the radiation is a continuum. The radiative recombination

coefficients were calculated by several authors. In this model the coefficients given by Aldrovandi [Ald73] are used which were fitted to the expression:

$$RR = n_e < \sigma v >= n_e \cdot A_{rad} \left(\frac{T_e}{10^4} \right)^{-\eta} \tag{4.47}$$

The two parameters A_{rad} and η for NI to NVI are given in table A.1 in appendix A.1. For NVII ($RR_{VIII,VII}$) an analytic expression [Sob95] was used:

$$RR = \frac{32\sqrt{\pi}a_0\hbar}{3\sqrt{3} \cdot m \cdot 137^3} Z n_1 \beta^{1/2} \cdot \left[ln(1.78\beta_1) - exp(\beta_1) Ei(-\beta_1) \left(1 + \frac{\beta_1}{n_1} \right) \right] \tag{4.48}$$

where $n_1 = 1$, $Z = 7$ and $\beta_1 = Z^2 Ry/n_1^2 T$. The classical electron radius $a_0 = 5.29 \cdot 10^{-9} cm$, the electron mass $m_e = 9.11 \cdot 10^{-28} g$ and $\hbar = 1.05 \cdot 10^{-27} erg\ s$ are given in *cgs*-units.

Alternatively, quantum mechanical calculations of photoionization cross sections have been performed and corresponding radiative rate coefficients have been fitted into a four-parameter analytical expression [Ros01b]. The fitting parameters are tabulated in appendix A.1.

Dielectronic recombination

The dielectronic recombination is defined by the process

$$N^{Z+1} + e(E_2) \rightarrow N^{Z**} + h\nu_1 \rightarrow N^{Z*} + h\nu_2 \rightarrow N^Z + h\nu_3$$

The first step is the capture of a continuum electron by N^{Z+1} into an doubly excited state N^{Z**}. The autoionizing state is stabilized by a radiative transition [Gab72]. Like in the case of the radiative recombination a fitted formula was used for the rate coefficients which was calculated by [Ald73]:

$$DR = n_e \cdot A_{di} T_e^{-3/2} exp(-T_0/T_e)(1 + B_{di} exp(-T_1/T_e)) \tag{4.49}$$

The coefficients A_{di}, T_0, T_1 and B_{di} are given in table A.1 in appendix A.1.

Three-body recombination

In high-density plasmas the dominant recombination mechanism is three-body recombination. In the case of a Maxwellian electron distribution the rate coefficient can directly be calculated from the rate coefficient for collisional ionization I_{ij} by the principle of detailed balance [Ros98]:

$$\begin{aligned} T_{ji} &= I_{ij} \frac{g_i}{2g_j} \left(\frac{2\pi\hbar^2}{m_e k T_e} \right)^{3/2} exp\left(\chi_i / kT_e\right) \\ &= n_e \cdot I_{ij} \cdot 1.656 \cdot 10^{-22} \frac{g_i}{g_j} \frac{exp(\chi_i/kT_e]}{(kT_e)^{3/2}} \qquad [s^{-1}] \end{aligned} \tag{4.50}$$

Spontaneous transition probabilities

The spontaneous transition probabilities from the averaged first excited states (n=3) to the ground states (n=2) were calculated from a summation over detailed LSJ-split Hartree-Fock rates [Ros01b]. The results used in the rate model as well as the statistical weights, the excitation energies and the ionization potentials of the excited states are summarized in table 4.3.
Here $\bar{A} = \frac{\sum g_i \cdot A_{ij}}{\sum g_i}$ is the sum of all transition probabilities and $E_i = \chi - \Delta E$ the ionization energy.

Z	$\bar{A}$ $[s^{-1}]$	$g_{low}(n=2)$	$g_{up}(n=3)$	λ [Å]	ΔE $[eV]$	E_i $[eV]$
1 (N-like)	$3.30 \cdot 10^{10}$	20	270	1189	10.4	4.1
2 (C-like)	$1.68 \cdot 10^{11}$	15	108	571	21.7	7.9
3 (B-like)	$1.26 \cdot 10^{11}$	6	18	369	33.6	13.8
4 (Be-like)	$2.08 \cdot 10^{12}$	28	144	281	44.1	33.4
5 (Li-like)	$5.29 \cdot 10^{11}$	8	18	246	50.4	47.5

Table 4.3: Spontaneous transition probabilities $\bar{A}$ used for the balance equations.

Collisional excitation rates

The collision rates from the ground state to the first excited state C^{up} are calculated by the Van Regemorter formula [Reg62]

$$C^{up} =< v\sigma(n \to n') >= 3.15 \cdot 10^{-7} f(n \to n') \left(\frac{Ry}{\Delta E}\right)^{3/2} \sqrt{\beta_n} e^{-\beta_n} p(\beta_n) \tag{4.51}$$

where $\beta_n = \Delta E / kT_e$ and ΔE is the excitation energy given in table 4.3. The oscillator strength f and the Gaunt factor $p(\beta_n)$ are given in appendix A.1.4. The rates for transitions from the excited state to the ground state C^{down} are derived from C^{up} by the assumption of a detailed balance

$$n \cdot n_e \cdot C^{up} = n' \cdot n_e \cdot C^{down}.$$

From the Boltzmann equation (4.33) follows that

$$C^{down} = C^{up} \cdot \frac{n}{n'} = C^{up} \cdot \frac{g_{low}}{g_{up}} \cdot e^{-\Delta E / kT_e} \tag{4.52}$$

with g_{low} and g_{up} given in table 4.3.

The rate coefficients for ionization, three-body recombination as well as dielectric and radiative recombination for a transition from the NII ground state are plotted for comparison in figure 4.45. The ionization is for temperatures higher than a few eV by far the dominant process.

Results of the rate model

The population densities of the ground levels as computed by the rate model are shown in figure 4.46. Alternatively the densities were calculated by the Saha equation

$$\frac{N_{Z+1}}{N_Z} = \frac{2(2\pi m k T_e)^{3/2}}{h^3 n_e} \cdot \frac{g_{Z+1}}{g_Z} \cdot exp\left(-\chi_Z / kT_e\right), \tag{4.53}$$

where g_{Z+1} and g_Z are the statistical weights (g_{low}) from table 4.3 and χ_Z is the ionization energy of the ionization state N_Z (table 4.2). The density of the atom N_1 was set to an arbitrary initial value and N_2 was calculated by equation 4.53. Then N_3 is calculated from N_2 and so on. Finally the densities are normalized to one. Figure 4.46 compares the densities from the Saha equation (dashed lines) with the results from the rate model (solid lines) for a density of $5 \cdot 10^{17}$ cm^{-3} as present in the channel plasma and a much higher density of 10^{23} cm^{-3}. For this comparison the excited states with n≥3 were excluded from the calculation while all the states with n=2 were included. The population densities of the different ionization stages peak at a temperature of around 2.5 eV, 7 eV, 10 eV and 40 eV for NII, NIII, NIV and NV respectively. At any temperature not more than two neighboring ionization states are populated to a significant degree. According to the results from the Saha equation the densities would peak at much lower temperatures. In this case at a temperature above 5 eV, NIII would not be present in the plasma

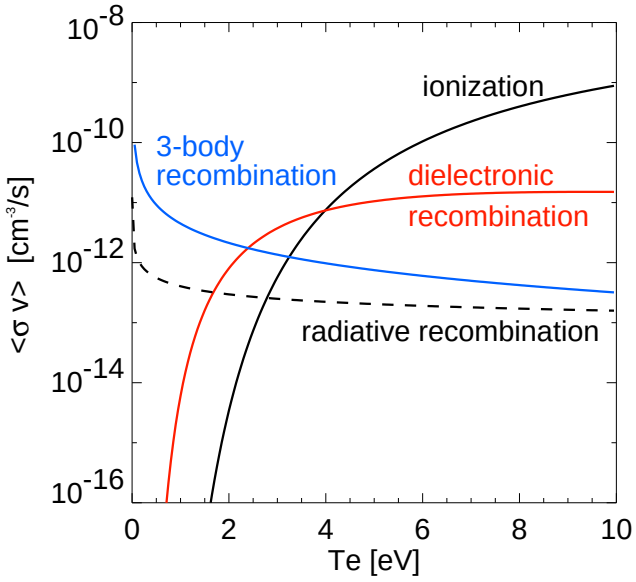

Figure 4.45: Comparison of the rate coefficients for ionization, three-body recombination as well as dielectronic and radiative recombination for transitions from the NII ground state at an electron density of $5 \cdot 10^{17}\ cm^{-3}$.

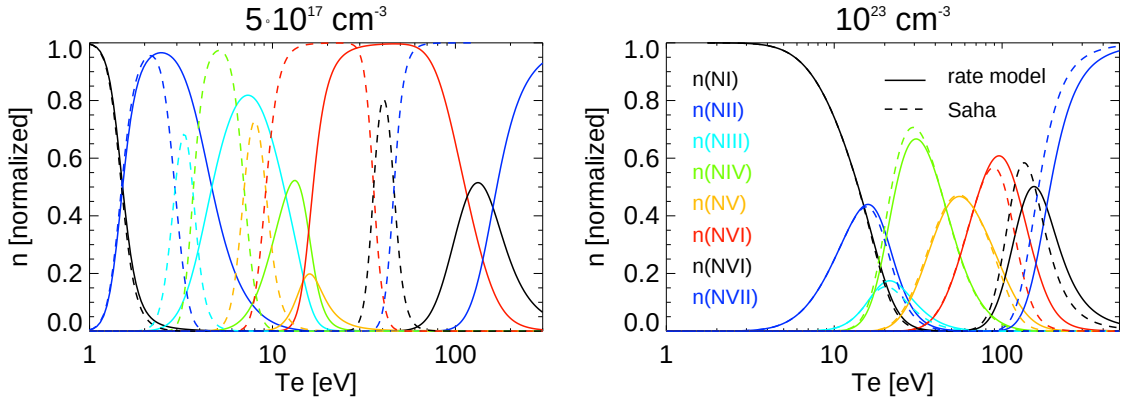

Figure 4.46: Comparison of the ground level densities calculated with the rate model (solid lines) and the Saha equation (dashed lines) for a density of $5 \cdot 10^{17}\ cm^{-3}$ (left) and $10^{23}\ cm^{-3}$ (right). For this calculation all n=2 states were included but no n≥3 states.

any more. Only at higher densities the results from the rate model and the Saha equation agree. At a density of $10^{23}\ cm^{-3}$ both methods agree within 10 percent at temperatures below 100 eV so the plasma is in the Saha regime. Beginning with $10^{24}\ cm^{-3}$ both models agree better than 1 % up to temperatures of 500 eV. This shows that the Saha equation can not be used in the plasmas encountered in the channel experiments in Berkeley and at GSI and that a rate model is crucial for an accurate temperature determination.

The result for the whole system of linear equations including the excited states (n=3) is plotted in figure 4.47 for an electron density of $5 \cdot 10^{17}\ cm^{-3}$. The peak density of the excited state is typically three to four orders of magnitude smaller than the density of the ground state. For a two-level system this ratio can also be estimated analytically by

$$\frac{n(n=3)}{n(n=2)} = n_e \cdot \frac{C_{up}}{n_e \cdot C_{down} + A}. \tag{4.54}$$

The population of the excited state increases with the electron density. The peak densities of the excited states are shifted relative to the maxima of the ground levels towards higher temperatures by a few eV.

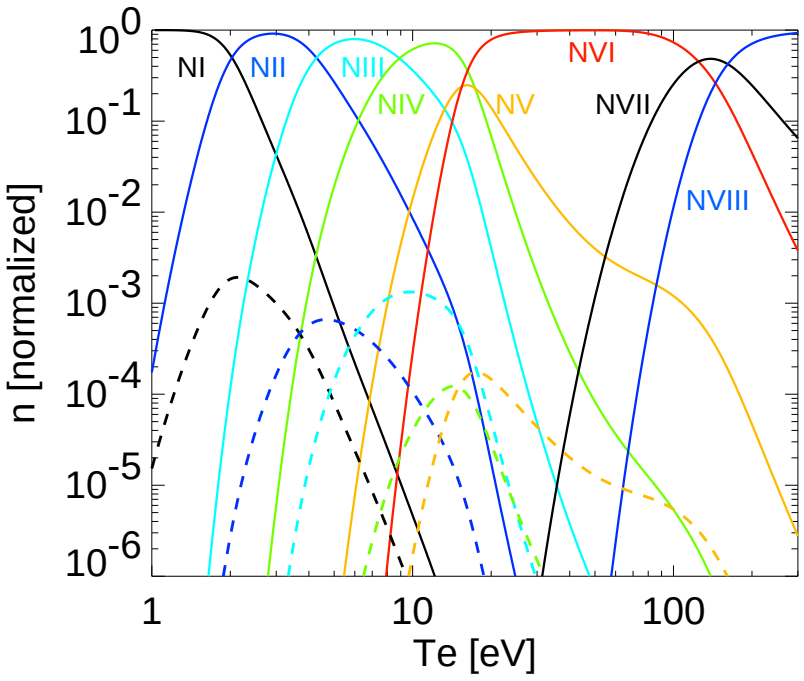

Figure 4.47: Population densities of the ground levels (solid lines) and the first excited states (dashed lines) for NI to NVIII as calculated with the rate model for an electron density of $5 \cdot 10^{17}\ cm^{-3}$.

4.2.4 Determination of the electron temperature

Once the densities of the first excited levels $n_3(NI)$, $n_3(NII)$, ... are known a theoretical spectrum can be constructed

$$\begin{aligned} I(\lambda) = \quad & \sum_{i,j} n_3(NI) A_{ji} \cdot \frac{g_j}{g_3} \cdot exp\left(\frac{-(E_j - E_0^I)}{kT_e}\right) \Phi_j + \\ & + \sum_{k,l} n_3(NII) A_{lk} \cdot \frac{g_l}{g_3} \cdot exp\left(\frac{-(E_l - E_0^I)}{kT_e}\right) \Phi_l \ + \\ & \vdots \end{aligned} \tag{4.55}$$

where the sum has to be performed over all possible transitions $j \rightarrow i$ each corresponding to a spectral line. Hereby g_j is the statistical weight of the upper level, g_3 the statistical weight of the average excited state (table 4.3) and A_{ji} the spontaneous transition probability for this spectral line. The line shape is expressed in ϕ. Since the nitrogen lines are dominated by the apparatus broadening, ϕ has a Lorentz shape:

$$\phi_j(\omega) = \frac{\sigma^2}{4(\lambda - \lambda_{c,j})^2 + \sigma^2} \ , \tag{4.56}$$

where σ is the line width given by the apparatus width and $\lambda_{c,j}$ the central wavelength of the line j. For the theoretical spectrum a database containing the central wavelength λ_c, the

spontaneous transition probability A_{ji}, the statistical weight $g_j = 2J + 1$ and the energy of the upper level E_j for 13 NI lines, 87 NII lines, 57 NIII lines and 25 NIV lines in the relevant spectral range was used [Kur95]. The exponential factor in equation 4.55 accounts for the energy difference between the individual levels in n=3. The minimum energy E_0^X of all the levels in n=3 was selected for each ionization stage X from the same database [Kur95] including around 900 lines in the entire spectral range ($E_0^I = 10.3266\ eV$, $E_0^{II} = 18.4636\ eV$, $E_0^{III} = 27.4398\ eV$ and $E_0^{IV} = 64.3038\ eV$). Both normalized experimental and theoretical spectrum are compared for different temperatures until the best agreement is found. For a determination of the temperature it is important to concentrate on spectra which contains lines of two different ionization states, in this case NII and NIII. Figure 4.48 shows two different experimental spectra of a 44 kA discharge in 10 mbar at different times together with the fitted theoretical spectra. At early

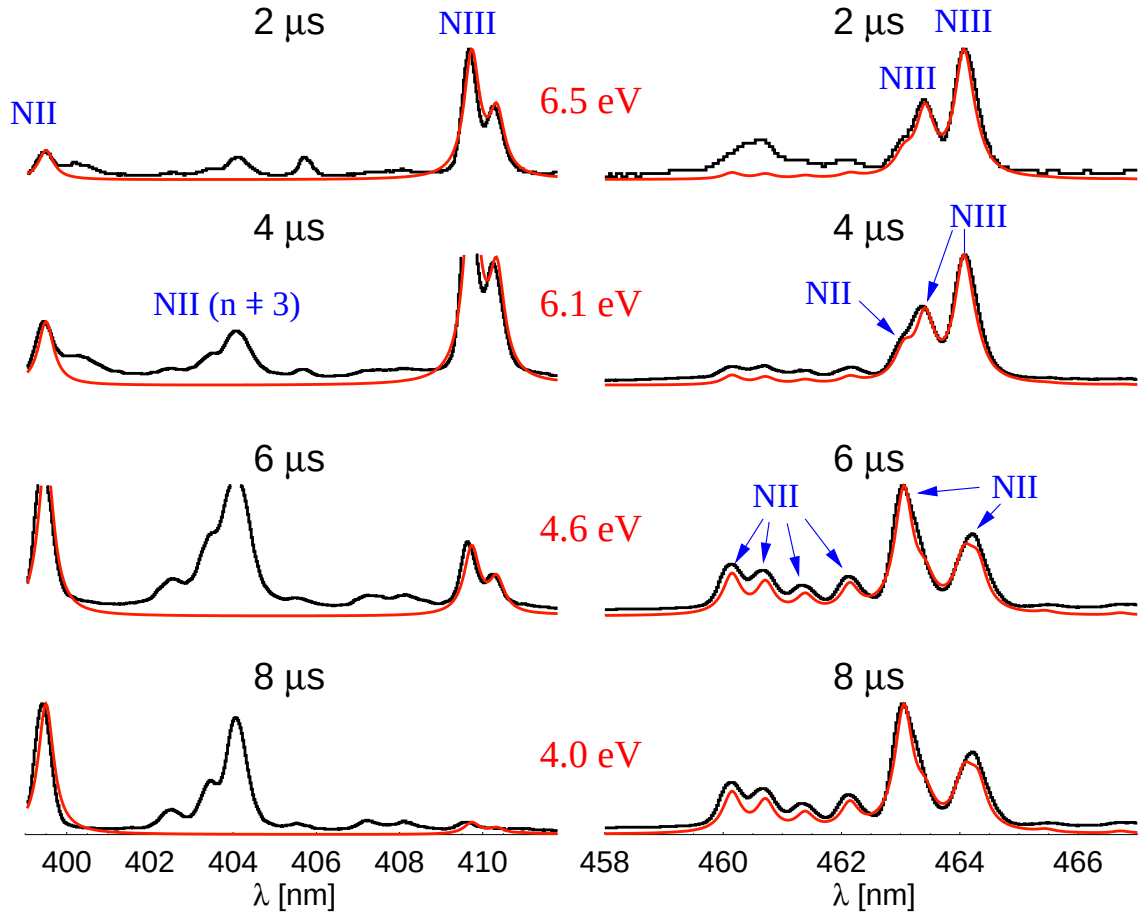

Figure 4.48: Experimental spectra for different times (black) and the fitted theoretical spectrum (red). The temperature was chosen to fit the measurement in the best possible way.

times when the temperature is high the NIII lines dominate. As the temperature drops their intensity decreases while NII lines take over. The theoretical spectrum fits the measurement well throughout the entire investigated spectral range. Lines from other excited levels which are not included in the model (e.g. the NII line at 404 nm in figure 4.48) can not be compared with the measurement. The small differences between experiment and theory which can be seen for example at the NII lines around 461 nm in figure 4.48 can by explained by such lines which are not included in the model. Also the used line data [Kur95] is only precise within a few percent. Test with another database [Wie96] could only poorly reproduce the measurements.

Within the model assumptions described above the temperature can be determined with an accuracy better than 0.1 eV. However, systematic errors in the calculated population densities

due to simplifications in the model or poor rate coefficients are not included in this small error. The time evolution of the plasma temperature for a set of different discharge parameters is summarized in figure 4.49. For each time the spectra of the discharges with different parameters were fitted by the model to obtain the temperature. The discharge current and the channel

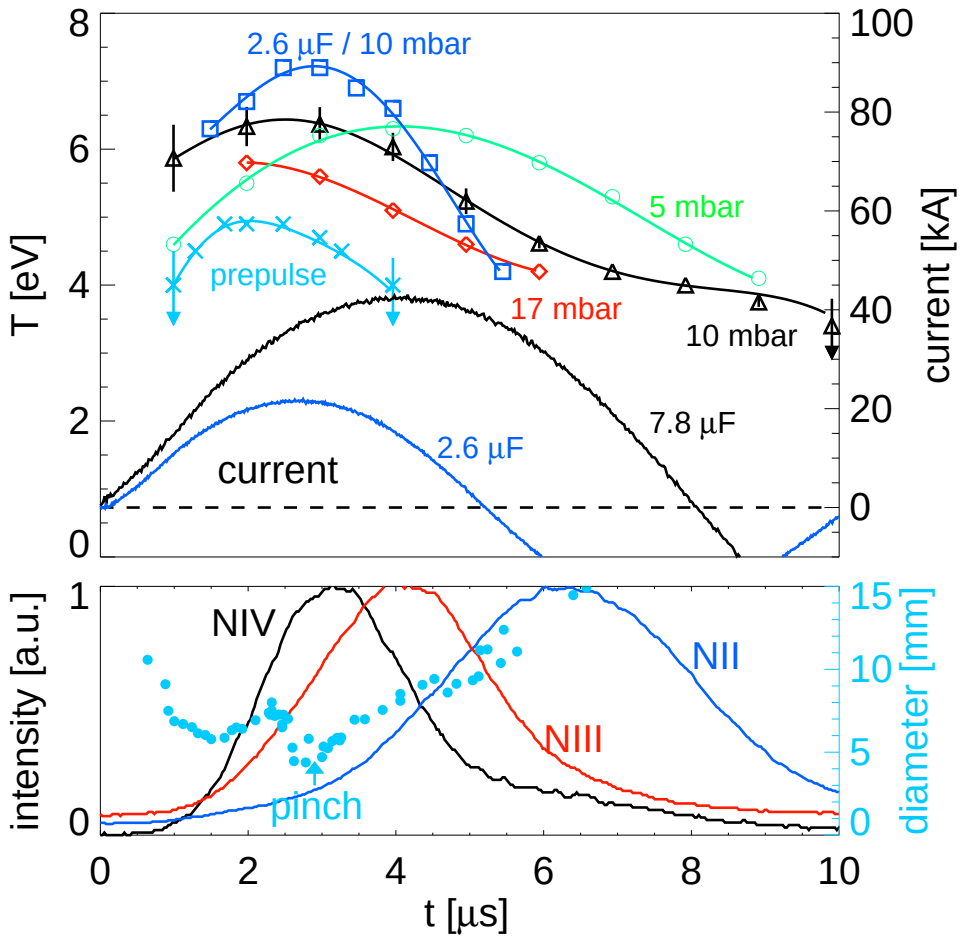

Figure 4.49: Time evolution of electron temperature for a 44 kA discharge in 5 mbar (green), 10 mbar (black) and 17 mbar (red), a 20 kA discharge in 10 mbar (dark blue) and a 15 kV prepulse in 15 mbar (light blue). For each time the experimental spectra were fitted by the model to obtain the temperature. The discharge current of a 20 kA and a 44 kA discharge is shown as time reference. The lower graph shows the time evolution of the line intensity of NII, NIII and NIV as well as the channel diameter in a 44 kA discharge in 10 mbar.

diameter are ploted as reference. Figure 4.49 also compares the time evolution of the line emission of the NII line at 444.7 nm ($2p3d-2p3p$), the NIII line at 451.8 nm ($2s2p(^3P^0)3p-2s2p(^3P^0)3s$) and the NIV line at 346 nm ($2p3p-2p3s$) in a 44 kA / 10 mbar discharge. The temperature in a 44 kA discharge in 10 mbar ammonia ranges from around 4 eV at late times up to a maximum of 6.5 eV at a time of 3 μs. This is in agreement with observations of NIV lines which peak at this time for this discharge parameters. Although the maximum discharge current is reached later at 4 μs, the pinch occurs at 3 μs and the maximum current density and therefore temperature is reached at that time. The maximum temperature in 5 mbar discharges occurs later at around 4 μs, while the temperature in a 17 mbar discharge peaks earlier than 3 μs. The highest temperature is observed for a lower discharge current of 20 kA, reaching a maximum of more than 7 eV. Also the prepulse discharge with currents around 1 kA produces temperatures

as high as 5 eV. At temperatures below 4 eV the NIII lines disappear and the temperature can not be determined accurately. No NI lines were measured in the investigated spectral range which could be used together with NII lines to determine temperatures below 4 eV at later times. Only two NIV lines at around 346 nm were recorded. Since in the spectral vicinity no NIII lines are present it can not be used to determine the temperature from the NII/NIII lines.

Chapter 5

Intersecting discharge channels

A channel based reactor with two sided target illumination requires two converging discharges and some current return path in order to provide a focusing magnetic field for both beams propagating from opposite sides towards the target (figure 2.3). The feasibility of producing multiple intersecting channels has already been demonstrated in the seventies by laser-induced, aerosol-initiated air-breakdown guided V-shaped discharges [Kop79]. However, due to the required high gas pressure and the poor stability of the channels this method is not suited for a reactor application. Multiple channel experiments were also performed with exploding wires [Oza83]. In those experiments a 30 cm long center channel and two current return paths of 10 cm length were initiated, reaching discharge currents of up to 40 kA. In an ion-beam transport experiment a 14 kA / 1.1 MeV proton beam from the Reiden IV pulsed-power machine was transported through the center channel with high efficiency [Oza85]. Experiments in Berkeley with UV-laser initiated channels produced two converging discharges from opposite sides towards a brass ball target in the center of the discharge chamber connected by one or two metallic rods as current return paths towards ground [Vel98, Fes97, Vel96]. These experiments demonstrated a very stable interaction with the target in a symmetric arrangement with a two-sided return path but produced unstable channels with a single sided brass rod return path at 90^o to the laser initiated channels.

In experiments at GSI, intersecting, stable discharges were initiated for the first time by two crossing laser beams without any other guiding structures at pressures of only a few mbar. Two converging channels with lengths of 29 cm and 21 cm together with two 30 cm long current return channels were produced. The discharges are initiated by CO_2 laser gas heating, causing a rarefaction of ammonia gas. The reduced density of the laser heated gas guides the channels along the laser path and around the 90^o angles. In this way it was possible to produce L,T and X-shaped, free-standing discharges with a total length of 110 cm.

5.1 Experimental setup

The discharges are initiated in the same cylindrical chamber which was used for the experiments with straight channels (see chapter 3.1). Four stainless steel electrodes are mounted on opposite sides, insulated from the chamber by plexiglass flanges. Two cathodes are placed at the symmetry axis of the chamber while two anodes are oriented perpendicular, one at the bottom and one at the top. All four electrodes are arranged in the same plane, indicating the shape of a cross (figure 5.1). For the ion-beam transport experiments, the whole setup was integrated into the Z4 beamline of the UNILAC-accelerator. The cathodes were kept on ground potential since they are in direct contact to the beamline. The laser is focused by a f=1.5 m concave mirror before it is split by a 50/50 beam splitter into two beams of equal intensity. Both beams enter the discharge chamber through ZnSe windows and 15 mm bore holes in the upper anode and the left cathode. The two laser beams meet in the center of the chamber where also the foci

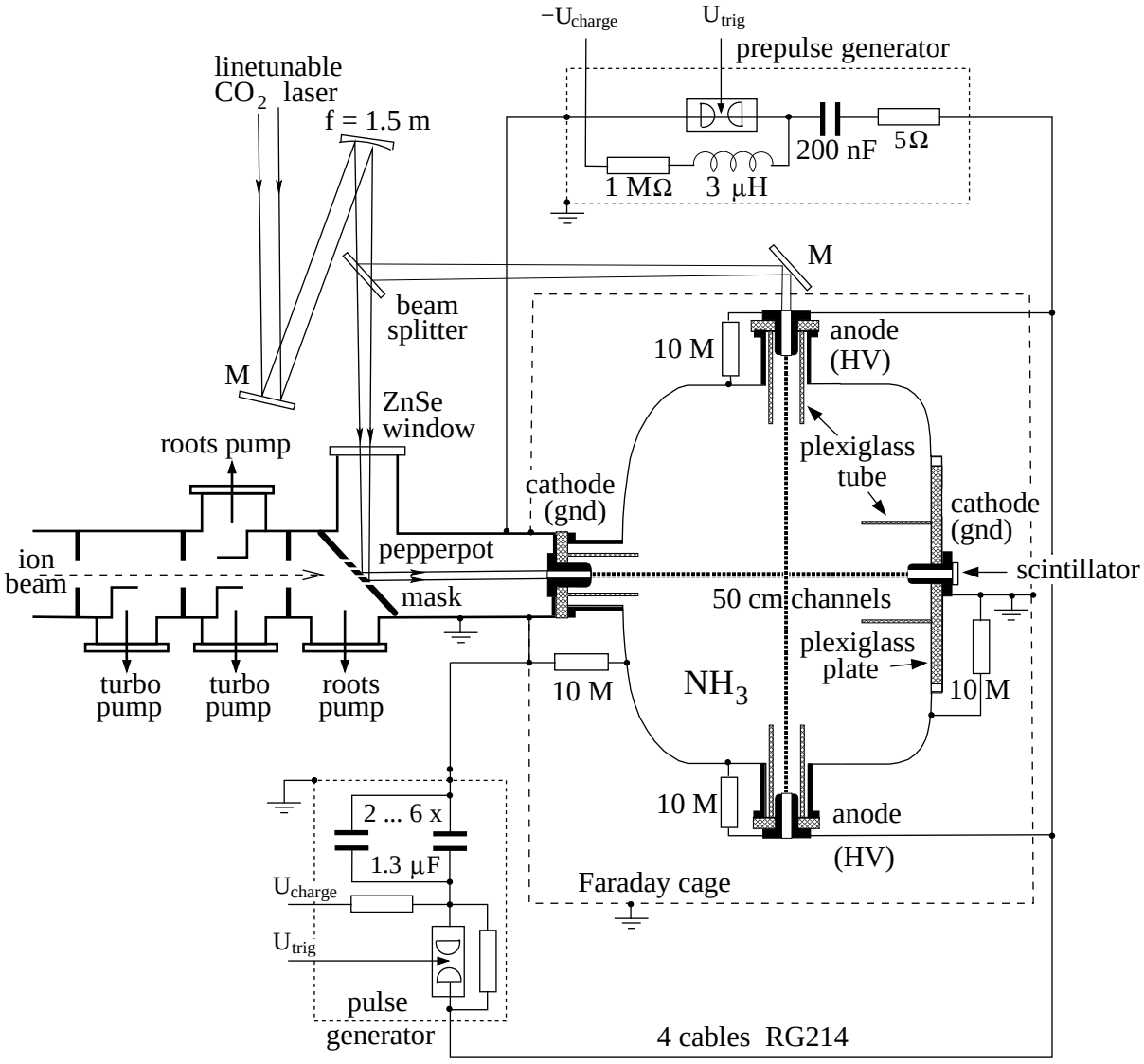

Figure 5.1: Experimental setup for the experiments on intersecting channels.

are located, forming the shape of a cross. The maximum energy density was around 1 J/cm in each beam. Four plexiglass tubes extend 10 cm from the electrodes into the chamber to prevent breakdown directly to the wall. A differential pumping section consisting of several roots and turbo pumps reduces the pressure from initially a few mbar inside the chamber down to the 10^{-6} mbar environment of the UNILAC linear accelerator. A Molybdenum pepperpot mask which is also used as a final bending mirror for one of the two laser beams prepares 11 ion beamlets of the whole UNILAC beam forming a cross. The 1 mm diameter holes in the mask reduce the laser energy reflected horizontally into the chamber by roughly 20 percent. A fast plastic scintillator mounted in a 15 mm diameter hole in the back side cathode together with a fast shutter camera is used to analyze the ion optical properties of the discharge channels. The main-pulse generator is connected by two RG214 cables of 3 m length to each of the anodes. Two 10 cm wide and 70 cm long copper bands connect the two cathodes. The ground of the HV-cables is connected to these copper bands in a symmetric way in the middle between both cathodes. The prepulse capacitor was connected with one cable each to the upper and the lower anode from the 5 Ω damping resistor. The ground of both cables was directly connected to the right cathode.

5.2 Creation of intersecting discharges

The capability to control the bending of discharges with the laser was first tested by the low energy prepulse. A series of fast shutter images of a 7 kV prepulse discharge (4.9 J) in 5 mbar ammonia recorded at different times with an exposure time of 100 ns is shown in figure 5.2. The discharge was triggered 15 μs after the laser pulse. The initial footprints of the two intersecting laser beams are marked by the dashed lines. The pictures show a L-shaped discharge with

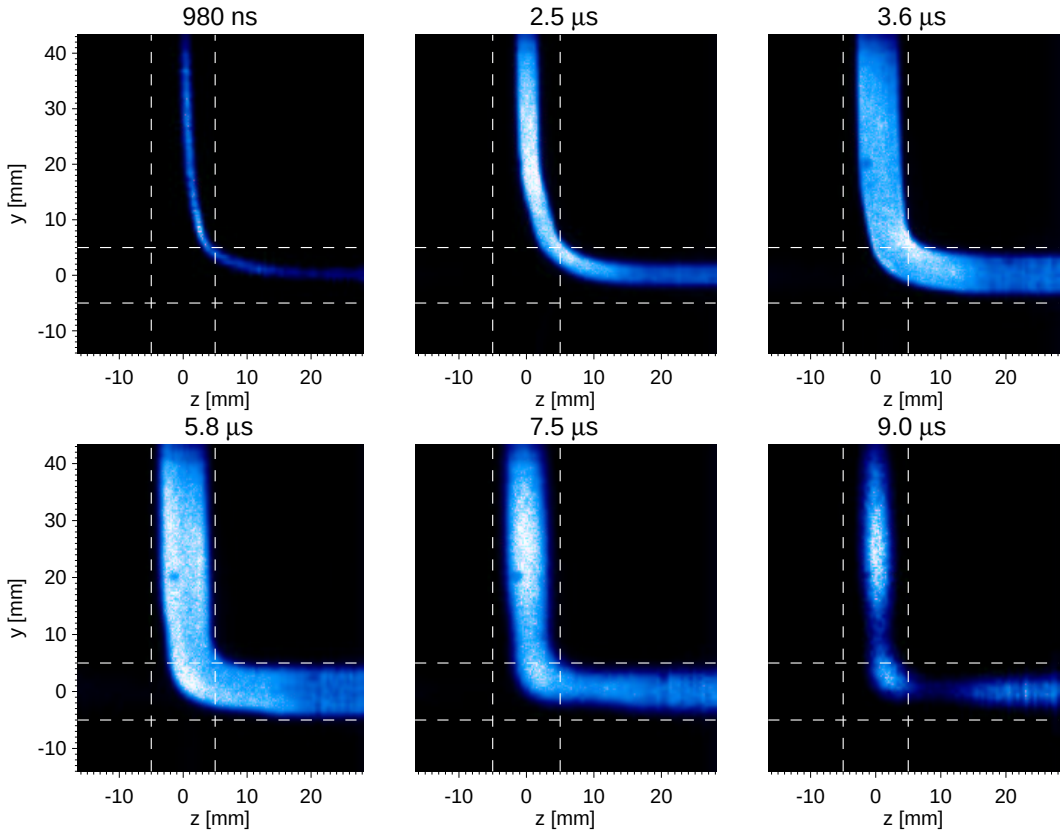

Figure 5.2: A series fast shutter camera images of an L-shaped 7 kV predischarge in 5 mbar ammonia.

two straight channel sections and a bending radius not bigger than 10 mm at the intersection point. The discharge does not break through the unheated gas but follows at all times the laser beam, even close to the intersection point. The reduced gas density along the laser paths offers the better conditions for a gas breakdown even though the length is bigger. The product of length and gas density of the two perpendicular channel sections is comparable to the product of the diagonal if the density along the laser beams is reduced by $\sqrt{2}$ corresponding to a density reduction of 30 percent. The laser energy is not absorbed homogeneously along the laser path. The absorption along the gas cell is given by $\partial I/\partial z \sim \sigma \cdot I$ where I is the laser energy and σ the absorption cross section. Apart from saturation effects this leads to an exponential decrease of deposited energy along the channel. The gas near the left cathode and the upper anode is heated stronger causing a bigger gas rarefaction and prefered conditions for the discharge. Apart from this, the discharge chamber is not symmetric along the ion beam axis (left - right). The bending radius of the chamber wall is bigger on the left side than an the right (see figure 5.1). The distance from the left anode to the intersection point of the crossed channels (29 cm) is bigger than the distance to the right anode (21 cm). For these reasons all the current flows only through the upper and right channel sections forming a L-channel. The reduced gas rarefaction on the lower side of the discharge chamber can be compensated by a shorter distance of the lower anode

from the chamber center. This was realized by a 1 cm diameter stainless steel rod of adjustable length, connected to the bottom anode, which reduces the initially 30 cm distance between the electrode and the intersection point. The effect of such a rod is shown in figure 5.3 for a prepulse at 5 mbar. Without the rod the current flows entirely through the upper half of the cross. A rod with only 1 cm length already draws a visible fraction of the current towards the bottom anode. A 3 cm long rod yields in this conditions an almost perfect balance between the upper and the lower channel section. The balance depends very sensitive on the absorption and thus on the gas

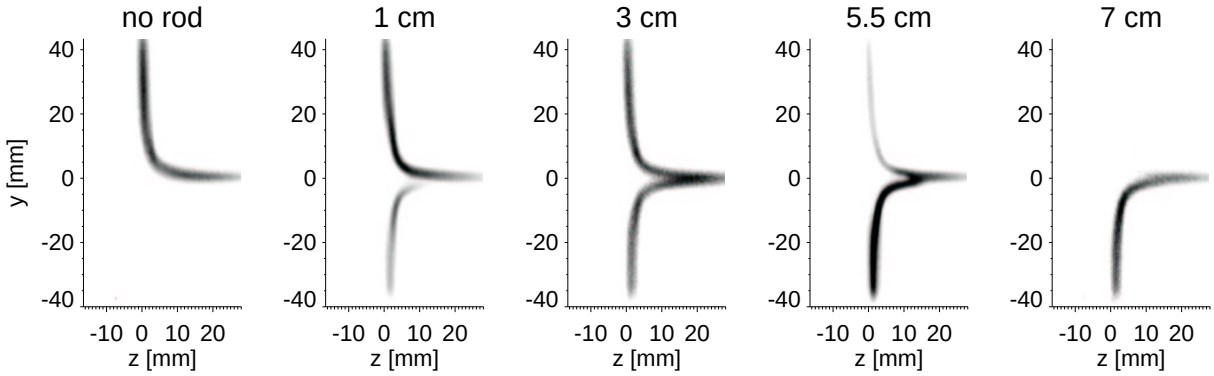

Figure 5.3: Prepulse discharges imaged each time at 2 μs after the breakdown but with a metal rod of different length extending the lower cathode.

pressure and the laser wavelength. At a higher gas pressure the difference between laser heating near the top and the bottom anode is stronger emphasized. A balanced system creating a T-channel at a certain pressure will create an L upwards at higher pressures and an L downwards at lower pressures. A pressure difference of only 0.5 mbar was in this experiment sufficient to compensate a rod length of 1 cm. For UV or ion beam initiated intersecting channels where the initial conditions are considerably more symmetric than in our case the channel balancing should be much easier. The experiments performed in Berkeley [Fes97, Vel96] with metal rods replacing the second laser beam produced two converging channels from opposite sides each time. However, a current imbalance due to an impedance imbalance was also observed there. After some microseconds a T-shaped discharge will transform into a L when the current return channel with the bigger initial current flow takes over all the current and the other channel dies off. With a proper balancing the duration of the phase where two current return paths can exist at the same time can be increased to almost the duration of the discharge. A pinhole camera was used to maximize the field of view through the narrow windows in the discharge chamber. In this way the discharge could be imaged over 25 cm, showing very straight channels at some distance from the intersection point (figure 5.4). X-shaped prepulse discharges or L-channels from left towards up or down were also created occasionally at slightly higher pressures of 8 to 10 mbar. However, the unsymmetric chamber geometry and laser absorption did not allow a reproducible initiation of X-shaped channels.

Also the high current discharge at 45 kA follows the laser footprint. However, in this case all discharges formed a T-channel. Extending metal rods at the electrodes of several cm length do not change this behaviour. Also with a preceding L-shaped low current discharge the following high current discharge forms the shape of a T. A series of fast shutter photographs of a T-shaped main discharge is shown in figure 5.5. The temporal evolution shows two separate L-channels at early times with a bending radius of a few mm, small enough to stay within the laser footprint. After 2 μs the two channels merge. The discharges are surprisingly stable up to late times after the current maximum. A wider view of the high current discharges recorded with the pinhole camera shows that apart from the intersection point the separate channel sections are straight and perpendicular (figure 5.6). Due to the 90^o angle the two current return channels experience

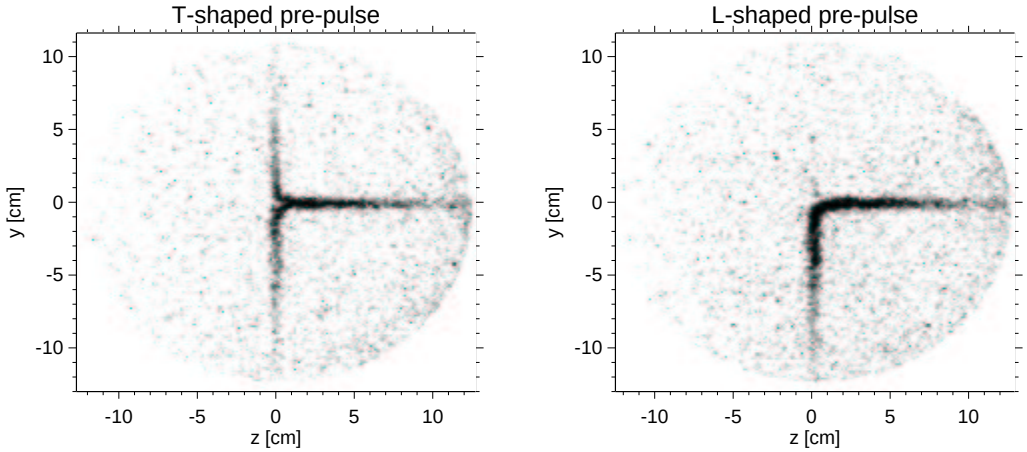

Figure 5.4: Pinhole camera images of a T-shaped and an L-shaped prepulse discharge. The exposure time was 1 μs.

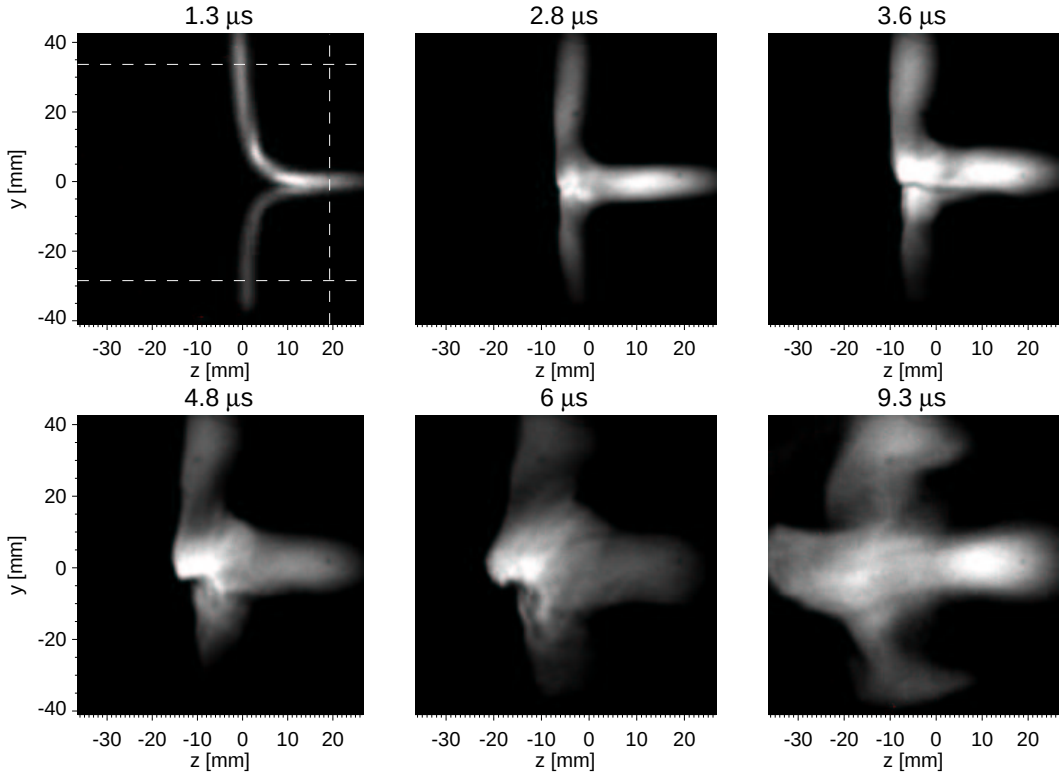

Figure 5.5: A series of fast shutter pictures of a 45 kA T-shaped discharge in 5 mbar. The exposure time was 50 ns.

the azimuthal magnetic field of the center channel. The higher magnetic pressure inside the bending section pushes them towards the left side (figure 5.7) with a force which is decreasing with the distance y from the center of the intersection point. The center channel stays fixed since the opposite currents from the return paths compensate. No X-shaped 40 kA main-discharges could be produced in this experiment due to the unsymmetric chamber geometry (distance from left cathode to intersection point (IP) 29 cm, distance from right cathode to IP 21 cm).

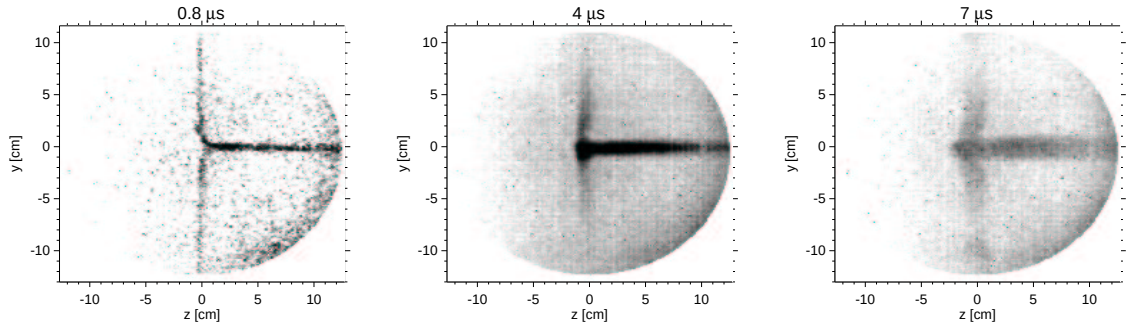

Figure 5.6: Pinhole camera images of 45 kA discharge in 5 mbar ammonia at different times. The exposure time was 1 μs. The picture in the middle shows the discharge shortly after the current maximum. Close to the intersection point the higher magnetic pressure inside the bend pushes the vertical channels towards the left side.

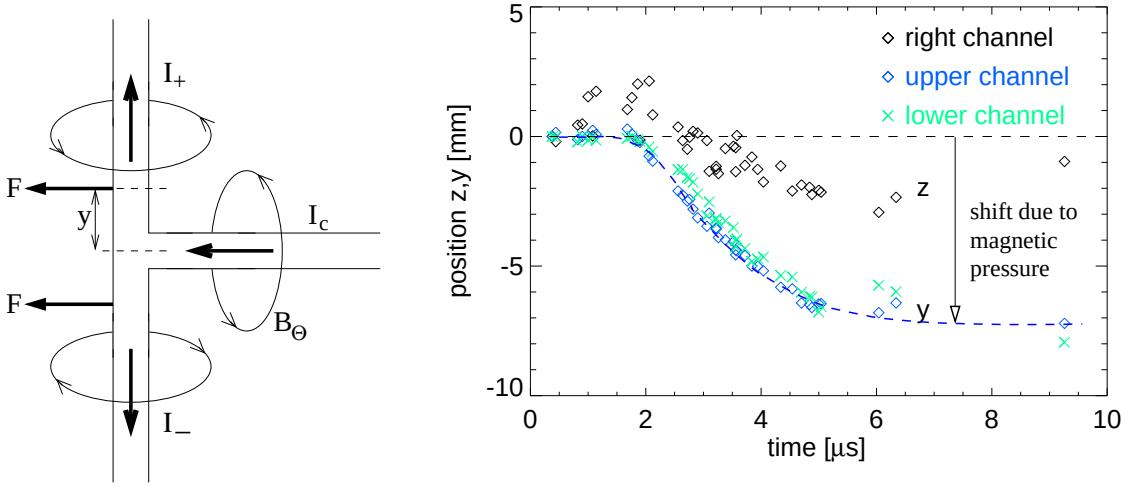

Figure 5.7: Magnetic forces at the intersection point cause a shift of the upper and lower channels towards the left side around the intersection point.

5.3 Ion-beam transport experiments in intersecting channels

A 11.4 AMeV $^{58}Ni^{+12}$ beam from the UNILAC linear accelerator was used to probe the ion-optical properties of the discharge and thus the current density distribution. For this purpose 11 separate 1 mm diameter beamlets are selected in a cross shaped configuration from the whole beam by a Molybdenum pepperpot mask. The holes are distributed equally at the x and y axis with a distance from hole to hole of 2 mm. The central hole is missing and one hole at an unsymmetric position at 45 degree is added. The azimuthal magnetic field bends these beamlets depending on their radial position from the discharge axis as described in chapter 2.3. A T-shaped discharge was used to investigate the effect of the intersection point on the overall ion optical properties of the discharge (figure 5.8). A fast plastic scintillator (Bicron BC-400) was used to visualize the ion distribution behind the chamber. A total ion-beam current of around 50 μA before the pepperpot mask allowed an exposure time as low as 30 ns with an image intensified camera at almost full gain. Both ion - and laser beam as well as the center of the pepperpot cross are aligned to the symmetry axis of the discharge chamber. However, due to the large laser beam size an uncertainty of a few mm is typical. If the discharge axis is not aligned to the center of the pepperpot cross the different beamlets will oscillate around the actual discharge axis, making an interpretation rather complex (figure 5.9). This is an experimental evidence

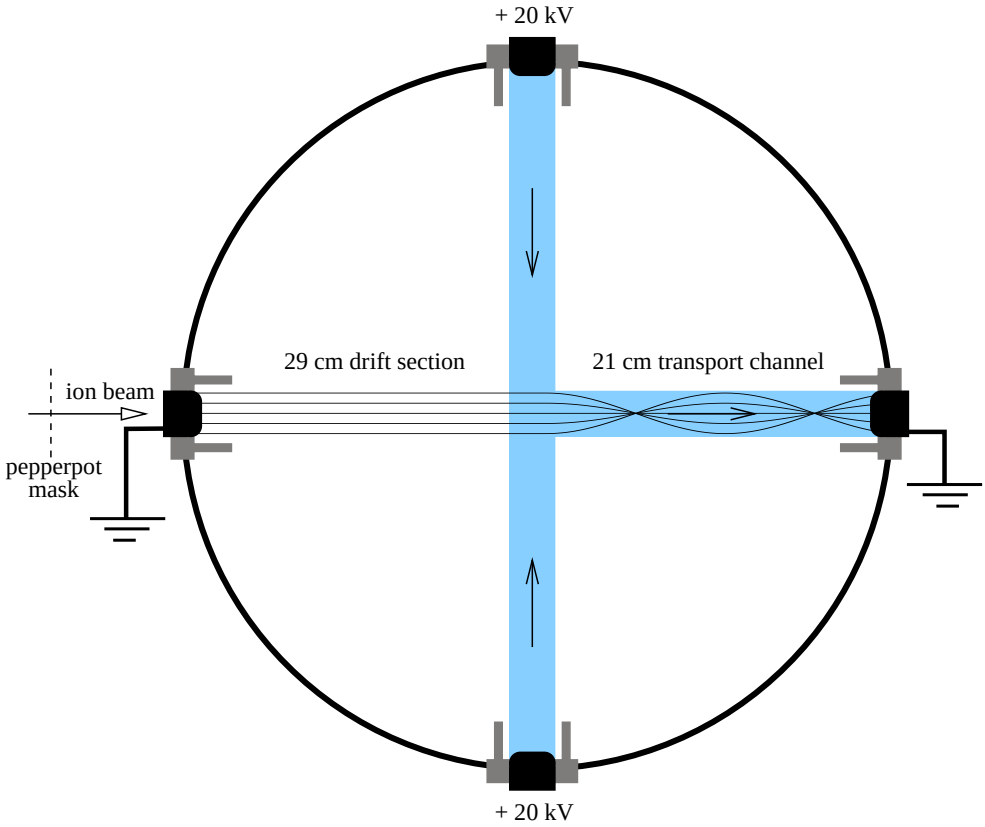

Figure 5.8: Investigation of the ion optical properties of the central channel of a T-shaped discharge.

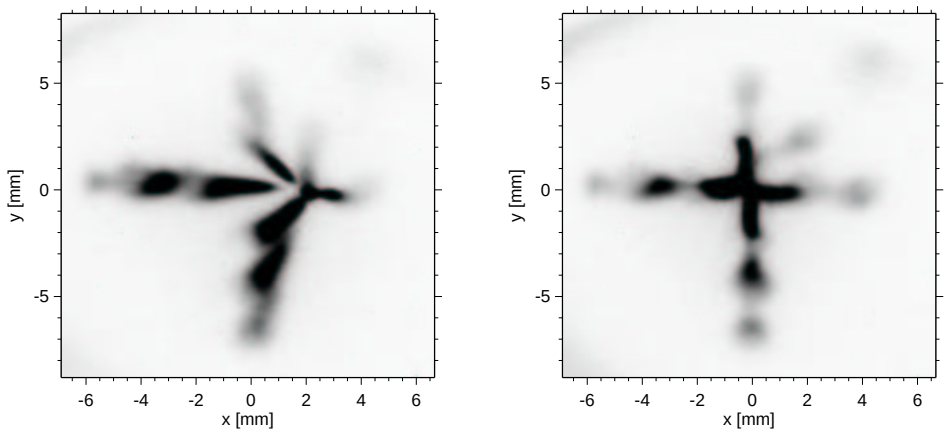

Figure 5.9: Fast shutter photographs of the scintillator light emission caused by the heavy ion beam. The exposure time was 1 μs to image the trend of the beamlet motion towards the discharge axis (perpendicular to the paper plane). The left picture shows the result for a discharge axis different from the ion beam axis (center of the pepperpot cross), the right picture shows the result after the laser beam was aligned to the center of the cross.

that the discharge follows directly the laser beam in a very sensitive way. A perfect alignment of the laser beam to the center of the pepperpot mask was not possible in this setup because the pepperpot mask which is used as final bending mirror is fixed. The laser-beam alignment is done only with the last focusing mirror. Therefore the angle and the position of the laser beam change always at the same time.

A series of fast shutter photographs of the scintillator light emission with an exposure time of 30 ns is shown in figure 5.10 together with the discharge current. The picture on the left side shows an image of the pepperpot cross without a discharge. During the first microsecond the

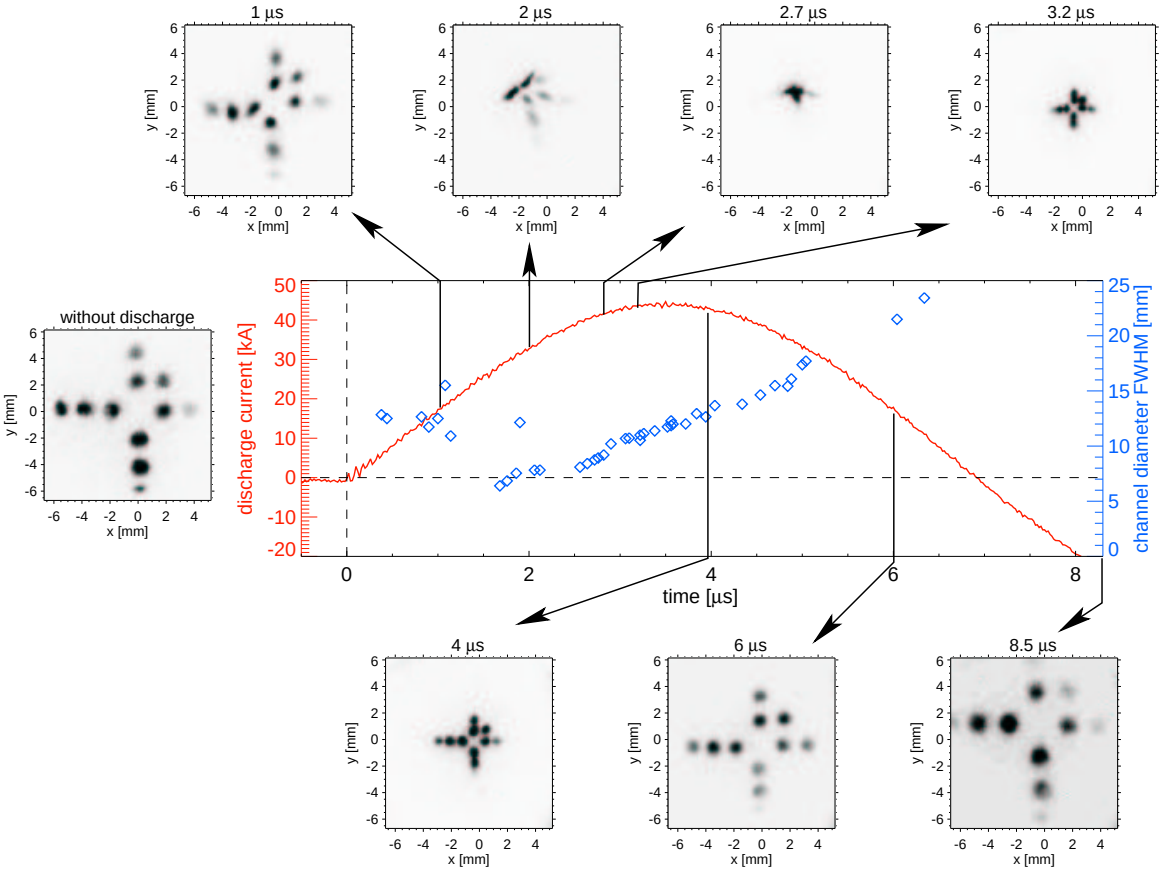

Figure 5.10: Photographs of the scintillator light emission for different times during the discharge as well as the discharge current. The exposure time was 30 ns each time. Only one focus can be observed at around 2.7 μs.

discharge-current density distribution is so small, that the beamlets are only slightly deflected towards the discharge axis. At 2 μs, when the discharge pinches, the image of the cross is distorted due to an inhomogeneous current density distribution. The same behaviour was observed in straight discharges [Pen02]. The smallest focus is reached at around 2.7 μs. The cross is never completely reversed as it is the case for a normal 50 cm long z-discharge with the same discharge conditions [Tau01]. The focusing strength slowly decreases in time after 2.7 μs when the discharge current decreases and the channel diameter increases. At late times the reversed current leads to a defocusing of the beamlets resulting in a bigger image of the pepperpot cross (bottom right picture at 8.5 μs). The constant ratio of the distances between different beamlets on the scintillator is an indication that the current density distribution is approximately constant at all times apart from the pinch time. While the size of the cross is changing, the shape remains the same. This is a feature of an ideal lens with a linear magnetic field.

The Betz formula (equation 2.12) gives a charge state of 26 for the 11.4 AMeV ^{58}Ni beam. Figure 5.11 shows the calculated ion trajectories for the 21 cm long channel section assuming a current of 40 kA and a homogeneous current density distribution of 10 mm radius, which are the measured discharge parameters for 2.7 μs. The size of the current carrying channel was considered to be comparable to the size of the light emission profile, measured at the base, which is roughly twice as big as the FWHM. With this parameters the beam would be transported a

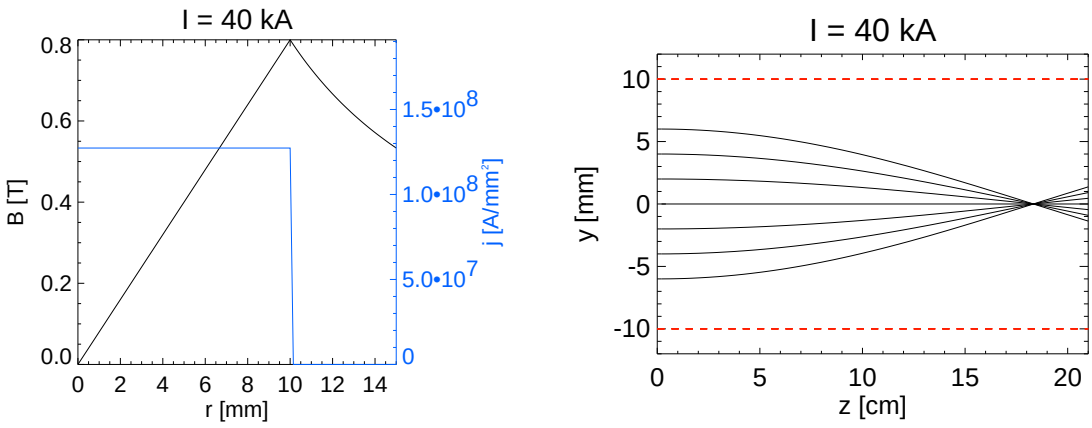

Figure 5.11: Magnetic field and ion beam trajectories for the used Ni beam transported through a 40 kA channel with a homogeneous current density distribution and a diameter of 20 mm, the size of the channel at 2.7 μs (measured at the base).

little more than over a quarter of a betatron oscillation, showing a compressed, inverted image of the pepperpot mask at the scintillator. The observed image of an non-inverted image shortly before the first focus can be explained by a slightly larger channel , a smaller current flow within the channel (30 kA) or the influcence of the intersection point of the discharges, where the channel diameter is considerably bigger and the focusing magnetic field smaller over a length of several cm. The current of 40 kA is measured at a shunt inside the pulse generator and does therefore not necessarily give the current flowing inside the channel. It is possible that a fraction of the total current flows around the insulators directly to the wall. The observed images at the scintallator can be reproduced assuming a maximum current of only 30 kA flowing through the channel with the measured diameter (figure 5.12). The charge state only has a small effect on the ion-beam trajectories. Direct magnetic-field measurements by $\dot{B}$ probes [Pen02] will show if the width of the light emission profile gives a reasonable value for the size of the current density distribution and if all the current flows within the channel.

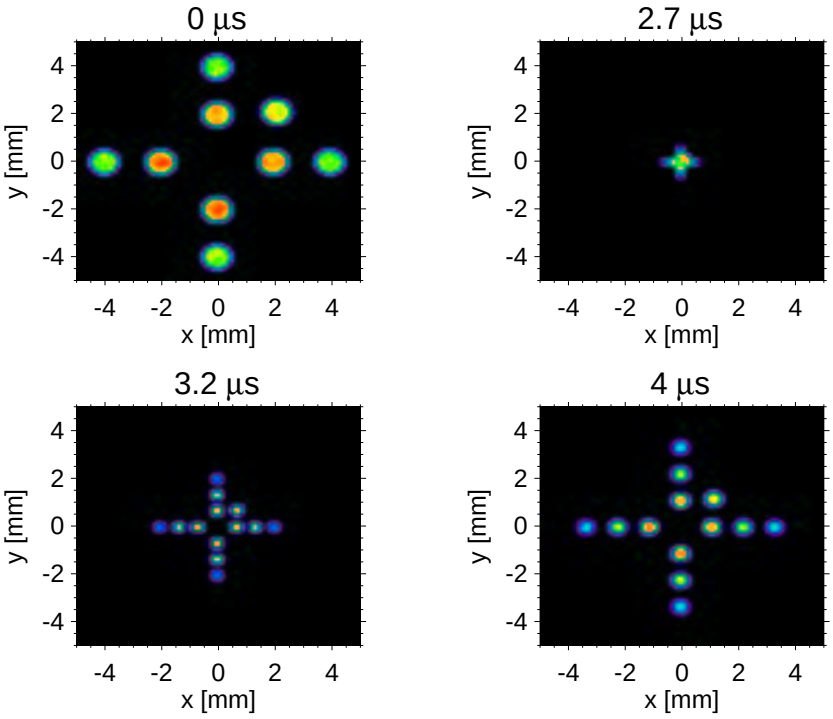

Figure 5.12: Simulated scintillator images for a diameter as measured from the self emission profile but a maximum current of only 30 kA.

Chapter 6

Summary and outlook

Stable plasma channels with a length of half a meter and currents in excess of 50 kA were produced in a metallic discharge chamber by different initiation techniques. In experiments at Berkeley the free-standing discharge channels were guided by a UV-laser, ionizing Benzene molecules by resonant two-photon absorption, which were added to a nitrogen background gas. At GSI, the discharges were guided and stabilized by resonant CO_2-laser gas heating of ammonia gas. The laser wavelength was tuned to a molecular vibration of ammonia to maximize the absorption. In this way the total absorption in the 50 cm long chamber was ranging up to 80 percent at a gas pressure of 15 mbar. Initial gas temperatures around 1000 K lead to the creation of a rarefaction channel which guides the discharge along the laser path. The breakdown and channel evolution can be explained by the formation of this low density channel. Simulations with CYCLOPS indicate a reduction of the gas density on axis by 40 to 80 percent for maximum temperatures of 500 to 1300 K. A reduction of breakdown voltage by more than 40 percent was measured at 15 mbar for a 2 J/cm^2 laser pulse. For a discharge voltage below the breakdown limit the density is too high to lead to an instantaneous breakdown when the capacitor bank is triggered. However, a small current is driven through the heated, rarefied gas causing Joule-heating and an additional gas density reduction. When the density drops below a critical value an electron avalanche occurs. The simulated on-axis gas density evolution in time predicts a distinct minimum 15 μs after the laser pulse. The measured internal discharge delay shows a minimum at the same time, indicating that the discharge delay is determined primarily by the evolution of the gas density. For a discharge voltage above the breakdown limit the avalanche occurs without any delay. In this case discharge trigger delays of a few microseconds up to milliseconds with respect to the laser heating successfully initiate channels, which demonstrates that the rarefaction channel remains at a low density during this time span. The channels are straight, stable and reproducible at least up to the current maximum. The jitter is small compared to the discharge evolution timescale. Breakdown along the metallic discharge chamber wall was not an issue within thousands of discharges. Stable channels were produced with and without an additional low energy prepulse discharge. The minimum channel diameter at pinch time could not be reduced with the prepulse.

Discharge channels at GSI were also successfully initiated by an ion-beam pulse from the UNILAC-linear accelerator. A 2 mm diameter 11.4 AMeV Ni^{+12} ion beam with a current as low as 5 μA in a 20 μs pulse was sufficient to create enough seed electrons to guide free-standing channels in ammonia and argon. Discharges in other gases like Kr and Xe were produced in a consecutive beamtime. These discharges were stable at all times with and without a prepulse. Compared to laser initiated channels the ion-beam channels showed a much smaller fluctuation of the channel position during the discharge. The possibility to initiate discharge channels with the ion beam increases the attractiveness of the channel transport scenario because of the flexibility in choosing the filling gas, the improved channel stability and the simple discharge initiation mechanism.

The discharge plasmas at GSI and Berkeley were investigated by a number of diagnostics. A two-color imaging interferometer was used to measure the electron and neutral gas density in the channels. A comparison of measurements at two wavelengths showed, that within the precision of the measurement, the refractive index inside the plasma column in high-current discharges is determined by the electron density only. Densities between $10^{16}\ cm^{-3}$ and $2 \cdot 10^{18}\ cm^{-3}$ were measured, depending mainly on the initial gas pressure. The temporal evolution of the electron density initially showed an increase up to the time of the current maximum around 4 μs and a subsequent decrease. The density roughly corresponds to half of the electrons contained in the ammonia gas at each pressure. In prepulse discharges the refractive index was within the precision of measurement, dominated by the gas density depression on the channel axis and the radially expanding pressure wave. The on-axis density drops by up to 90 percent in a 15 kV prepulse discharge in 15 mbar. The pressure wave, which expands with a velocity of roughly 1 $mm/\mu s$ shows peak densities around twice the surrounding gas density.

The gas-rarefaction channel created by the laser-heating could be measured by interferometry yielding a gas density reduction of around 50 percent. The axial gas density reaches a minimum around 20 μs and returns to the initial value slowly within milliseconds. This observation is in agreement with CYCLOPS calculations and measurements of the discharge delay.

A gas wall of up to 4 times the initial density was observed in high-current discharges without prepulse. If a prepulse is used 25 μs before the main discharge, no gas wall is observed. This explains partially, why at GSI the discharges are more prone to hydrodynamic instabilities with the prepulse. Expansion velocities of the pressure wave in the prepulse were extensively studied by the schlieren-imaging technique. Calculations of the schlieren-deflection angle due to gas-density gradients are in agreement with experimental estimations.

A Faraday polarimeter, consisting of a cw CO_2-laser and two HgCdTe-detectors based on the half-shadow principle has been set up at Berkeley and was used to measure magnetic fields. Preliminary measurements with reduced laser power and reduced sensitivity indicate that the setup works in principle. The current flow is confined within a cylinder of about 1 cm diameter. Several key-issues for an improvement of the setup, like an increase of laser energy, a better polarization output and a correction of laser deflections, have been identified. A setup with a better laser is expected to measure rotation angles with the design sensitivity of around 0.1^o.

The plasma-self emission has been investigated by means of spectroscopy in the visible range. Measurements of the Stark broadening of hydrogen Balmer lines shows the same temporal evolution of the electron density as the interferometric results. The densities along the line of sight are by a factor of two smaller, which is caused by the integration of the measurement.

To determine temperatures, a rate model for a nitrogen plasma, including electron impact ionization, three-body recombination, radiative recombination, dielectronic recombination, collisional excitation as well as spontaneous transition was developed to calculate the population densities of the ground levels and the first excited state for each ionization state. From this results, experimental spectra could be fitted with synthetic spectra assuming electron temperatures between 4 and 7 eV depending on the discharge parameters. For a high-current discharge in 10 mbar, the highest temperature is reached before the current maximum, around the pinch of the discharge, when the current density peaks. At this time NIV lines reach their highest intensity. As the plasma cools down, the intensity maximum shifts from NIV over NIII to NII lines. The highest temperature reached in a 15 kV prepulse discharge is 5 eV.

The feasibility to produce free-standing, intersecting discharge channels by CO_2-laser initiation was demonstrated at GSI. In this way it was possible to create L, T and X-shaped prepulse-discharges with currents of a few kA at pressures below 10 mbar. At higher pressures only the formation of straight channels was possible. A current imbalance, resulting from an impedance imbalance was observed due to the varying laser-energy absorption along the laser path and the unsymmetric chamber geometry. This current imbalance could be compensated , extending the electrode at the side of higher impedance. If the current was not balanced properly

only L-shaped discharges could be produced or T-discharges, which transformed into L-channels after a few μs. T-shaped high-current discharges with currents in excess of 40 kA were stable for times up to the current maximum and longer with and without a prepulse-discharge. No L-shaped high current discharges could be produced, even by extending an electrode. The same behaviour was observed with a preceding L-shaped prepulse. The higher magnetic pressure close to the interaction point of a T-shaped high current discharge, caused a shift of the two current return channels by up to 7 mm.

Experiments with a 11.4 AMeV $^{58}Ni^{+12}$ beam from the UNILAC-linear accelerator showed that the beam was transported over a quarter of a betatron oscillation through the center channel of a T-shaped discharge. The discharge channels follow very sensitively the laser beams. This was observed with high precision on the scintillator images of the pepperpot-beamlets which oscillate around the discharge axis. When the laser position was shifted, the image on the scintillator was shifting in the same way. The very linear focusing properties of the channel at all times exept the pinch time shows, that the current density distribution is almost homogeneous and that the intersection point does not have a very big effect on the ion-optical properties of the whole channel. Different targets were tested in the intersection point. It was demonstrated, that a current-carrying target can be used to guide the discharge current in the vicinity of the channel intersection point. The target does not disturb the discharge stability and can improve the creation of multiple channels. At discharge conditions where without a target only L-shaped channels were created a target in the intersection point caused the initiation of T or X-channels.

For an application in a reactor, many technical issues like the design of insulators around the electrodes have to be addressed. The work has to be expanded to the investigation of longer channels and pulse durations to fulfill the requirements for inertial-fusion energy. However, important parameters like the channel current and diameter are close to the requirements for a heavy-ion fusion reactor.

In near-term experiments at GSI the channel should be expanded to a length of several meters. The diagnostics developed during this work can be used to build up an experimental data base for the longer channels. Improved diagnostics for high precision experiments must be developed for a better understanding of the channel stability. As part of this could be an interferometer measuring end-on along the channel axis, where the fringe shift is bigger and an Abel-inversion is not required. The discharges must be improved regarding stability of the channel position. This is especially important for diagnostics which measure only at a certain fixed position, like the magnetic field measurements. A key issue might be the interaction of the channel with the electrodes, which has to be analyzed in detail. Experiments should also be performed with smaller laser beam diameters. Ion-beam initiated channels especially in heavy gases like Xe must be studied thoroughly. For discharges in rare gases the current flow has to be concentrated at the channel axis, to maximize the magnetic field. All measurements must be paralleled by extensive simulations with CYCLOPS, which has to be adopted for the ammonia and the rare-gas plasmas. The effect of the gas ionization by the ion beam has to be included for an understanding of the channel initiation and stability. Advanced ion-beam diagnostics, including emittance and beam-current measurements should be performed for a better understanding of the transport properties. The influence of an intense ion beam on the channels must be addressed by simulation codes and by experiments at high intensity proton diodes.

Appendix A

Spectroscopic data

A.1 Fit parameters for the rate coefficients

A.1.1 Fit parameters for radiative and dielectronic recombination

The fit parameters for equations 4.47 and 4.49 are summarized in the following table:

species	A_{rad} $[cm^3 s^{-1}]$	η	A_{di} $[cm^3 s^{-1} K^{3/2}]$	T_0 $[^0K]$	T_1 $[^0K]$	B_{di}
NI	$4.1 \cdot 10^{-13}$	0.608	$5.2 \cdot 10^{-4}$	$1.3 \cdot 10^5$	$4.8 \cdot 10^4$	3.8
NII	$2.2 \cdot 10^{-12}$	0.639	$1.7 \cdot 10^{-3}$	$1.4 \cdot 10^5$	$6.8 \cdot 10^4$	4.1
NIII	$5.0 \cdot 10^{-12}$	0.676	$1.2 \cdot 10^{-2}$	$1.8 \cdot 10^5$	$3.8 \cdot 10^5$	1.4
NIV	$6.5 \cdot 10^{-12}$	0.743	$5.5 \cdot 10^{-3}$	$1.1 \cdot 10^5$	$5.9 \cdot 10^5$	3.0
NV	$1.5 \cdot 10^{-11}$	0.850	$7.6 \cdot 10^{-2}$	$4.6 \cdot 10^6$	$7.2 \cdot 10^5$	0.2
NVI	$2.9 \cdot 10^{-11}$	0.750	$6.6 \cdot 10^{-2}$	$5.4 \cdot 10^6$	$9.8 \cdot 10^5$	0.2

Table A.1: Fit parameters for radiative and dielectronic recombination [Ald73].

A.1.2 Quantum mechanical calculation of radiative recombination rates

Rate coefficients have alternatively been fitted into analytical form based on the quantum mechanical calculation of photoionization cross sections by F.B. Rosmej [Ros01b]:

$$< v\sigma >= 10^{-8} Z A \sqrt{\beta} \cdot \frac{\beta + D}{\beta + \chi} \qquad [cm^{-3} s^{-1}] \tag{A.1}$$

where

$$\beta = \frac{Z^2 \cdot Ry}{kT_e}.$$

The fitting parameters are summarized in table A.2. For $1/4 \leq \beta \leq 32$ the calculated rate

species	Z	A	χ	D
NVII	7	$1.35 \cdot 10^{-5}$	3.26	0.36
NVI	6	$1.21 \cdot 10^{-5}$	3.76	0.41
NV	5	$1.02 \cdot 10^{-5}$	5.25	0.31
NIV	4	$1.07 \cdot 10^{-5}$	4.58	0.40
NIII	3	$1.25 \cdot 10^{-5}$	2.24	0.14
NII	2	$1.37 \cdot 10^{-5}$	0.727	0.08
NI	1	$1.05 \cdot 10^{-5}$	0.777	1.40

Table A.2: Fit parameters for equation A.1.

coefficient has an accuracy better than 10 % for all ionization states and β.

A.1.3 Electron impact ionization

Quantum mechanical calculations of ionization cross sections have been carried out in the Coulomb - Born - Exchange approximation and corresponding ionization rate coefficients have been fitted into analytical formulas by F.B. Rosmej [Ros01b]:

$$\begin{aligned} Z>1: \qquad <v\sigma> &= \frac{10^{-8}}{Z^3}\cdot\frac{mQ}{2l+1}\sqrt{\beta}\cdot\frac{A}{\beta+\chi}\frac{\beta+1+D}{\beta+1}e^{-E_i/kT_e}, \\ Z=1: \qquad <v\sigma> &= \frac{10^{-8}}{Z^3}\cdot\frac{mQ}{2l+1}\sqrt{\beta}\cdot\frac{A}{\beta+\chi}\frac{\beta+1+D}{\beta+1}\left(\frac{1}{1+\frac{E_i}{kT_e}}\right)^{1/2}e^{-E_i/kT_e} \end{aligned} \quad \text{(A.2)}$$

where

$$\beta = \frac{Z^2\cdot Ry}{kT_e}$$

and E_i is the ionization energy given in table 4.3 on page 72. The fitting parameters for the excited states are summarized in table A.3. For $1/4 \le \beta \le 128$ the calculated rate coefficients have an accuracy better than 10 %. Ionization from the n=2 states have been included with a similar procedure.

Z	A	χ	D	m	Q	l
1	$3.77\cdot10^4$	47.5	0.0	1	1/9	0
2	$1.72\cdot10^4$	11.2	0.0	1	1/9	0
3	$2.70\cdot10^4$	15.9	0.60	1	1/9	0
4	$3.55\cdot10^4$	16.8	0.80	1	1/9	0
5	$4.37\cdot10^4$	17.0	0.90	1	1/9	0

Table A.3: Fit parameters for equation A.2. for the n=3 states of the first five ionization stages.

A.1.4 Collisional excitation rates

Oscillator strength (equation 4.51) and transition probability are related by

$$f(n\to n') = \frac{1}{4.339\cdot10^7\Delta E^2}\frac{g(n)}{g(n')}A(n'\to n). \quad \text{(A.3)}$$

For the Gaunt-factor $p(\beta)$, an analytical expression [Ros01c] was used:

- for neutrals:

$$p(\beta) = \left\{ \begin{array}{ll} 0.27566\cdot\left(\beta-\frac{\beta^2}{4}+\frac{\beta^3}{12}-ln(\beta)-0.57722\right) & \text{if } \beta\le 0.4 \\ 0.066\frac{\sqrt{\beta+2}}{\beta+0.127} & \text{else} \end{array} \right\} \quad \text{(A.4)}$$

- for charged particles:

$$p(\beta) = 0.2757e^{-1.3\beta}\left(\beta-\frac{\beta^2}{4}-ln(\beta)-0.5772\right)+0.2\left(1-e^{-4.5\beta}\right) \quad \text{(A.5)}$$

A.2 Rate equations for a nitrogen plasma

Ground states

$$\begin{aligned}\frac{dn(NI)}{dt} = 0 = & -n(NI)\cdot[I_{I,II} + C_I^{up}] + n(NII)\cdot]T_{II,I} + RR_{II,I} + DR_{II,I}] \\ & + n(NI_{n=3})\cdot[A_I + C_I^{down}] \end{aligned} \tag{A.6}$$

$$\begin{aligned}\frac{dn(NII)}{dt} = 0 = & \, n(NI)\cdot I_{I,II} - n(NII)[T_{II,I} + RR_{II,I} + DR_{II,I} + I_{II,III} + C_{II}^{up}] \\ & + n(NIII)[RR_{III,II} + DR_{III,II} + T_{III,II}] \\ & + n(NI_{n=3})\cdot I_I + n(NII_{n=3})\cdot[A_{II} + C_{II}^{down}] \end{aligned} \tag{A.7}$$

$$\begin{aligned}\frac{dn(NIII)}{dt} = 0 = & -n(NIII)[T_{III,II} + DR_{III,II} + RR_{III,II} + I_{III,IV} + C_{III}^{up}] \\ & + n(NIV)[RR_{IV,III} + DR_{IV,III} + T_{IV,III}] + n(NII)\cdot I_{II,III} \\ & + n(NII_{n=3})\cdot I_{II} + n(NIII_{n=3})\cdot[A_{III} + C_{III}^{down}] \end{aligned} \tag{A.8}$$

$$\begin{aligned}\frac{dn(NIV)}{dt} = 0 = & -n(NIV)[DR_{IV,III} + RR_{IV,III} + T_{IV,III} + I_{IV,V} + C_{IV}^{up}] \\ & + n(NV)[T_{V,IV} + DR_{V,IV} + RR_{V,IV}] + n(NIII)I_{III,IV} \\ & + n(III_{n=3})\cdot I_{III} + n(NIV_{n=3})\cdot[A_{IV} + C_{IV}^{down}] \end{aligned} \tag{A.9}$$

$$\begin{aligned}\frac{dn(NV)}{dt} = 0 = & \, n(IV)I_{IV,V} - n(NV)[DR_{V,IV} + RR_{V,IV} + T_{V,IV} + I_{V,VI} + C_V^{up}] \\ & + n(VI)[T_{VI,V} + DR_{VI,V} + RR_{VI,V}] \\ & + n(IV_{n=3})\cdot I_{IV} + n(V_{n=3})\cdot[A_V + C_V^{down}] \end{aligned} \tag{A.10}$$

$$\begin{aligned}\frac{dn(NVI)}{dt} = 0 = & \, n(V)I_{V,VI} - n(NVI)[DR_{VI,V} + RR_{VI,V} + T_{VI,V}] \\ & + n(VII)[T_{VII,VI} + DR_{VII,VI} + RR_{VII,VI}] \\ & + n(NV_{n=3})\cdot I_V \end{aligned} \tag{A.11}$$

$$\begin{aligned}\frac{dn(NVII)}{dt} = 0 = & -n(NVII)[DR_{VII,VI} + RR_{VII,VI} + T_{VII,VI} + I_{VII,VIII}] \\ & + n(VIII)[T_{VIII,VII} + DR_{VIII,VII} + RR_{VIII,VII}] + \\ & + n(VI)I_{VI,VII} \end{aligned} \tag{A.12}$$

Excited states

$$\frac{dn(NI_{n=3})}{dt} = 0 = n(NI)\cdot C_I^{up} + n(NII)\cdot T_{II} - n(NI_{n=3})\cdot[A_I + C_I^{down} + I_I] \tag{A.13}$$

$$\begin{aligned}\frac{dn(NII_{n=3})}{dt} = 0 = & \, n(NII)\cdot C_{II}^{up} + n(NIII)\cdot T_{III} \\ & - n(NII_{n=3})\cdot[A_{II} + C_{II}^{down} + I_{II}] \end{aligned} \tag{A.14}$$

$$\begin{aligned}\frac{dn(NIII_{n=3})}{dt} = 0 = & \, n(NIII)\cdot C_{III}^{up} + n(NIV)\cdot T_{IV} \\ & - n(NIII_{n=3})\cdot[A_{III} + C_{III}^{down} + I_{III}] \end{aligned} \tag{A.15}$$

$$\frac{dn(NIV_{n=3})}{dt} = 0 = n(NIV)\cdot C_{IV}^{up} + n(NV)\cdot T_V - n(NIV_{n=3})\cdot[A_{IV} + C_{IV}^{down} + I_{IV}] \quad (A.16)$$

$$\frac{dn(NV_{n=3})}{dt} = 0 = n(NV)\cdot C_{V}^{up} + n(NVI)\cdot T_{VI} - n(NV_{n=3})\cdot[A_{V} + C_{V}^{down} + I_{V}] \quad (A.17)$$

List of the matrix elements of $\mathcal{A}$

$$\begin{aligned}
a_{11} &= -(I_{I,II} + C_I^{up})\\
a_{12} &= T_{II,I} + RR_{II,I} + DR_{II,I}\\
a_{22} &= -(T_{II,I} + RR_{II,I} + DR_{II,I} + I_{II,III} + C_{II}^{up} + T_{II'})\\
a_{23} &= RR_{III,II} + DR_{III,II} + T_{III,II}\\
a_{33} &= -(T_{III,II} + DR_{III,II} + RR_{III,II} + I_{III,IV} + C_{III}^{up} + T_{III'})\\
a_{34} &= RR_{IV,III} + DR_{IV,III} + T_{IV,III}\\
a_{44} &= -(T_{IV,III} + DR_{IV,III} + RR_{IV,III} + I_{IV,III} + C_{IV}^{up} + T_{IV'})\\
a_{45} &= RR_{V,IV} + DR_{V,IV} + RR_{V,IV} + I_{V,VI}\\
a_{55} &= -(T_{V,IV} + DR_{V,IV} + T_{V,IV} + I_{V,VI} + C_V^{up} + T_{V'})\\
a_{56} &= RR_{VI,V} + DR_{VI,V} + T_{VI,V}\\
a_{66} &= -(T_{VI,V} + DR_{VI,V} + T_{VI,V} + I_{VI,VII} + T_{VI'})\\
a_{67} &= RR_{VII,VI} + DR_{VII,VI} + T_{VII,VI}\\
a_{77} &= -(T_{VII,VI} + DR_{VII,VI} + T_{VII,VI} + I_{VII,VIII})\\
a_{78} &= RR_{VIII,VII} + DR_{VIII,VII} + T_{VIII,VII}
\end{aligned}$$

$$\begin{aligned}
b_{11} &= A_I + C_I^{down} & d_{11} &= -(A_I + C_I^{down} + I_{I'})\\
b_{22} &= A_{II} + C_{II}^{down} & d_{22} &= -(A_{II} + C_{II}^{down} + I_{II'})\\
b_{33} &= A_{III} + C_{III}^{down} & d_{33} &= -(A_{III} + C_{III}^{down} + I_{III'})\\
b_{44} &= A_{IV} + C_{IV}^{down} & d_{44} &= -(A_{IV} + C_{IV}^{down} + I_{IV'})\\
b_{55} &= A_V + C_V^{down} & d_{55} &= -(A_V + C_V^{down} + I_{V'})
\end{aligned}$$

Bibliography

[Ahm81] G. Ahmadi, A. Hirose, 'Distortion of Velocity Gradient by Anomalous Viscosity', IEEE Trans. Plasma Sci. Vol. PS-9 (1), 21 (1981)

[Ald73] S.M.V. Aldrovandi, D. Pequignot, 'Radiative and Dielectronic Recombination Coefficients for Complex Ions', Astron. & Astrophys. **25**, 137 (1973)

[Ank99] C.M. Ankenbrandt et al., ' Status of muon collider research and development and future plans', Phys. Rev. ST Accel. Beams 2, 081001 (1999)

[Ban99] R.O. Bangerter, 'Ion beam fusion', Phil. Trans. R. Soc. Lond. A **357**, 575 (1999)

[Bet83] H.D. Betz, Applied Atomic Collision Physics, Vol. 4, p.1, Editors: H.S.W. Massey et al., Pure and Applied Physics **43-4**, Academic Press, Orlando (1983)

[Bis85] W.K. Bischel, L.J. Jusinski, M.N. Spencer, D.J. Eckstrom, 'Absolute two-photon ionization yields for selected organic molecules at 248 nm', J. Opt. Soc. Am. B **2**(6), 877 (1985)

[Blu92] H.J. Bluhm, P.J.W. Hoppe, H.P. Laqua, D. Rusch, 'Production and Investigation of TW Proton Beams from an Annular Diode Using Strong Radial Magnetic Insulation Fields and a Preformed Anode Plasma Source', Proceedings of the IEEE **80**, 995 (1992)

[Bog91] E. Boggasch, J. Christiansen, K. Frank, R. Tkotz, H. Riege, 'Z-Pinch Current Enhancement by the Inverse Skin Effect', IEEE Trans. Plasma Sci. **19**, 866 (1991)

[Bog92] E. Boggasch, D.H.H. Hoffmann, H. Riege, 'Fokussierung von Teilchenstrahlen mit Plasmalinsen', Physik in unserer Zeit, **23**(6), 272 (1992)

[Bur98] 'Ultra-Low Noise Precision OPERATIONAL AMPLIFIERS', PDS-466M, Burr Brown Corporation, PO BOX 11400, Tucson, AZ 85734, 1998

[Car93] F. Carminati et al. 'An Energy Amplifier for cleaner and inexhaustible Nuclear Energy Production driven by a Particle Beam Accelerator', CERN/AT/93-47 (1993)

[Dav97] G. Davara, L. Gregorian, E. Kroupp, Y. Maron, 'Spectroscopic determination of the magnetic-field distribution in an imploding plasma', Phys. of Plasm. **5**(4), 1068 (1997)

[Fal68] I.S. Falconer, S.A. Ramsden, J. Appl. Phys. 39, 3449 (1968)

[Fes97] T.J. Fessenden, M.C. Vella, 'Plasma pinch for transport of HIF beams', LBNL HIFAR-474, June 6 (1997)

[Fre82] J.R. Freeman, L. Baker, D.L. Cook, 'Plasma Channels for intense Light-Ion-Beam Transport', Nucl. Fus. **22**, 383 (1982)

[Fro82] C.A. Frost, J.R. Woodworth, J.N. Olsen, T.A. Green, 'Plasma channel formation with ultraviolet lasers', Appl. Phys. Lett. **41**(9) 813 (1982)

[Gab72] M. Gabriel, Mon. Not. Astro. Phys. **160**, 99 (1972)

[Gal84] W. Galus, F.S. Perry, Laser Focus / Electro-Optics, Vol.20, No 11, 76-82, (1984)

[Gar95] I. S. K. Gardner, H. Lengeler, G. H. Rees, 'Outline Design of the European Spallation Neutron Source', ESS 95-30-M, September (1995)

[Gee98] S. Geer, 'Neutrino beams from muon storage rings: characteristics and physics potential', Phys. Rev. D **57**,6989 (1998)

[Gri64] H.R. Griem, 'Plasma Spectroscopy', McGraw-Hill, New York (1964)

[Gri68] R.F. Gribble, E.M. Little, R.L. Morse, W.E. Quinn, Phys. Fluids **11**, 1221 (1968)

[Gri74] H.R. Griem, 'Spectral line broadening by plasmas', Pure and Applied Physics **39**, Academic Press, New York (1974)

[Hai59] M.G. Haines, 'The inverse skin effect', Proc. Phys. Soc. **74**(5), 576 (1959)

[Hen98] E. Henestroza, S.S Yu, M.C. Vella, W.M. Sharp, 'Simulations of channel-based final beam transport', Nucl. Instr. and Meth. A **415**, 186 (1998)

[Hil67] R.A. Hill, J.B. Gerardo, 'Stark Broadening of H_β, H_γ, and H_δ: An Experimental Study', Phys. Rev. **162**, 45 (1967)

[Hin92] D. Hinshelwood, 'Development of wall-stabilized z discharges for intense ion-beam transport in inertial confinement fusion facilities', J. Appl. Phys. **72**(10), 4581 (1992)

[Hog92] W.J. Hogan, R. Bangerter, G.L. Kulcinski, 'Energy from inertial fusion', Physics Today, 42, September (1992)

[Hut81] D.P. Hutchinson, C.H. Ma, P.A. Staats, K.L. Vander Sluis, 'Simultaneous measurement of line electron density and Faraday rotation in the ISX-B tokamak', Nucl. Fus. **21**(12), 1535 (1981)

[Hut87] I.H. Hutchinson, 'Principles of plasma diagnostics', Cambridge University Press, Cambridge (1987)

[Jac83] J.D. Jackson, 'Klassische Elektrodynamik', Walter de Gruyter, Berlin (1983)

[Jah71] F.C. Jahoda, G.A. Sawyer, in 'Methods of Experimental Physics', Vol. 9B, (R.H. Lovberg and H.R. Griem, eds.), Academic Press, New York (1971)

[Jar77] T.R. Jarboe, J. Appl. Phys. 48, 557 (1977)

[Job92] F.C. Jobes, D.K. Mansfield, 'Midplane Faraday rotation: A densitometer for large tokamaks', Rev. Sci. Instr. **63** (10), 5154 (1992)

[Kop79] D.W. Koopman et al., J. DePhysique Coll. 7. Suppl. 7., Tome 40, 419 (1979)

[Kun78] W. Kunz, 'First measurements of poloidal-field-induced Faraday rotation in a tokamak plasma', Nucl. Fus. **18** (12), 1729 (1978)

[Kur95] R.L. Kurucz, B. Kelly, '1995 Atomic Line Data, Kurucz CD-ROM No. 23', Cambridge, Mass.: Smithonian Astrophysical Observatoy *(http://cfa-www.harvard.edu/amdata/ampdata/kurucz23/sekur.html)* (1995)

[Lan74] L.D. Landau, E.M. Lifschitz, 'Lehrbuch der Theoretischen Physik, Band VIII: Elektrodynamik der Kontinua', Akademie-Verlag, Berlin (1974)

[Lee82] L.C. Lee, W.K. Bischel, 'Two-photon-ionization coefficients of propane, 1-butene and methylamines', J. Appl. Phys. **53** (1), 203 (1982)

[Lee01] R.W. Lee, F.B. Rosmej, private communication (2001)

[Loc68] W. Lochte-Holtgreven, 'Plasma Diagnostics', North-Holland, Amsterdam, 597 (1968)

[Ma79] C.H. Ma, D.P. Hutchinson, K.L. Vander Sluis, 'A modulated submillimeter-laser polarimeter for the measurement of the Faraday rotation by a plasma', Appl. Phys. Lett. **34**(3), 218 (1979)

[Man73] W.M. Manheimer, M. Lampe, J. Boris, 'Effect of a surrounding gas on magnetohydrodynamic instabilities in Z pinch', Phys. Fluids **16** (7), 1126 (1973)

[Man84] A. Mankofsky, R.N. Sudan, 'Numerical simulation of ion beam propagation in z-pinch plasma channels', Nucl. Fus. **24** (7), 827 (1984)

[Mar94] R.A. Marsland, 'Balanced photoreceivers challenge shot-noise limit', Laser Focus World, 41, March (1994)

[Mar85] W.E. Martin, G. J. Caporaso, W. M. Fawley, D. Prosnitz, A.G. Cole, 'Electron-Beam Guiding and Phase-Mix Damping by a Laser-Ionized Channel', Phys. Rev. Lett. **54** (7), 685 (1985)

[Mci77] T.J. MacIlrath, T.B. Lucatorto, 'Laser Excitation and Ionization in a Dense Li Vapor: Observation of the Even-Parity, Core-Excited Autoionizing States', Phys. Rev. Lett, **38** (24), 2662 (1979)

[Mea79] R.M. Measures, N. Drewell, P. Cardinal, 'Electron- and ion-beam transportation channel formation by laser ionization based on resonance saturation - LIBORS', J. Appl. Phys. **50** (40), 2662 (1979)

[Mer81] W. Merzkirch, in Methods of Experimental physics **18**, 'Fluid Dynamics', R.J. Emrich, Ed., 345 (1981)

[Mew67] R. Mewe, Brit. J. Appl. Phys. **18**, 107 (1967)

[Miy84] T. Miyamoto, 'Analysis of High-Density Z-Pinches by a Snowplow Energy Equation', Nucl. Fusion **24**, 337 (1984)

[Moi92] R.W. Moir, 'HYLIFE-II Inertial Confinement Fusion Power Plant Design', Part. Accel. **37-38**, 467 (1992)

[Nef02] S. Neff, 'Diagnostik und Simulation eines laserinduzierten Plasmakanals für Ionenstrahltransportexperimente', Diploma Thesis, TU-Darmstadt (2002)

[Ner93] J. Neri, P.F. Ottinger, D.V. Rose, P.J. Goodrich, D.D. Hinshelwood, D. Mosher, S.J. Stephanakis, F.C. Young, 'Intense ion-beam-transport experiments using a z-discharge plasma channel', Phys. Fluids B5, 176 (1993)

[Noo97] W.A. Noonan, T.G. Jones, P.F. Ottinger, 'Laser induced fluorescence diagnostic for measuring small magnetic fields', Rev. Sci. Instrum. **68**(1), 1032 (1997)

[Ols80] J.N. Olsen, D.J. Johnson, R.J. Leeper, 'Propagation of light ions in a plasma channel', Appl. Phys. Lett. **36**, 808 (1980)

[Ols81a] J.N. Olsen, 'Laser-initiated channels for ion transport: CO_2-laser absorption and heating of NH_3 and C_2H_4 gases', J. Appl. Phys. **52** (5), 3279 (1981)

[Ols81b] J.N. Olsen, L. Baker, 'Laser-initiated channels for ion transport: Breakdown and channel evolution', J. Appl. Phys. **52** (5), 3286 (1981)

[Ols82] J.N. Olsen, R.J. Leeper, 'Ion beam transport in laser-initiated discharge channels', J. Appl. Phys. **53** (5), 3397 (1982)

[Ott91] P.F. Ottinger, D.V. Rose, D. Mosher, J.M. Neri, 'Z-discharge transport of intense ion beams for inertial confinement fusion', J. Appl. Phys. **70** (10), 5292 (1991)

[Ott00] P.F. Ottinger, F.C. Young, S.J. Stephanakis, D.V. Rose, J.M. Neri, B.V. Weber, M.C. Myers, D.D. Hinshelwood, D. Mosher, C.L. Olsen, D.R. Welch, 'Self-pinched transport of an intense proton beam', Phys. Plasmas **7**, 346 (2000)

[Oza83] T. Ozaki, A. Yoshinouchi, S. Miyamoto, K. Imasaki, S. Nakai, C. Yamanaka, 'Light ion beam transport in a multi-plasma channel system', Proc. 5^{th} Int. Conf. on High Power Part. Beams, San Francisco, 78 (1983)

[Oza85] T. Ozaki, S. Miyamoto, K. Imasaki, S. Nakai, C. Yamanaka, 'Light ion beam transport in plasma channels', J. Appl. Phys. **58** (6), 2145 (1985)

[Pen02] D. Penache, PhD thesis, TU-Darmstadt, to be completed in 2002

[Per96] F. Perry, 'Predicting the performance of a photodetector', Boston Electronics Corporation, 72 Kent Street, Brookline, MA 02146 USA (1996)

[Pon01] D.M. Ponce, C. Niemann, S.S. Yu, W.P. Leemans, T.J. Fessenden, G. Dahlbacka, W.M. Sharp, A. Tauschwitz, 'Diagnostics of plasma channels for HIF transport', Nucl. Instr. and Meth. A **464**, 331 (2001)

[Pon02] D.M. Ponce, PhD Thesis, UC Berkeley, to be completed in 2002

[Pot78] D. Potter, 'The formation of high-density z-pinches', Nucl. Fusion **18**, 813 (1978)

[Pre92] W.H. Press, S.A. Teukolsky, W.T. Vetterling, B.P. Flannery, 'Numerical Recipes in C, The Art of Scientific Computing', 2^{nd} Edition, Cambridge University Press (1992)

[Rad68] H.E. Radford, 'Electrical breakdown in ammonia at low pressure', NBS report 9882 (1968)

[Reg62] H. Van Regemorter, 'Rate of Collisional Excitation in Stellar Atmospheres', Astro. Phys. J. **136**, 906 (1962)

[Ric92] B.W. Rice, 'Fifteen chord FIR polarimetry system on MTX', Rev. Sci. Instr. **63** (10), 5002 (1992)

[Ril92] R.A. Riley, R.H. Lovberg, J.S. Shlachter, D.W. Scudder, 'Optical diagnostics on dense Z-pinch plasmas', Rev. Sci. Instrum. **63** (10), 5202 (1992)

[Ros54] M. Rosenbluth, Los Alamos Sci. Lab Rep., LA-1850 (1954)

[Ros98] F.B. Rosmej, 'Spektroskopische Methoden zur Analyse von Plasmen im Nicht-Gleichgewicht', Habilitationsschrift, Bochum (1998)

[Ros00] F.B. Rosmej, et al., 'X-ray radiation from ions with K-shell vacancies', JQSRT **65**, 477 (2000)

[Ros01] F.B. Rosmej, 'A new type of analytical model for complex radiation emission of hollow ions in fusion, laser and heavy-ion-beam-produced plasmas', Europhys. Lett. **55**, 472 (2001)

[Ros01b] F.B. Rosmej, private communication (2001)

[Ros01c] F.B. Rosmej, V.S. Lisitsa, R. Stamm, to be published

[San81] F.A. Sandel, S.J. Stephanakis, F.C. Young, W.F. Oliphant, 'Experimental Studies of Intense Light-Ion Beam Transport', Proc. 4^{th} Int. Conf. on High-Power Electron- and Ion Beams, Palaiseau, France, 129 (1981)

[Sar95] G.S. Sarkisov, A.S. Shikanov, 'Structure of the magnetic fields in Z-pinches', JETP **81** (4), 743 (1995)

[Sna00] R.A. Snaveley, M.H. Key, S.P. Hatchett, T.E. Cowan, M. Roth, T.W. Philips, M.A. Stoyer, E.A. Henry, T.C. Sangster, M.S. Singh, S.C. Wilks, A. McKinnon, A. Offenberger, D.M. Pennington, K. Yasuike, A.B. Langdon, B.F. Lasinski, J. Johnson, M.D. Perry, E.M. Campbell, 'Intense High-Energy Proton Beams from Petawatt-Laser Irradiation of Solids',Phys. Rev. Lett. **85**, 2945 (2000)

[Sob95] I.I. Sobelman, 'Excitation of atoms and broadening of spectral lines', Springer Series on Atoms and Plasmas 15, Springer, New York (1995)

[Sol86] H. Soltwisch, 'Current distribution measurements in a tokamak by FIR polarimetry', Rev. Sci. Instr. **57** (8), 1939 (1886)

[Spi56] L. Spitzer, 'Physics of fully ionized gases', Interscience Publishers, New York (1956)

[Ste96] M. Stetter, U. Neuner, S. Stoewe, M. Dornik, D.H.H. Hoffmann, R. Kowalewicz, P. Spiller, A. Tauschwitz, 'The high current plasma lens: investigations of fine focusing of high energy heavy ion beams', Fus. Eng. Des. **32-33**, 503 (1996)

[Tab98] M. Tabak, D. Callahan-Miller, 'Design of a distributed radiator target for inertial fusion driven from two sides with heavy ion beams', Nucl. Instr. Meth. A **415**, 75 (1998)

[Tau96] A. Tauschwitz, S.S. Yu, S. Eylon, R.O. Bangerter, J.J. Barnard, W. Leemans, C. Peters, J.O. Rasmussen, L. Reginato, W.M. Sharp, 'Plasma lens focusing and plasma channel transport for heavy ion fusion', Fus. Eng. Des. **32-33**, 493 (1996)

[Tau98] A. Tauschwitz, S. Yu, S. Eylon, T. Fessenden, E. Henestroza, R. Lafever, W. Leemans, R. Petzoldt, D. Pnce, M. Vella, R.W. Moir, W.M. Sharp, M. de Magistris, R. Peterson, M. Sawan, 'Plasma-Channel-Based Final Transport and Reactor', in 'The HIDIF-Study', eds. I. Hofmann, G. Plass, GSI Report 98-06, 213 (1998)

[Tau99] A. Tauschwitz, C. Niemann, D. Penache, C. Penache, R. Presura, E. Wille, U.N. Funk, M. Geissel, D.H.H. Hoffmann, U. Neuner, A. Golubev, V. Turtikov, R. Knobloch, O. Winkelmann, F. Karstens, H. Wahl, 'Ion Beam Transport in a Laser Initiated Discharge channel', Proceedings: Inertial Fusion Sciences and Applications 1999, Editors: C. Labaune, W. Hogan, K. Tanaka, Elsevier, 521 (1999)

[Tau01] A. Tauschwitz, C. Niemann, D. Penache, S. Neff, R. Knobloch, H. Wahl, D.H.H. Hoffmann, 'Ion Beam Transport in Discharge Channels', GSI-AR 2000(2001)

[Tau01b] A. Tauschwitz, 'Space charge and current neutralized transport and focusing of heavy ion beams with discharge plasmas', Habilitationsschrift, Darmstadt (2001)

[Tay80] R.S. Taylor, A.J. Alcock, K.E. Leopold, 'Laser-induced preionization of rare-gas halide discharge', Opt. Lett. **5** (6), 216 (1980)

[Tho88] A.P. Thorne, 'Spectrophysics', 2^{nd} Edition, Chapman and Hall (1988)

[Tho95] M. Thomson, 'Side-on Messungen der Balmerlinie H_α an einem Plasma hoher Dichte', Diploma Thesis, Kiel (1995)

[Tuy93] G.J. Van Tuyle et al., 'Accelerator-Driven Subcritical Target Concept for Transmutation of Nuclear Wastes', Nuclear Technology, Vol. 10l, 1, January (1993).

[Uni95] United States Environemantal Protection Agency, 'Innovative high risk/high priority anhydrous ammonia study', (http://www.tbrpc.org/lepc/ammonia.htm) (1995)

[Van00] K. Vandersloot, 'Mathematical equations used in CYCLOPS', HIFAR 500, LBNL report 46692 (2000)

[Vel96] M.C. Vella, T.J. Fessenden, W. Leemans, S. Yu, 'Plasma pinch for final focus and transport', LBNL-40435, UC-415, HIFAN 885, 1996

[Vel98] M.C. Vella, T.J. Fessenden, W. Leemans, S. Yu, A. Tauschwitz, 'Plasma pinch for final focus and transport', Nucl. Instr. Meth. A **415**, 193 (1998)

[Wea90] R.C. Weast, D.R. Lide, M.J. Astle, W.H. Beyer, 'CRC Handbook of Chemistry and Physics', 70^{th} Edition, CRC Press, Inc., Boca Raton, Florida (1990)

[Wei00] J. Wei, D.T. Abell, J. Beebe-Wang, M. Blaskiewicz, P.R. Cameron, N. Catalan-Lasheras, G. Danby, A.V. Fedotov, C. Gardner, J. Jackson, Y.Y. Lee, H. Ludewig, N. Malitsky, W. Meng, Y. Papaphilippou, D. Raparia, N. Tsoupas, W.T. Weng, R.L. Witkover, S.Y. Zhang, Physical Review Special Topic AB, Vol. 3, 080101 (2000)

[Wen97] W. Weng, in *Proceedings of the 1997 Particle Accelerator Conf.,* Vancouver, 42 (1997)

[Wie72] W.L. Wiese, D.E. Kelleher, D.R. Paquette, 'Detailed Study of the Stark Broadening of Balmer Lines in a High-Density Plasma', Phys. Rev. A **6** (3), 1132 (1972)

[Wie96] W.L. Wiese, J.R. Fuhr, T.M. Deters, 'Atomic Transition Probabilities of Carbon, Nitrogen and Oxigen', Journal of Physical and Chemical Reference Data, Monograph No. 7 (1996)

[Woo85] J.R. Woodworth, T.A. Green, C.A. Frost, 'Ionization of organic molecules with ultraviolet lasers: A technique for generating large, well-defined ionized volumes', J. Appl. Phys. **57** (5), 1648 (1985)

[Yu98] S.S. Yu, S. Eylon, T. Fessenden, E. Henestroza, R. Lafever, W. Leemans, R. Petzoldt, D. Ponce, M. Vella, R.W. Moir, W.M. Sharp, R. Peterson, M. Sawan, A. Tauschwitz, 'Plasma-channel-based reactor and final transport', Nucl. Instr. and Meth. A **415**, 174 (1998)

[Zie96] J.F. Ziegler, J.P. Biersack, U. Littmark, 'The stopping and Ranges of Ions in Solids', Pergamon, New York (1996)

Acknowledgements

At this point I would like to express my gratitude to all those who made this work possible, and whose contributions played an important role for the completion of this thesis. In particular I would like to thank to:

Professor Dr. Dr.h.c. Dieter H.H. Hoffmann for the opportunity to take part in the interesting research project and for the strong support to perform some of the experiments in Berkeley. He has always been an excellent supervisor, providing the right atmosphere, which is crucial for a successful and enjoyable doctoral work. Herzlichen Dank für Alles !

Dr. Simon S. Yu for the possibility to participate in the channel experiment in Berkeley. His skillful guidance and the enthusiasm about physics that he passed on to me strongly influenced my work, also at GSI.

Dr. Andreas Tauschwitz for the support and guidance during the experiments at GSI. He has always been open for new ideas and kept the work on the right track. He was also very helpful with the proofreading of the manuscript.

Priv. Doz. Dr. Frank B. Rosmej for the intense and outstanding supervising in the spectroscopic part of the work, which he continued even after he left the group. Without his help and expertise the chapter on spectroscopy would not have been possible.

Dr. Radu Presura for the guidence and the very nice working atmosphere during the first months when he was still at GSI. Many of the ideas behind this work were born in the interesting discussions we had.

My colleagues Dan Penache, Stephan Neff, Richard Birkner and Renate Knobloch at GSI for the many hours they spent to help with all aspects of the experiments. Dipl. Ing. Heinrich Wahl gave the technical support and was always very helpfull with any problem encountered in the experiments.

David Ponce has deeply contributed to my understanding of plasma diagnostics and made my stay at LBL as pleasant and interesting as possible.

Carmen Constantin for the help with the experiment on quite a lot of weekends, for precious encouragements and for proofreading the manuscript.

Dr. Joachim Jacoby for the valuable discussions about the ion beam initiated channels

All members of the Plasma Physics Group at GSI and the AFRD division in Berkeley for the nice and friendly working atmosphere as well as the people from the workshops at GSI and TU-Darmstadt, which contributed in many ways to the work.

And last but not least my parents for making this dissertation possible.

Lebenslauf

Persönliche Angaben

Name:	**Christoph Niemann**
Anschrift:	Hildegardstr. 11 96049 Bamberg
Geburtsdatum / -ort:	10.05.1973 / Düsseldorf
Staatsangehörigkeit:	deutsch
Familienstand:	ledig

Ausbildung

Sept. 79 - Juli 83:	Grundschule Bamberg - Bug
Sept. 83 - Juni 93:	Besuch des E.T.A. Hoffmann Gymnasiums Bamberg, Abitur im Juni 93
Nov. 93 - Juli 98:	Studium der Physik an der Friedrich Alexander Universität Erlangen - Nürnberg, Vordiplom im Juni 95, Diplom im Juli 98
Sept. 95 - April 96:	Gaststudent an der University of East Anglia, Norwich, England
März 97 - März 98:	Diplomarbeit am Max Planck Institut für Plasmaphysik in Garching und der FAU-Erlangen zum Thema 'Das Isotopenverhältnis H/D im ASDEX Upgrade Tokamak'
seit August 98:	Doktorand an der TU-Darmstadt und GSI-Darmstadt
März 99 - Nov. 99:	Forschungsaufenthalt am Lawrence Berkeley National Laboratory, Berkeley, USA

Hiermit erkläre ich, daß ich die Arbeit selbständig und nur mit den angegebenen Hilfsmitteln angefertigt und nicht schon früher eine Promotion versucht habe.

7. Februar 2002 Christoph Niemann